Dissertation

submitted to the
Combined Faculty of Natural Sciences and Mathematics
of the Ruperto Carola University Heidelberg, Germany
for the degree of

Doctor of Natural Sciences

Presented by

Benedikt Best, B.Sc. (Hons)

born in: Heilbronn-Neckargartach

Oral examination: 13th March 2019

Rab-mediated membrane trafficking systems in terminal tracheal cells of *Drosophila melanogaster*

Referees: Dr. Stefano De Renzis

Prof. Dr. Michael Boutros

Acknowledgements

First and foremost my gratitude goes to my mentor, Maria Leptin, one of the few supervisors who are really worth learning from.

Next of course is the obligatory cheers to my lab. Baubi, Catarina, Daniel, Denisa, Eva, Juan, Julio, Matteo, Paola, Sara, Sinja, Sourabh, Srishti, all of you have made and still do make life in the lab worth working.

I am grateful also to my advisory committee, Stefano De Renzis, Michael Boutros and Darren Gilmour. Your feedback helped steer me on a realistic track and kept me going me when things under the microscope didn't.

My work progressed immensely faster thanks to the reliable advice and assistance by the Advanced Life Microscopy Facility at EMBL, and the entire infrastructure and support system. You're brilliant, IT, fly kitchen, cleaning crew, maintenance team. Special thanks go to Bernd Klaus for making sure I'm doing Maths and not Connect-the-Dots.

Credit also goes to my undergrad tutor and supervisor, Jim Crawley, for the privilege to do my PhD at EMBL. Thank you for encouraging me to "just give it a try".

There probably wouldn't be a thesis for me to write right now without all the support and encouragement from my family and friends. Thank you Doro, Reiner, Jonathan, Christofer and Thaddea, and Josias. And thank you in particular, Alina. Du bisch a rechts Schätzle.

Also, hi Andreas, Malte, Charli, Steve, Tom, Eni, Alex. Look, I'm an author!

Table of Contents

Summary

The terminal cells of the tracheal system in *Drosophila melanogaster* are one of the few known cell types that form stable, long branches. Like all epithelial cells, terminal cells have an apical and a basal membrane domain. Throughout larval life, each terminal cell's basal membrane repeatedly bifurcates and elongates to establish an extensive branched network, and the apical membrane is invaginated to form a subcellular tube that expands a lumen in each branch. The lumen is contiguous with the tracheal system's lumen and carries air to deliver oxygen to internal organs. To achieve this elaborate structure, terminal cells expand their volume and surface area at least hundredfold over the course of a few days. The synthesis and distribution of membrane and proteins must thus pose a particular challenge. In addition to the necessary bulk of production, all material needs to be delivered to the appropriate membrane domain. In particular, the specialised apical extracellular matrix within the tracheal lumen must be supplied with the structural molecules that confer the tracheal system its physical stability and the ability to contain and exchange gas.

My hypothesis was thus that terminal cells possess a customised membrane trafficking system that allows them to transport large amounts of newly synthesised proteins and lipids through secretory pathways to the apical and basal domains as appropriate. This directed the focus of my research to the Rab family of small GTPases, a group of proteins known as master regulators of membrane trafficking. Rabs bind to the plasma membrane or to intracellular membrane compartments and subsequently function as platforms to recruit effector proteins. These effectors execute virtually all mechanisms that direct membrane-bound and secreted molecules from one membrane compartment to the next, as well as to and from the cell's exterior environment.

To explore membrane trafficking systems in terminal cells, I first conducted a systematic quantitative analysis of normal and abnormal terminal cell phenotypes to better understand how morphological defects should be interpreted. This was necessary because of the variability with which mutant phenotypes manifest in terminal cells. My results provide a reference for the range of natural variability in TC phenotypes, and identify phenomic analysis, currently only applied to plants, as a powerful method for extracting meaning from partially penetrant loss-of-function phenotypes. The main part of my work was a tracheal knockdown screen targeting all *Drosophila* Rabs. Rather than using specific RNAi constructs against each gene, I utilised a collection of endogenously YFP-tagged Rabs and knocked down the YFP tag in animals where all copies of a Rab are tagged. This indirect approach confers more confidence in its results because unlike conventional RNAi, its risk of false positives is minimal. Through this and supplementary experiments, I pinpointed a secretion route from endoplasmatic reticulum through Golgi and endosomes to the plasma membrane that ensures proper organisation of the extracellular matrix and allows the cell to grow. I identified only one Rab whose phenotype suggested a role in establishing the shape and size of the subcellular tube: Rab8. In my final experiments, I therefore investigated how Rab8 is involved in apical morphogenesis in terminal cells. While not definitive, my results suggest that Rab8 acts on apically-directed secretory endosomal traffic to retain basally-destined cargoes, thereby preventing their erroneous apical secretion.

Zusammenfassung

Die Endzellen des trachealen Systems in *Drosophila melanogaster* sind eine der wenigen bekannten Zellarten, die stabile, lange Äste bilden. Wie alle Epithelzellen haben Endzellen eine apikale und eine basale Membrandomäne. Im Verlauf der Larvenstadien verlängert und verästelt sich die basale Domäne wiederholt, um ein weitläufiges Astnetzwerk zu schaffen. Die apikale Domäne wird ins Zellinere eingestülpt und bildet eine subzelluläre Röhre, die in jedem Ast ein Lumen ausdehnt. Dieses ist mit dem Lumen des Tracheensystems verbunden und enthält Luft, welche die internen Organe mit Sauerstoff versorgt. Um diese komplexe Struktur zu erreichen, vergrößern Endzellen ihr Volumen und ihre Oberfläche im Verlauf einiger Tage mindestens hundertfach. Die Synthese und Verteilung von Membran und Proteinen muss daher eine besondere Herausforderung darstellen. Zusätzlich zur notwendigen Masse an Produktion muss alles Material an die adäquate Membrandomäne geliefert werden. Insbesondere die spezialisierte apikale extrazelluläre Matrix im trachealen Lumen muss mit den Strukturmolekülen versorgt werden, die dem Tracheensystem seine physikalische Stabilität und die Fähigkeit, Gas zu enthalten und auszutauschen, verleihen.

Meine Hyothese war daher, dass Endzellen über ein besonderes Membrantransportsystem verfügen, das ihnen den fehlerfreien Transport von großen Mengen neu synthetisierter Proteine und Lipiden über Sekretionswege zur apikalen und basalen Domäne ermöglicht. Dies konzentrierte meine Arbeit auf die Familie der Rab GTPasen, eine Gruppe von Proteinen, die als wichtige Regulatoren des Membrantransports bekannt sind. Rabs binden die Plasmamembran oder intrazelluläre Membrankompartimente und fungieren dann als Plattform zur Rekrutierung von Effektorproteinen. Diese Effektoren setzen alle Mechanismen um, die membrangebundene und sekretierte Moleküle von einem Membrankompartiment zum anderen, und zum bzw. vom extrazellulären Raum leiten.

Zur Untersuchung des Membrantransportsystems in Endzellen habe ich zunächst eine systematische, quantitative Analyse von normalen und abnormalen Endzellphänotypen unternommen, um besser zu verstehen, wie morphologische Defekte interpretiert werden müssen. Dies war aufgrund der Variabilität, mit der Phänotypen von Mutanten in Endzellen auftreten, notwendig. Meine Ergebnisse stellen eine Referenzspanne der natürlichen Variabilitat in Endzellphänotypen dar und identifizieren die phänomische Analyse, welche bislang nur bei Pflanzen angewendet wurde, als eine leistungsstarke Methode, um trotz phänotypischer Variation sinnvolle Schlüsse aus Endzellphänotypen zu ziehen. Der Hauptteil meiner Arbeit war ein tracheales "Knockdown" Screening aller *Drosophila* Rabs. Statt spezifische RNAi-Konstrukte gegen jedes Gen zu testen, habe ich eine Sammlung von endogen YFP-verbundenen Rabs verwendet und RNAi gegen die YFP-Sequenz angewendet. Diese indirekte Methode verleiht den Resultaten des Screenings mehr Sicherheit, denn im Gegensatz zur traditionellen RNAi ist das Risiko von falsch positiven Resultaten minimal. Durch dieses und vervollständigende Experimente habe ich eine Sekretionsroute vom endoplasmatischen Reticulum über den Golgiapparat und Endosomen zur Plasmamembran aufgezeigt, welche die korrekte Organisierung der

extrazellulären Matrix sicherstellt und das Wachstum der Zelle ermöglicht. Ich habe lediglich ein einzelnes Rab identifiziert, dessen Phänotyp eine Rolle in der Festlegung der Form und Größe der subzellulären Röhre nahelegt: Rab8. In meinen abschließenden Experimenten habe ich daher untersucht, wie Rab8 die apikale Morphogenese der Endzellen beeinflusst. Obwohl meine Resultate nicht endgültig sind, deuten sie darauf hin, dass Rab8 an apikal-orientiertem sekretorischem Endosomtransport operiert, um basal-orientierte Beladungen zurück zu halten und damit eine fehlerhafte apikale Sekretion derselben zu verhindern.

Abbreviations

aECM	apical extracellular matrix
btl	*breathless*, a *Drosophila* FGFR
CI	confidence interval
DAPI	4',6-diamidino-2-phenylindole
DB	dorsal branch
dsrf	*blistered*, the *Drosophila* serum response factor
DT	dorsal trunk
ER	endoplasmatic reticulum
FGFR	fibroblast growth factor receptor
GAP	GTPase activating protein
GDP/GTP	guanosine di-/tri-phosphate
GEF	GTP exchange factor
MAPK	mitogen-activated protein kinase
PIP	phosphoinositide phosphate
Rab5-IR/Rab8-IR/...	Rab5/Rab8/... interfering RNA (transgenic construct)
RNAi	RNA interference
TC	terminal cell
UAS	upstream activating sequence
YRab-gfpIR	indirect RNAi against an endogenously YFP-tagged Rab by expressing GFP-IR

List of Figures and Tables

1. Introduction

1.1 Development of the tracheal system in Drosophila melanogaster

The life cycle of the fruit fly, *Drosophila melanogaster*, consists of four main stages, of which two are mobile: embryo, larva, pupa and adult (Bates and Martinez-Arias, 1993; Hartenstein, 1993). After copulation, female adults retain the male's sperm to continuously fertilise eggs, which they deposit in a suitable substrate. The embryo undergoes seventeen stages of development, of which the first four are characterised primarily by multiple rounds of division of the egg's nucleus. At stage five, membranes form around the nuclei in a process termed cellularisation. This is shortly followed by the onset of gastrulation, marked by the first concerted tissue movement, the formation and internalisation of the ventral furrow. This results in the division of the three germ layers. The internalised cells become the mesoderm, cells at the anterior and posterior ends of the embryo become the endoderm, and the midlateral cells that remain after the mesoderm is internalised become the ectoderm. Ventral furrow internalisation is followed by the extension of the germ band, whereby the ventrally located mesoderm and ectoderm stretch around the posterior end, fold over, and extend on the dorsal side until they reach the head. During and after germ band extension, subsets of cells within each germ layer adopt tissue fates and begin executing the various genetic and morphogenetic programs to ultimately form their specific organ. Many of these processes are organised by the division of the germ band into eleven segments that persists also into the adult stage. The germ band then again retracts around the posterior end, and as soon as the last segment has aligned, the dorsal boundaries of the segments begin stretching towards the midline in the process known as dorsal closure. By the point the contralateral migrating boundaries have met and closed the gap at the dorsal midline, most aspects of the larval body plan have been laid down and most organs are formed. Embryogenesis concludes when the larva hatches from the egg.

The larval stage lasts for several days and is subdivided into three instars, separated by two moults during which the larva sheds its mouth parts and cuticle (Bates and Martinez-Arias, 1993; Hartenstein, 1993). The main developmental process of the larval stages is simple growth, which is primarily achieved by increases of cell sizes since most larval cells are postmitotic (Guha et al., 2008). This does not apply to the imaginal discs, specialised organs whose cells will form much of the adult body during metamorphosis. Throughout larval life, cells of the imaginal discs replicate, effect shape changes of their tissue, and adopt fates for specific subsections of the adult body part. Two to three days after the second moult, when the larva has grown enough, it leaves its food medium and crawls upwards on the wall of the vial in case of cultured animals. Eventually the larva settles down and begins pupation, accompanied by increasing levels of the steroid hormone ecdysone (Hyun, 2018). Once its pupal case is formed, the pupa undergoes metamorphosis, during which most of the larval cells die and are replaced by the fully differentiated cells that form the adult's body.

These can originate both from dedicated pockets of precursors already present in the larva, and also from postmitotic larval cells that dedifferentiate and reenter the cell cycle (Guha et al., 2008). Simultaneously, the imaginal discs undergo substantial tissue shape changes and movements to form the respective body part, including head appendages (antennae, mouth parts), eyes, prothorax, legs, wings and genitalia (Aldaz and Escudero, 2010). The pupal stage is subdivided descriptively by the pupa's colour, which darkens gradually from the initial white colour of the larva to a brownish shade. Near the end of metamorphosis, the eyes become visible due to their pigmentation, and the wings become black, giving this final "black" pupal stage its name. The fully developed adult finally ecloses from the pupal case.

1.1.1 Tracheal cell fate specification and primary branching

Tracheal development begins mid-embryogenesis during germ band elongation with the specification of the tracheal fate in ten groups of ectodermal cells on each side of the embryo (Hayashi and Kondo, 2018). This is hallmarked by the expression of the transcription factor *trachealess* (*trh*), which is stimulated in ~20 cells in each segment by JAK/STAT signalling (Brown et al., 2001; Sotillos et al., 2010) and constrained in the dorsoventral and anteroposterior axes by *wingless* (*wg*) and *decapentaplegic* (*dpp*) signalling (Isaac and Andrew, 1996; Wilk et al., 1996). These cells constitute the tracheal placode, which invaginates out of the ectoderm to form a sac from which primary branches then migrate outwards. The invagination is driven partially by apical constriction mediated by Epidermal growth factor (EGF) receptor in response to the EGF Rhomboid (Llimargas and Casanova, 1999), and partially by the final round of mitosis that tracheal cells undergo simultaneously, which causes a release of tension due to cell rounding (Kondo and Hayashi, 2013). Tracheal cells arrest the cell cycle after this and most instead undergo endoreduplication to sustain their growth throughout the larval stages.

Once internalised, tracheal cells begin expressing the fibroblast growth factor (FGF) receptor Breathless (Btl), which is induced by Trh and remains expressed by most tracheal cells throughout the animal's life, guiding almost every migratory movement of tracheal cells from here on (Glazer and Shilo, 1991; Klämbt et al., 1992; Shishido et al., 1993). Btl signals through Dof (Imam et al., 1999; Michelson et al., 1998; Vincent et al., 1998) and the Ras-MAPK pathway (Reichman-Fried et al., 1994; Wappner et al., 1997) for these functions. Even before the last tracheal cell detaches from the ectoderm and closes off the invaginated sac, the already internalised tracheal cells begin adopting specific primary branch fates. These are defined at least in part by Knirps/Knirps-like and Spalt (Chen et al., 1998; Franch-Marro and Casanova, 2002; Kühnlein et al., 1994) and determine the cell number and tube size of each primary branch. As the germ band retracts, tracheal cells of each primary branch migrate towards sources of the FGF Branchless, which is stereotypically expressed by small groups of non-tracheal cells around the tracheal sac (Du et al., 2017; Ohshiro et al., 2002; Sutherland et al., 1996). This results, for each segment, in the migration of an anterior and posterior bud that meets its counterparts from the sacs of the neighbouring segments and fuses with them to establish the dorsal trunk (DT), the largest tracheal tube. The ends of the DT are formed by specialised dorsal and anterior spiracles, which establish contact between the prospective tracheal lumen and the external environment. Another bud migrates in interior direction towards the gut, establishing the visceral branch. Ventrally, the primary branch first establishes the transverse connective and then bifurcates. Of the two daughter branches, the anterior migrates across the segment boundary to meet the next tracheal metamer and establish the lateral trunk. The posterior daughter branch migrates towards the central nervous system at the ventral midline, establishing the ganglionic branch.

1.1.2 Dorsal branch morphogenesis and cell fate specification

Dorsally, a single bud of 4-6 cells migrates out towards the epidermis from each tracheal sac during primary branching. Out of the primary branches, this dorsal branch (DB) has received the most attention in past studies because its budding and migration process shares many aspects with sprouting angiogenesis in the vertebrate vascular system and therefore presents a valuable model system to study the underlying principles (Kotini et al., 2018). DB morphogenesis occurs in two steps that are divided in time by a ~2h period of apparent quiescence (Affolter and Caussinus, 2008). The first step is primary branch migration and occurs simultaneously to all other primary branching events during germ band retraction. Like other primary branches, it is primarily guided by a group of Bnl-expressing cells located dorsally to the tracheal sac. The DB cells move along the dorsal muscle precusors, which form a coincident groove to make space for them (Franch-Marro and Casanova, 2000). This groove appears before the DB cells migrate through it towards the epidermis, but whether it guides the migration along with the Bnl signal has not been shown. The dorsal primary branch remains a relatively short bud throughout germ band retraction, until dorsal closure begins. During the second migration event, two DB tip cells migrate in parallel to the leading epidermal edge and pull the remaining DB stalk cells behind (Caussinus et al., 2008). This also drives the stalk cells to intercalate, reshaping the DB from a multicellular tube where cells form epithelial junctions only with their neighbours, into an elongated unicellular tube in which each stalk cell is wrapped around the lumen and forms an autocellular junctional seam (Gervais et al., 2012). The tip cells are guided in this movement by a cluster of 4-6 epidermal cells that secrete Bnl and with which the DB tip cells establish physical contact (Du et al., 2017; Kato et al., 2004; Le Droguen et al., 2015). Once the DB approaches the dorsal midline, its movement slows and the two tip cells begin to show divergent behaviour. One tip cell, the fusion cell (FC) continues migrating in the dorsal direction, and the other, the terminal cell (TC) reverses its direction and forms a U-turn towards the embryo's lateral side. The FC subsequently establishes contact with the FC of its contralateral DB as dorsal closure concludes. The two FCs form epithelial junctions at their contact site and then hollow their cytoplasm with a new seamless lumen branching off the existing DB tubes and fusing at the contact site. Meanwhile, the TC begins the process of elongation and apical membrane invagination to initiate the subcellular seamless tube, which is the subject of my thesis. This process results in a similar DB morphology for the second to ninth tracheal metameres, with a thin dorsally fused tube and a TC located anterior to it. It is modified in the first and last tracheal metameres, which form much longer, multicellular dorsal fusions with a larger tube diameter and uniquely positioned TCs. These are known as the anterior and posterior anastomosis. By the time these dorsal processes have concluded, the remaining anatomy of the tracheal system has also been established. Prior to hatching, the tracheal cells perform coordinated pulses of secretion and endocytosis to clear the so far liquid-filled lumen of the tracheal tubes, and replace it with a gas of unknown constitution (Tsarouhas et al., 2007).

A question of much interest has been how the different roles of the cells in the DB are assigned. This again is achieved in two steps, the first resulting in distinct fates of tip and stalk cells, and the second resulting in the subdivision of tip cells into FC and TC. Prior to this, the specification of DB cells from the original tracheal placode (Ghabrial et al., 2003) is mediated by Dpp, expressed on the dorsal side of the embryo. This induces expression of the transcription factors Knirps and Knirps-related, which drive the assumption of the DB fate in the dorsal-most part of the tracheal sac (Chen et al., 1998; Vincent et al., 1997).

All DB cells are initially responsive to the dorsally located Bnl source and migrate towards it. The specification of tip and stalk cells during this process results from Btl sensing of Bnl, combined with Notch-mediated lateral inhibition. Btl, through the Ras-MAPK pathway, activates Mitogen-activated protein kinase (MAPK) to upregulate the expression of Delta according to each cell's proximity to the Bnl source. Delta signals through Notch in adjacent cells, which in response downregulates the neighbour's own expression of Delta by inhibiting MAPK. The two cells closest to the source retain MAPK activity (Schottenfeld et al., 2010), which feeds back positively onto Btl expression (Ohshiro et al., 2002). The stalk cells cease Btl expression due to the absence of this feedback. Transgenic induction of excess Btl signal in an individual DB cell leads this cell to become one of the two tip cells (Ghabrial and Krasnow, 2006; Lebreton and Casanova, 2016), indicating the role of Btl signalling in the competition of DB cells for the tip cell position. This competition mechanism is not robust to excess Bnl signalling induced transgenically, however, as this can cause all DB cells to eventually become TCs, one of the two downstream fates of tip cells (Sutherland et al., 1996). Similarly, in *notch* mutant embryos, all DB cells become tip cells (Ikeya and Hayashi, 1999), indicating the role of Notch signalling in determining the number of resulting tip cells.

After the DB group is subdivided into stalk cells and Btl-expressing tip cells, the second fate selection is the distinction of tip cells into FC and TC (Fig. 1.1A). This is determined by the dorsally expressed Wingless (Wg) and possibly other WNTs (Llimargas, 2000), as well as Dpp (Steneberg et al., 1999). Wg and Dpp specify the cell closest to their source as the FC and also drive this cell to inhibit its neighbours from acquiring the FC fate via lateral inhibition through Notch (Chihara and Hayashi, 2000; Steneberg et al., 1999). This is achieved by inducing the expression of the transcription factor Escargot (Esg) in the dorsal-most tip cell, which is responsible for most downstream programs related to the FC fate and inhibits Btl expression to prevent TC behaviour (Ghabrial et al., 2003). Wg also upregulates Delta expression in the FC, which activates Notch in the neighbouring prospective TC, where it suppresses expression of Esg. Tip cells that receive Notch signal continue expressing high levels of Btl and also begin expressing the definitive TC marker Drosophila serum response factor (DSRF) (Fig.1.1B).

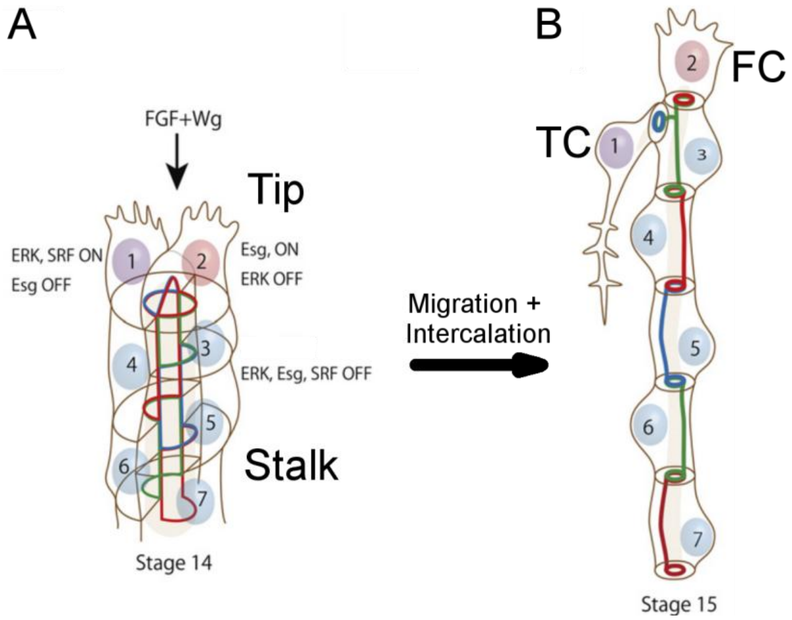

Figure 1.1: Fate specification between the two dorsal branch tip cells
After the primary branch migration event, the dorsal branches are subdivided into two tip and 4-6 stalk cells (A), due to FGF-induced Delta expression and migration in tip cells, combined with Notch-mediated lateral inhibition of their neighbours. Dorsally expressed Wingless and Decapentaplegic determine the tip cell closest to them as the fusion cell (FC) and induce expression of Delta and Escargot (Esg). Esg downregulates expression of the FGFR Breathless, thereby inactivating MAPK (ERK) and preventing the FC from adopting the TC fate instead. Delta inhibits the neighbour from expressing Esg via Notch. The remaining tip cell continues to receive FGF signal and in response upregulates Serum response factor (SRF), specifying it as a terminal cell (TC) (B). Meanwhile, the stalk cells rearrange their junctions to remodel the multicellular dorsal branch tube into a series of unicellular autojunctional tubes. Adapted from Hayashi and Kondo (2018).

1.2 Terminal cell morphogenesis

The processes described here are specific to the dorsal TCs, and different mechanisms determine both cell fates and branch direction of the ~300 TCs in an individual embryo, most of which are located at visceral branches throughout the tracheal system. The dorsal TCs are a popular subject of study due to their accessibility for imaging and the relatively large amount of background knowledge about the DB. Aside from their branch guidance, it is assumed that all remaining morphogenetic processes that have been studied in dorsal TCs are executed in a similar manner by all other TCs, since their resulting morphologies are mostly equivalent. Although each TC is located in a different anatomical environment and its extrinsic regulation of morphogenesis is therefore unique, so far there is no evidence to suggest that TCs in different anatomical locations employ different mechanisms to change their cell shape.

1.2.1 Embryonic terminal cell elongation

While the FC drives the final stages of dorsalward migration, the TC reverses its direction of movement and elongates in a U-turn in ventral direction. How exactly the

TC determines the direction of elongation has not been studied in much detail (Hayashi and Kondo, 2018). Btl activity is required by the TC throughout this process, but so far it has not been shown that a Bnl signal guides the direction of TC elongation as it guides all previous primary branching events as well as secondary branch migration such as in the DB. TCs are highly motile cells as a result of DSRF expression and Btl signalling, and they extend filopodia initially in random directions. The current model (Kato et al., 2004) is thus that to direct TC elongation, positional signalling factors selectively destabilise or stabilise filopodia that the TC has grown in the direction of the signal source. The known factors involved in TC branch guidance are Dpp, expressed dorsally, and Hedgehog (Hh), which is expressed in transverse stripes anterior to each DB. Dpp during this process inhibits TC motility, directing the elongation away from its source (Kato et al., 2004). This prevents TCs from crossing the dorsal midline. Hh acts in the opposite manner. It attracts TCs to its domain of expression in transgenic experiments, to the extent that TCs can reroute the entire DB in some cases. In the wild type this translates to a confinement of TCs to the Hh expressing region, defining a transverse stripe within which the TC remains. TC elongation in the ventral direction thus can be explained as a product of confinement to the Hh stripe and Dpp repulsion from the dorsal side (Kato et al., 2004).

As it elongates, the TC also invaginates a subcellular tube from its apical membrane at the contact site with the DB lumen (Sigurbjornsdottir et al., 2014). The TC thus remains attached to the DB stalk only by a ring of adherens and septate junctions that separates the apical domain, i.e. the subcellular tube, from the basal domain, i.e. the outer membrane that drives the cell elongation. Most of our knowledge about the subcellular tube pertains to its growth, and only little is known about the initial invagination event. The earliest observed event is the recruitment of centrosomes to the incipient site of invagination (Ricolo et al., 2016), but the subsequent steps to deform the apical membrane and begin its growth as a subcellular tube are unknown. Centrosomes organise the growth of microtubules both around the tube and ahead of it, towards the elongating basal edge of the cell. Microtubules are believed to serve both as trafficking mediators, guiding vesicles for delivery of membrane material to the tube, and as mechanical stabilisers for the tube (Sigurbjornsdottir et al., 2014). The tube is additionally lined by a cortex of actin, which contributes to its mechanical stability and determines its shape through actin anchors such as Moesin (Schottenfeld-Roames et al., 2014). It is also important for anchoring components such as microtubules and vesicles (Gervais and Casanova, 2010). Throughout TC elongation, the tube grows in concert with the cell, maintaining a more or less constant distance between its own tip and the migrating tip of the cell. A second pool of actin at the basal side of the cell forms the migratory filopodia and is also responsible for this alignment of the tube with the axis of elongation (Okenve-Ramos and Llimargas, 2014; Oshima et al., 2006). How precisely the length of the tube is kept in line with the size of the cell is not known. A so far unexplored factor in this process is the attachment of the TC to the underlying muscle tissue, which plays important roles for TC morphogenesis at least during the larval stages.

1.2.2 Larval terminal cell branching and tube shaping

By the time the larva hatches, TCs have elongated and grown their tube to more than twice their original length. This tube expands and becomes gas-filled along with the rest of the tracheal system before hatching. Throughout the three larval stages, TCs repeatedly bifurcate their cell body and the subcellular tube, combined with continuous extension of each branch (Baer et al., 2007). As a result of this ramification process, each TC forms a vast network of oxygen-delivering branches around the respective target tissue to which it attached during embryogenesis (Fig.1.2). In the case of dorsal TCs, these are the dorsal skeletal muscles. Each dorsal TC ramifies on the surface of one to three muscles, depending on the direction and length that its branches achieve. Most of this branching and growth occurs between the second larval moult and pupation (JayaNandanan et al., 2014).

The sprouting and extension of new branches is commonly considered to occur by essentially the same molecular mechanisms as the initial tube invagination and cell extension during the embryo (Sigurbjornsdottir et al., 2014). The most notable difference between the embryonic elongation process and the larval ramification process is their regulation by external signals. In the embryo, stereotyped systems that ultimately derive from the anteroposterior and dorsoventral positioning signals determine TC positions and guide their elongation towards their target tissue. In the larva, TC ramification is not stereotyped but instead responds to the dynamic oxygen needs of the target tissue (Jarecki et al., 1999). The mediator that directs terminal branches remains the same that guides tracheal branches throughout embryogenesis; the target tissues secrete Bnl, and TCs express Btl to sense it. However, rather than secreting Bnl in response to stereotyped patterning signals, Bnl secretion by target tissues is upregulated by the Hypoxia-inducible factor Similar (Sima), the central downstream readout of several hypoxia-sensing pathways (Cabernard et al., 2004; Gorr et al., 2006; Horowitz and Simons, 2008; Romero et al., 2007). Transgenically expressed Bnl can also attract terminal branches over long distance to tissues that have no adjacent TCs (Centanin et al., 2008; Jarecki et al., 1999). Btl thus induces the growth of branches, determines their growth direction, and also stimulates the branching and growth of the subcellular tube at the same time. However, a fine balance between branch and tube growth exists at physiological Bnl signal levels. Excess Btl signalling can result from transgenics or from high Bnl secretion due to a very low oxygen concentration in the environment. In these cases, Btl stimulates excessive growth of the tube beyond the length necessary to hollow each branch, and as a result the tube attains a wave-form shape and forms bundles near branching points or at branch tips (Centanin et al., 2008; Schottenfeld-Roames and Ghabrial, 2012; Ukken et al., 2014).

The connection between apical and basal membrane remains intimate also throughout larval TC morphogenesis. The formation and growth of new branches crucially depends on the continuous growth of the tube (Best, 2018), which in turn is subject to size regulation by the apical determinant complex around Par-6 (Jones and Metzstein, 2011) and depends on functioning membrane trafficking systems for the delivery of new membrane material to sustain its growth (Jones et al., 2014; Ríos-

Barrera et al., 2017; Schottenfeld-Roames and Ghabrial, 2012; Sigurbjornsdottir et al., 2014). The regular shape of the tube is maintained by the apical actin cortex that lines it throughout the cell's branch network (JayaNandanan et al., 2014). The mechanical constraints imposed by the actin cortex are modulated by Crumbs, which in many other tissues functions as an apical determinant, but in TCs appears to function primarily to recruit Moesin for anchoring the actin cortex to the apical membrane (Schottenfeld-Roames et al., 2014). Endocytosis at the apical membrane regulates the level of Crumbs present in it and thereby also impacts the mechanical properties of the actin cortex. Btl signalling is involved in these mechanisms and an excess of it can compensate for some deficiencies in apical actin stabilisers, but the Ras-MAPK pathway does not appear to be the downstream effector that mediates this function of Btl (Ukken et al., 2014). Throughout the third larval instar, TCs undergo an intense period of branching and growth (JayaNandanan et al., 2014). During this stage, they require Talin and Integrins to anchor branches to the target tissue (Levi et al., 2006).

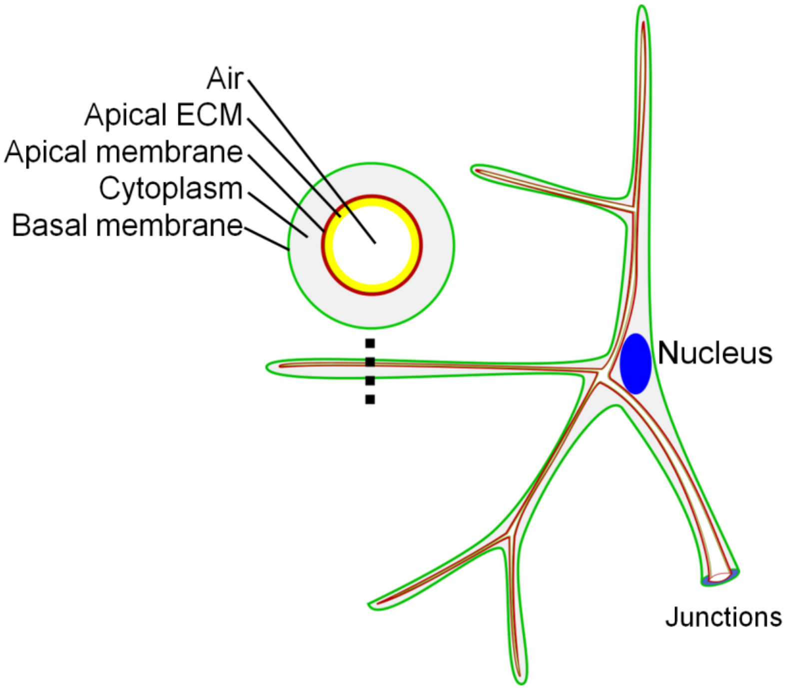

Figure 1.2: Terminal cell structure

Diagram showing spatial organisation of polarised membrane domains in larval terminal cells. The cell is attached to the secondary tracheal branch (e.g. the dorsal branch) by a ring of adherens and septate junctions at its stalk. The nucleus is typically located near the first branching point. The basal membrane (green) forms the outside of the branches, while the apical membrane (red) forms the subcellular tube. The lumenal surface is lined with an apical extracellular membrane for mechanical support, which forms transverse ridges called taenidia. The lumen is filled with air.

1.3 Membrane trafficking mediated by Rab GTPases

1.3.1 Compartmentalisation by endomembranes

The main function of the eukaryotic endomembrane system is the subdivision of the cell interior into discrete compartments. Endomembranes encapsulate volumes that are logically exterior to the cell, even if spatially they are suspended within the cytoplasm. This allows the creation of specialised microenvironments, for example through the modification of the pH within a vesicle, or by the addition of enzymes to the interior of a vesicle that modify its contents. Organising endomembranes requires the subdivision of proteins according to the logical compartment where they are required to perform their function: cytoplasmic, membrane-bound, or extracellular.

This is effected by localisation signals within the genetic sequence of the protein, which directs its mRNA to be translated either by cytoplasmic ribosomes or by those bound to the membrane of the rough endoplasmatic reticulum (ER) (Alberts et al., 2002). ER-translated proteins can be translocated during synthesis into the ER lumen or, if they contain an appropriate sequence, remain anchored in the ER membrane. Once synthesised, proteins cannot cross from the cytoplasmic into the extracellular space or vice versa without a specialised translocation mechanism. Together with the lipids of the membrane itself and other soluble molecules, membrane-bound and extracellular proteins constitute the trafficking cargo of the endomembrane system. The primary route for proteins to leave the ER is through COPII-dependent export to the Golgi apparatus, where many posttranslational modifications are effected and proteins with the same downstream destination are sorted together for further transport. The Golgi is broadly subdivided into *cis*, *medial* and *trans* compartments, through which proteins transition in this order. Proteins leave the Golgi apparatus from the *trans*-Golgi network in post-Golgi carriers of various shapes and sizes, which transport them either directly to the plasma membrane or to one of several types of endosomes, where they may be retained, or subsequently redirected to the plasma membrane. This constitutes the primary trafficking streams in the anterograde direction and also the primary secretory routes: ER to Golgi (to endosomes) to plasma membrane. In the retrograde direction, molecules taken up by endocytosis or other vesicle-internalising processes at the plasma membrane can be collected at an endosomal compartment for sorting, or returned to a Golgi compartment either directly or through endosomes.

While these models are useful guides for thought, the details of transport connections between the different compartments are often not understood and currently unknown routes remain to be discovered (Lee and Ye, 2018). There is also considerable diversity in the types of compartments that exist in different organisms and in different cell types within the same organism. This applies in particular to endosomes, of which there are many known subcategories that are only found in particular cell types. The consistent, overarching principle remains the compartmentalisation into cytoplasmic and external space. The function of membrane trafficking is the distribution of membrane-anchored and external material between the different logically external compartments, and the prevention of random flow across compartments due to entropy.

1.3.2 Rab GTPase mechanism of action

The Rabs are a family of small GTPases that insert into the cytoplasmic leaflet of endomembrane compartments and act as scaffolds for the recruitment of various effectors. Through their effectors, Rabs establish, maintain, and modify the identity and composition of the membrane they are bound to, as well as performing the basic actions of membrane trafficking such as coat protein recruitment, cargo sorting, vesicle budding, transport and fusion with a target membrane. The classic model of Rab function involves a switch-like mode of action, whereby the Rab can be bound either to GTP, placing it in its "active" state, or to GDP, the "inactive" state. The switching from inactive to active state is performed by interacting with a GTP exchange factor (GEF), and the reverse step is executed by a GTPase activating protein (GAP), which causes the Rab to hydrolyse its bound GTP (Fig. 1.3). Most Rabs are inserted into and removed from membranes by Rab GDP dissociation inhibitor (GDI), which binds GDP-bound Rabs with strong preference and promiscuity (Pfeffer, 2017). The activation by a GEF thus protects Rabs from being dissociated by GDI, assigning GEFs an important role in determining the compartments on which a Rab acts. Subsequently, the recruitment of effectors by the Rab further stabilises its presence on the membrane (Aivazian et al., 2006). In this manner, the Rab itself, its GEFs and effectors all reciprocally ensure each other's correct localisation and activity specific to each type of membrane compartment. Next to protein-based mechanisms, the mode of membrane insertion itself can also confer a Rab's compartment specificity. Additionally, many Rab functions involve not only interactions with other proteins but also the underlying membrane lipids, in particular phosphoinositide phosphates (PIPs) (Roth, 2004), and a growing number of Rab regulatory mechanisms that involve phosphorylation and other posttranslational modifications are being identified (Stenmark, 2009).

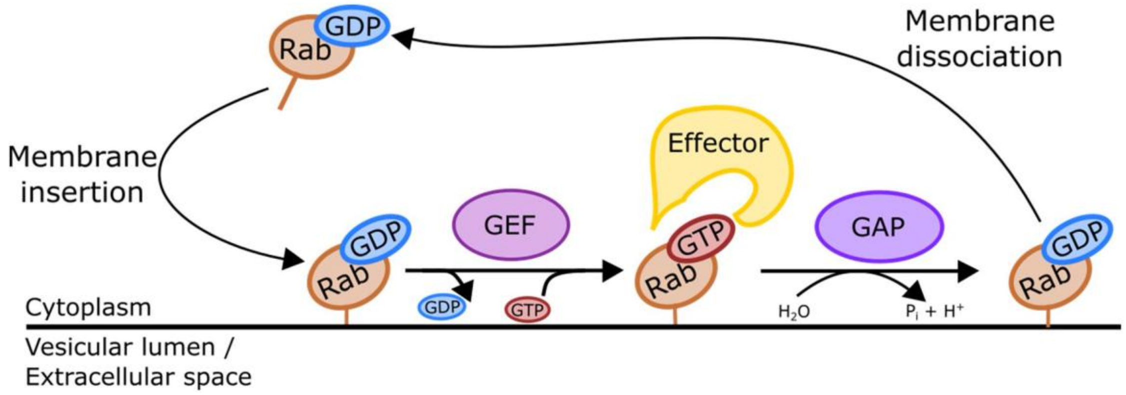

Figure 1.3: Canonical Rab switching cycle

Rab GTPases are thought to act like switches depending on the bound nucleotide. Cytosolic Rabs are GDP-bound and inactive. RabGDI (not illustrated) inserts and removes GDP-Rabs into membranes. A GTP exchange factor (GEF) removes the GDP of membrane-bound GDP-Rabs and transfers a GTP, thereby activating the Rab and stabilising its attachment to the membrane. The active GTP-Rab binds various effectors which execute the various trafficking functions such as vesicle budding, movement, tethering and fusion, or modify the membrane itself. To inactivate the Rab at the end of its pathway, a GTPase activating protein (GAP) induces the GTP-Rab to hydrolyse its GTP, thereby converting back to GDP-Rab, which may then be dissociated from the membrane.

1.3.2 The core Rabs and the rest

A small set of Rabs are considered the "core Rabs" (Fig.1.4). These Rabs are conserved across most of the eukaryotic kingdom and expressed by most cell types (Dunst et al., 2015). This comprises Rab1, Rab5, Rab6, Rab7 and Rab11. The *Drosophila* genome contains 28 further Rabs in addition to these, while mammalian genomes contain ~70 potential Rabs. Due to their evolutionary conservation, the core Rabs have become widely used as markers to identify which membrane compartment an unknown protein localises to. Their interactions with other proteins are commonly assumed to be conserved in *Drosophila*, although in many cases this has not been tested. The degree of conservation of expression and subcellular localisation has been studied for all Rabs in some exemplary *Drosophila* tissues using endogenous tagging (Dunst et al., 2015).

Rab1 localises to the interface of ER and Golgi and is best known for anterograde trafficking from ER to *cis*-Golgi, potentially through an ER-Golgi intermediate compartment in some cell types (Stenmark, 2009). In *Drosophila*, Rab1 depends on Tempura for its proper subcellular localisation (Charng et al., 2014). Tempura is a subunit of a Rab geranylgeranylate transferase (GGT) complex, a class of enzymes that provide many newly synthesised Rab proteins with a hydrophobic moiety for insertion into target membranes. *Drosophila* Rab1 is required for Notch trafficking (Charng et al., 2014), and in the trafficking of Integrins in S2 cells (Wang et al., 2010). Human Rab1 is involved in various cancers, primarily through its involvement in mTOR signalling (Yang et al., 2016).

Rab6 is reported with localisations at *trans*-Golgi membranes and post-Golgi vesicles. The precise mechanisms of actions of Rab6 are not clear yet, as it seems to be involved both in retrograde trafficking through the Golgi apparatus via COPI, and back to the ER (Liu and Storrie, 2015; Sandoval and Simmen, 2012), as well as in anterograde post-Golgi secretory trafficking, in which it cooperates with Rab8. This function is regulated by ARHGEF10 and effected through MICAL3 (Grigoriev et al., 2011; Shibata et al., 2016). In *Drosophila* accessory glands, Rab6 is crucial for forming secretion-related vacuole-like organelles (Prince et al., 2018) and in photoreceptors it is associated with apical secretion through recycling endosomes (Iwanami et al., 2016).

Rab5 is perhaps the most studied of all Rabs. It localises to the plasma membrane, endocytic vesicles, early endosomes as well as recycling endosomes, and its best known function is the integration or transformation of endocytic vesicles into early endosomes. Once recruited to the endosomal membrane, Rab5 is activated by its GEF, Rabex-5. GTP-bound Rab5 then recruits the PIP kinase Vps34 to promote the formation of PI(3)P in the membrane, which then together with Rab5 leads to the recruitment of Early endosome antigen 1, an effector responsible for endosome fusion among other functions (Mizuno-Yamasaki et al., 2012). In this capacity, Rab5 compartments receive EGFR and potentially other receptor tyrosine kinases when they are internalised from the plasma membrane (Bakker et al., 2017). From Rab5 endosomes, EGFR then progresses either to recycling endosomes and is returned to the plasma membrane, or to late endosomes and eventually lysosomes for degradation. These are considered the exemplary routes of endocytic trafficking. Rab5 is not necessarily uniformly distributed around an early endosome's membrane but can form discrete "microdomains", allowing the remaining membrane to be labelled instead by Rab4, which promotes direct recycling back to the plasma membrane from early endosomes (Zerial and McBride, 2001). Rab5 is also capable of converting either its microdomain or an entire vesicle into a late endosomal membrane in a so-called "Rab cascade" (Mizuno-Yamasaki et al., 2012). In this process, the GEF complex Mon1-Ccz1 is recruited by Rabex-5 and PI(3)P. At the same time, Rab5 recruits the Homotypic vacuole protein sorting (HOPS) complex, which binds Rab7 upon interacting with Mon1. Mon1 then activates Rab7, promoting maturation from an early endosome to a late endosome. In *Drosophila*, the fusion of endocytic vesicles into early endosomes relies on the Syntaxin7-homologue Avalanche (Lu and Bilder, 2005). This is mediated by the Rab5-effector Rabenosyn, which recruits Vps45, a Sec1/Munc18-family protein that interacts with Avalanche to promote fusion (Morrison et al., 2008).

Rab11 localises to endosomal recycling compartments, to a lesser extent on Golgi membranes and, as Rab5 overlaps with recycling endosomes, Rab11 also overlaps with early endosomes. Similarly to Rab4 and Rab5 on early endosomes, recycling endosomes can be subdivided into Rab4, Rab5 and Rab11 microdomains (Zerial and McBride, 2001). The main function of Rab11 is the generation of recycling compartments, as well as transport to and from them, which are a central crossroads in many anterograde and retrograde trafficking pathways. This places Rab11 as an important regulator of both the lipid and the protein content of the plasma membrane (Campa and Hirsch, 2017). As a result, Rab11 is a prominent target of exploitation both by viruses (Vale-Costa and Amorim, 2016) and bacteria (Mellouk and Enninga, 2016). Core effectors of Rab11 in vesicle trafficking include motor proteins for both microtubule- and actin-dependent vesicle transport such as Dynein light chain (DLIC), Kinesin family member 13A (KIF13A) and Myosin-5 (Myo5b), as well as the scaffold proteins of the Rab11 Family interacting proteins (Rab11-FIPs) (Campa and Hirsch, 2017) and the vesicle tethering effector, the octameric exocyst complex composed of Sec3, 5, 6, 8, 10, 15 and Exo70, 84 (Neto et al., 2013). Many Rab11 effectors require specific PIPs, most commonly PI(3)P, to bind the membrane and Rab11 function is therefore subject to regulation by the respective PIP kinases and phosphatases recruited also by other Rabs such as Rab5. Rab11 in *Drosophila* is involved in planar cell polarity, where it regulates plasma membrane sizes, junction recycling and signalling together with Rab4, Rab5 and Rab35. Its effectors in these processes include the exocyst complex and Nuclear fallout (Nuf / Rab11-FIP3), which recruits the dynein motor complex (Del Signore et al., 2017; Strickland and Burgess, 2004). It also, among others, supplies the furrow during cytokinesis with membrane (Strickland and Burgess, 2004).

Rab7 marks late endosomes, lysosomes and multivesicular bodies resulting from endosomal degradation. One important function of Rab7 is the recruitment of the retromer complex, which consists of Sorting nexin (Snx) dimers and a Vps26-Vps29-

Vps35 trimer (Seaman et al., 1998). The latter trimer binds transmembrane proteins in the endosome for retrieval to the *trans*-Golgi network. It is recruited as an effector of Rab7, while the Snx dimer binds PI(3)P on the endosomal membrane, which depends on prior recruitment of Vps34 by GTP-bound Rab5 (Rojas et al., 2008). Next to its role in targeting late endosomal contents to lysosomes, Rab7 is also involved in certain secretory routes that seem to pass through late-endosome-related organelles (Hirosaki et al., 2002). In *Drosophila*, among other functions, Rab7 is downstream of Rab5 in an endosomal-lysosomal biogenesis pathway (Jacomin et al., 2016), in nephrocytes is part of a triad with Rab8 and the methyltransferase ICMT, which enables Rab7 and Rab8 to secrete Notch by methylating them (Court et al., 2017), and the Rab5-Ccz1-Mon1-Rab7 cascade has been implicated in authophagy by a similar mechanism as retromer recruitment (Hegedűs et al., 2016).

Rab5, Rab7 and Rab11 together orchestrate the principal types of endosomes and regulate the flow of membrane, membrane proteins and cargoes through them. Most other Rabs have been associated with membrane compartments that they share with a core Rab, although some are also found on membrane structures not labelled by core Rabs, such as lipid droplets (Rab18) and mitochondria (Rab32). In most cases, data stem only from one or two model systems and the degree to which the information might pertain to *Drosophila* or any specific tissue cell type is speculative. However, broadly speaking for mammalian cells, Rabs 2, 8, 10, 14, 18, 19, 39 and 40 are considered at least partially Golgi-associated; Rabs 3, 8, 10, 14, 26, 27 and 32 are associated with secretory vesicles; Rabs 4, 10, 14 and 23 are associated with early endosomes; Rab9 with late endosomes; Rabs 27 and 33 with autophagosomes; and Rabs 35 and 40 with recycling endosomes (Hutagalung and Novick, 2011).

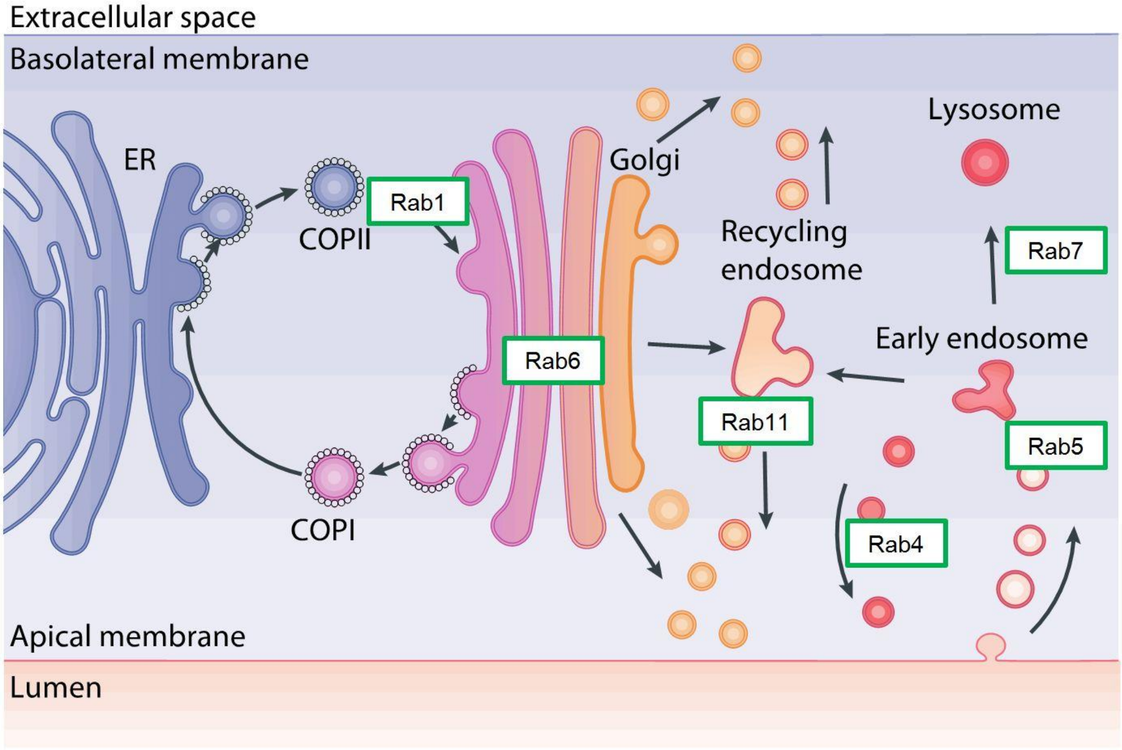

Figure 1.4: Primary trafficking routes associated with core Rabs

Rabs 1, 5, 6, 7 and 11 are considered the "core set" of Rabs due to their universal conservation across the eukaryotic kingdom. Rab1 regulates anterograde traffic from ER to Golgi. Rab6 maintains Golgi organisation and exports post-Golgi carriers. Rab11 converts endosomal membranes into recycling compartments which are used both in anterograde secretion and recycling, as well as retrograde shuttling to the Golgi. Rab5 acts in endocytosis (retrograde) and effects homotypic fusion of endocytic vesicles, forming early endosomes. Their contents may be recycled directly back to the plasma membrane by Rab4 (not a core Rab but widely conserved) or pass through Rab11 recycling endosomes first. Rab7 converts early into late endosomes and mediates their fusion with lysosomes. Adapted from Sigurbjornsdottir et al. (2014).

1.3.3 Rab8 in polarised trafficking

The GTPase Rab8 is of particular interest for my work due to its many functions related to polarisation of cells. Most data on Rab8 come from human cell culture and studies in mice, and their translation to *Drosophila* is complicated by three aspects. Mammals have two Rab8 isoforms (Rab8a and Rab8b) while *Drosophila* have only one, the *Drosophila* genome does not appear to contain homologues for many of the known regulators and effectors of mammalian Rab8, and the structures in which Rab8 is best understood, primary cilia, do not exist in *Drosophila* cells. Regardless, recent work has shown that particularly aspects of Rab8 function that were characterised in mammalian epithelial cell culture apply in similar forms to *Drosophila* epithelia.

The crystal structure of Rab8 in complex with Mss4 has been resolved (Itzen et al., 2006), a protein that binds multiple secretory and exocytic Rab proteins (Rabs 1, 3, 10, 18) (Wixler et al., 2011), and its interaction therefore suggested that Rab8 also acts in anterograde trafficking. The exact function of Mss4 seems to differ between physiological contexts. While traditionally it was considered a GEF for these Rabs based on in vitro studies, its ability to crystallise in complex with nucleotide-free Rab8, together with more recent evidence, suggests that in vivo contexts it may at least in some contexts act instead as a chaperone that protects Rab8, Rab10 and potentially others from degradation (Gulbranson et al., 2017). In accordance with this, Rab8 was found to participate in a membrane recycling pathway in HeLa cells, which redistributes membrane from the lagging tail to the leading edge during cell migration. This proceeds through the Clathrin-independent internalisation of macropinosomes guided by the small GTPase Arf6, which subsequently acquire GTP-bound Rab8. The compartments then elongate to tubular endosomal structures, transfer through the cytoplasm, and recycle the material back to the surface (Peränen, 2011). Rab8 is further involved in migration by modulating the actin cytoskeleton through Rac1 and RhoA, as well as by disassembling focal adhesions through calpain, matrix metalloproteases and Rho GTPases (Bravo-Cordero et al., 2016). Independent of this function, Rab8 in HeLa cells cooperates with Rab6 for secretory trafficking of exocytic vesicles to the plasma membrane. In this process, Rab6 recruits ARHGEF10 to post-Golgi carriers, which leads to recruitment of Rab8 (Shibata et al., 2017). Rab8 then enables the docking and fusion of the vesicle to the plasma membrane by recruiting ELKS and MICAL3 (Grigoriev et al., 2011).

One well-characterised function of Rab8 is its involvement in the generation of an apical membrane and subsequently the expansion of a multicellular lumen in 3D-cultured Madin-Darby Canine Kidney (MDCK) cells. This process begins with the formation of an apical membrane initiation site. This attracts the delivery of the apical polarity complex Par3-aPKC-Cdc42 as well as Par6 and Crb to promote its maturation into a pre-apical patch, all of which depend on Rab8 to fuse with the initiation site (Bryant et al., 2010). In this case, Rab8 is recruited to apical-destined vesicles and activated by Rabin8, a GEF that is first recruited by Rab11. The initial polarisation cue also induces the formation of $PI(4,5)P_2$ and the activation of Cdc42 to organise actin cables which may function as delivery tracks for Rab11-Rab8 vesicles by potentially Rab11-recruited myosins (Sigurbjornsdottir et al., 2014). The same apical delivery network around Rab11-Rab8 seems to be responsible for some cases of multivescular inclusion disease, whereby intestinal cells internalise or retain large apical vesicles with a fully matured villous structure (Sato et al., 2007).

Only a handful of studies have reported functions of Rab8 in *Drosophila*. Rab8 was first found in adult neurons to be downstream of the ESCRT-III complex, a component involved in endosomal degradation. Here, Rab8 is required to downregulate JNK and TGF-β signalling which otherwise promote excessive synaptic growth (West et al., 2015). An entirely independent function was found for Rab8 during early embryogenesis, prior to cellularisation. An endogenously tagged Rab8 showed striking dynamics, cycling between a vesicular distribution and a complete sequestration to the plasma membrane (Holly et al., 2015; Mavor et al., 2016), correlating with membrane furrows that are formed between nuclei each time they divide. The precise function of this Rab8 cycling is not yet known, but its dependence on Rab5, Rab11 and the exocyst complex suggested that Rab8 delivers membrane to supply for formation of these furrows. The Drosophila homologue of Mss4, Stratum, has been associated with polarised secretion functions of Rab8 by two different studies, one studying the follicular epithelium of egg chambers (Devergne et al., 2017) and the other studying the differentiation of precursor cells of the dorsal thoracic sensory hairs (Bellec et al., 2018). In the follicular epithelium, Strat acts as a Rab8-GEF and both proteins function to ensure that basement membrane proteins such as Collagen and Perlecan are not secreted apically. One point of confusion in this mechanism is that Strat protein was enriched on the basal side of the cells, while the membrane surface affected by its function is the apical side. In sensory organ precursors, Strat acts not as a GEF but potentially as a chaperone. Strat and Rab8 in these cells are required for the export of Notch and its trafficking partners from the Golgi, and similar to the follicular epithelium, their delivery to the appropriate plasma membrane domain. The findings mentioned above regarding the methyltransferase ICMT, which methylates Rab7 and Rab8 for the trafficking of Notch, were made in the wing disc (Court et al., 2017). Lastly, some aspects of the roles of Rab8 in HeLa migration seem to be conserved in *Drosophila* in Haemocytes, where Rab8 regulates filopodial and lamellipodial dynamics and promotes migration by secreting Laminins (Sánchez-Sánchez et al., 2017).

1.3.4 Roles of Rab GTPases in the tracheal system

While for most Rabs, it is not known whether Drosophila tracheal cells (and specifically terminal cells) express them, or what functions they might serve, a handful of Rab GTPases have been described. In all of these cases, the focus of the studies was on the effect of the Rab's activity rather than the mechanisms by which it performs its functions. During embryogenic tracheal development, Rab11 function depends on the nuclear protein Ribbon, which upregulates Crumbs expression and thereby downregulates Moesin activity at the apical membranes (Kerman et al., 2008). Loss of ribbon prevented the migration of the prospective dorsal trunk primary branches in the anteroposterior direction. This was proposed to be caused by a lack of Rab11 endosomes in the apical cortex and consequently insufficient supply of membrane material to the migrating front. Endosomes were suggested to be excluded from the apical actin cortex due to an increased rigidity resulting from excess Moesin activity. Rab11 also seems to play a role in the junctional remodelling of cells in the dorsal trunk and dorsal branches during cell intercalation around the same embryonic stages (Shaye et al., 2008). This depends on recycling of E-Cadherin from adherens junctions and is potentially mediated by the Rab11-FIPs Nuf and Rip11. Rab9 was shown to be important for the retention of the chitin deacetylase Serpentine in the tracheal lumen, a function that involves the retromer complex and the actin nucleator WASH as effectors and depends on cooperation with Rab5 (Dong et al., 2013). Since Rab9 regulates retrograde traffic, it was suggested that Rab9 via retromer either isolates Serpentine from endosomes before they transition into late endosomes for degradation, or allows Serpetine to progress from Rab11 recycling endosomes back into the secretory pathway at *trans*-Golgi compartments. The latter would imply that Serpentine has no Golgi-independent recycling route directly from endosomes to the plasma membrane. Prior to hatching, Rab5 is required to support the concerted Clathrin-mediated endocytosis of the liquid inside the tracheal lumen, allowing it to be replaced with gas (Tsarouhas et al., 2007). Rab7 and Rab39 were suggested to participate in a distinct secretory pathway in the fusion cells of the dorsal branches, which delivers apical material to the incipient fused tube through lysosomes (Caviglia et al., 2016). In this process, the small GTPase Arl3 recruits Rab39 to secretory lysosomes, which then recruits Staccato/Unc-13-4 to promote vesicle fusion.

The remaining data on Rabs in the tracheal system come from terminal cells (TCs) and pertain to Rabs 5, 10, 11 and 35. In TCs, Rab5 functions together with the early endocytic pathway that involves Dynamin, Syntaxin7, Rabenosyn and Vps45 at the apical membrane (Schottenfeld-Roames et al., 2014). Its precise mechanism of action or other functions in TCs, like for the other Rabs, is not known. However, its activity regulates the amount of Crb in the plasma membrane, which in turn regulates the recruitment of active Moesin to the apical actin cortex. The resulting modulation of the cortical mechanical properties ensures the regular and symmetrical shape of the subcellular tube. Rab10 and Rab11 were implicated also in subcellular tube development (Jones et al., 2014), though how they are involved remains unknown. Electron microscopy showed that they are required for the formation of the apical extracellular matrix in the lumen of the tube, and in case of Rab11 potentially for the growth of the tube itself. Rab35 was identified along with Whacked, a GAP whose human orthologues had caused some controversy regarding their specificity for Rabs or other small GTPases (Schottenfeld-Roames and Ghabrial, 2012). Whacked in the tracheal system acts as a GAP for Rab35 and is involved in the formation of subcellular TC tubes but not in the rest of the tracheal system. Both proteins are involved in regulating the amount of tube growth, and it was proposed that they act in a polarised manner that adds membrane to the tube specifically either to the beginning or end of branches.

2. Rationale, Aim and Structure

The size and morphology of terminal cells (TCs) prompt the question of how such large amounts of membrane material are distributed by the cell to ensure the proper relative sizes of the plasma and intracellular membrane compartments. Epithelial cells generally implement specific membrane trafficking routes related to their apicobasal polarity. However, TCs represent the only type of epithelial cell that invaginates its apical domain into its soma, shapes it into a tube and branches that tube repeatedly. My central hypothesis was that the processes that establish and maintain this unique structure are supported by membrane trafficking routes that do not exist, or work differently, in other cell types. To identify these pathways, the Rab family of GTPases were promising candidates to investigate, because Rab proteins fulfill many important roles in membrane trafficking. These include distributing membrane lipids and proteins to the different membrane compartments of the cell, regulating the sizes of membrane compartments, and secretion of extracellular biosynthetic products.

TC morphology has traditionally been assessed primarily using white light to image the contrast between the gas contained in the tubes and the liquid body of the larva, or by dissecting the larva and staining for a secreted marker such as Gasp (recognised by the 2A12 antibody). A third option has not been used much despite its ease of access: the apical extracellular matrix (aECM) on the lumenal side of tracheal cells is autofluorescent across the entire visible spectrum (Glasheen et al., 2010; Lin et al., 2008; A. Kern, M. Leptin, manuscript in preparation). Optimal and most practical excitation of the matrix autofluorescence is achieved with 405nm wavelength light sources, commonly equipped on microscopes for imaging DNA stains such as 4,6-diamidino-2-phenylindole (DAPI). The tracheal aECM shares this property with the epidermal cuticle, whose autofluorescence is substantially stronger. Like the cuticle, the tracheal aECM is a secreted product, and therefore a suitable readout for at least the secretory pathways of membrane trafficking. Additionally, since it lines the lumen of every tracheal branch, including those grown by TCs, it provides information on the tracheal tubes. Like the white light contrast of gas in the lumen, autofluorescence from the aECM only gives positive information, i.e. if it can be observed, it indicates the presence of a tube. Its absence, however, does not necessarily indicate the absence of a tube or a lumen (Best, 2018), and the tracheal membrane tubes are not necessarily of the same shape as the aECM as evidenced for example by excess Crumbs activity, where the membrane itself forms dilations, but the autofluorescence remains normally shaped (Schottenfeld-Roames et al., 2014). The morphology of the TC's soma has not received much attention in the past because its primary use has been as a model to study tube formation. Unlike the tube, there is no endogenous way to make the soma visible. Throughout my studies I therefore co-expressed a fluorescent protein along with other transgenes of interest under the trachea-specific driver *btl*-Gal4 to visualise the cytoplasm.

The core aim of this study was to use the library of fly lines with endogenously YFP-tagged Rabs (Dunst et al., 2015) to conduct a knockdown screen by targeting the tag instead of any *rab* gene specifically. There are two key benefits to this method. First, a strong control against false positives can be achieved by knocking down YFP in flies without any YFP-tagged gene. Second, due to equivalence of the method applied to different target genes, the resulting phenotypes can be quantitatively compared, permitting a system-level analysis. Implementing this simple idea posed two major challenges: First, the genetics to obtain the correct *Drosophila* lines for the knockdown screen required diverse unexpected adjustments for individual Rabs, which are detailed in the Methods chapter. More importantly, the groundwork for systematic analyses of phenotypes had not been done for TCs, particularly related to their subcellular tube, which manifests phenotypes in an unusual manner as described below. This resulted in a three-part structure to my project, first untangling the complex nature of tube-related TC phenotypes, second performing the YFP-mediated Rab knockdown screen, and finally following up on the results of the screen and investigating the function of the membrane trafficking pathways identified.

The structure of this thesis reflects these three main parts. The first part is a phenomic study. I used RNA interference (RNAi) constructs targeting known genes related to TC tube morphogenesis to systematically assess the range of defective morphologies and identify quantitative methods to interpret them. TCs pose unique challenges for assessing phenotypes. Their branches cover a very large area which needs to be imaged at high resolution to observe phenotypes of the micrometer-size tubes. On the semantic side, defect phenotypes of terminal tubes are often highly variable between different branches of the same cell, with some branches showing a normal morphology and others showing severe abnormalities. This contradicts the default assumption that all branches form by the same mechanism, and that the molecules that execute branch growth are uniformly distributed by the cell across its branches. Mutant phenotypes in TCs therefore have two layers of penetrance: the percentage of TCs that manifest the phenotype at all, and the percentage of branches that manifest the defect within affected TCs. Both of these are subject to developmental variability both between TCs within one animal, and between different individiuals. Various analytical techniques that have been used in agricultural science to quantify and interpret variable phenotypes are collectively denoted "phenomic analysis" (Furbank and Tester, 2011). Testing these methods, I found that they allow extracting meaningful interpretations where the traditional paradigm of "same phenotype, same function" is problematic because of partial penetrance, and because genes of unrelated functions cause qualitatively similar defects.

The second and main part of this thesis is the YFP-mediated Rab knockdown screen. Its objective was to express a knockdown construct targeting YFP in the tracheal system of larvae whose two alleles of a *rab* gene are endogenously tagged with YFP. I assumed that having only one allele - and therefore only a fraction of the *rab* gene product - tagged and hence knocked down would be insufficient to cause any phenotype. The morphology of TC tubes in these animals was then to be quantified and analysed using the methodology established in the preliminary study. The results from this screen were surprising in several ways, and required follow-up experiments to substantiate their interpretation. The main outcome of the screen was that TCs use only two Rab-mediated trafficking pathways that are sensitive to changes in protein levels of the Rabs involved in it. The first pathway was unique to Rab8, while the other involved Rab2 and Rab6, as well as potentially several other Rabs whose functions were less sensitive to a reduction of the Rab's protein expression.

The third and final chapter of this thesis describes the relationship between the two identified pathways, exemplified by Rab8 and Rab6. Since Rab8 appeared to perform a unique function related to tube morphogenesis, I further investigated its function in TCs with classic genetic approaches, primarily Gal4-induced expression of tagged proteins and combinations of RNAi constructs in experiments similar to traditional mutational epistasis assays. I found that Rab8 primarily occupies endosomal membranes and is involved in polarised delivery of protein cargos downstream of the Golgi apparatus.

All phenotypes were assessed in a defined subset of TCs that are easily accessible for imaging, and the generalising assumption is made that the findings of this work also apply to all other TCs. I focussed specifically on the dorsal TCs, whose branches are attached to the dorsal skeletal muscle. Each larva has eight pairs of dorsal TCs, one pair per tracheal segment, of which the third to sixth pair were observed (positioned in the larval abdominal segments 1-4). The first, second, seventh and eigth pair were excluded to reduce noise, because their anatomical environments have substantially different shapes and sizes, which alters their branch numbers, thickness, tube size and branching patterns.

3. Materials and Methods

3.1 Fly strains and rearing

All fly culture and non-experimental husbandry were at 25°C according to standard procedures. Finalised lines were kept at 18°C for maintenance. The culture medium was prepared according to a standard cornmeal-agar recipe and provided by EMBL.

Table 3.1 Drosophila lines

Name	Genotype	Source / Reference
w-	w[1118]; +; +	Lab resource
DblBal	w[1118]; If/CyO; MKRS,Sb/TM6b,Tb,Hu	Lab resource
Btl>DcrGFP	w*; UAS-Dicer2; btl-Gal4, UAS-GFP	Lab resource
SRF>Ch	w*; +; DSRF-Gal4, UAS-mCD8.mCherry	Lab resource
Oregon-R	Wildtype	S. De Renzis
Rab8-IR	w[1118]; P{GD12520}2/CyO,dfd-YFP; +	VDRC (#28092)
Rab5-IR	w[1118]; P{KK102895}VIE-260b;	VDRC (#103945)
Syx7-IR	w[1118]; P{GD2767}3;	VDRC (#5413)
Talin-IR	w[1118]; P{GD12050}3;	VDRC (#40399)
en>Ch	w[*]; P{w[en2.4-GAL4}e16E, P{UAS-mCherry.NLS}2;	Bloomington (#38420) (Ma et al., 2017)
Btl>DsRed	w*; If/CyO; btl-Gal4, UAS-DsRed1/TM6,Hu	Lab resource
GFP-IR-I	w*; UAS-GFP-IR-1;	NIG-Fly (NM_00GFP)
GFP-IR2	y[1] sc[*] v[1]; P{y[+t7.7] v[+t1.8]=VALIUM20-EGFP.shRNA.3}attP40;	Bloomington (#41559)
NanoP	y[1] w[*]; P{UAS-Nslmb-vhhGFP4}2;	Bloomington (#38422)
NanoM	y[1] w[*]; M{UASp-Nslmb.vhhGFP4}ZH-51D	Bloomington (#58740)
YRab(1-X6)	w[1118], Rab[YRab];; or w[1118]; Rab[YRab]; or w[1118];; Rab[YRab]	M. Brankatschk (Dunst et al., 2015)
Rab1^{S}	w*; P{neoFRT}82B P{lacW}Rab1[S147213]/TM3, Sb1	Bloomington (#37735) (Sechi *et al*., 2017)
Rab7^{d1}	w*;; P{neoFRT}82B Rab7[d1]/TM6b,Tb,Hu	G. Juhász (Hegedűs *et al*., 2016)
Rab11	w*;; P{lacW}Rab11[j2D1]/TM6,Hu	Kyoto DGGR (#111420) (Chen *et al*., 2005)
Btl-MARCM	y* w* hsFlp; btl-Gal4, UAS-GFP; FRT82B, Tub-Gal80	Lab resource
Rab6-IR	w[1118]; P{KK108556}VIE-260b;	VDRC (#100774)
RFP.Rab8^{WT}	w*;; P{UAST-tagRFP.Rab8}	Lab resource
RFP.Rab8^{CA}	w*;; P{UAST-tagRFP.Rab8[Q67L]}	Lab resource
Strat-IR	P{KK107973}VIE-260B	VDRC (#105730)
Crb-GFP	w*;;Crb[GFP-A]	M. Brankatschk (Huang et al., 2009)

3.1.2 Generation of 54 transgenic lines for YRab-gfpIR

For the YRab-gfpIR screen, I used the library of endogenously YFP-tagged Rabs (Dunst *et al*., 2015). This consists of 27 Drosophila lines, each carrying an N-terminal YFPMyc insertion in one endogenous Rab locus (known as the YRab allele). These lines were generated by homologous ends-in recombination. Most YRab lines were homozygous viable. A small number required a balancer chromosome to maintain a viable population: YRab10 is located on the X chromosome and was balanced using *FM7c,B*. YRab2, YRab5 and YRabX1 are located on the 2nd chromosome and were balanced with *CyO*. YRab8, YRabX4 and YRabX5 are located on the 3rd chromosome and were balanced with *TM6b,Tb,Hu*. After finalising the decision to use the GFP-IR-I construct and the Btl>DsRed driver, 54 new lines were derived, two lines from each YRab line: One "YRab,IR" line (e.g. *w*; GFP-IR-I; YRab11*) and one "YRab,Gal" line (e.g. *w*; YRab3; btl-Gal4, UAS-DsRed1/TM6b,Tb,Hu*). The btl-Gal4 driver in this line is the same insertion as in the btl>DcrGFP line used in the phenotype study, according to lab records. All YRabs on the second chromosome were recombined with the GFP-IR-I construct, while all YRabs on the third chromosome were recombined with the btl-Gal4 and the UAS-DsRed1 construct (see Appendix). For the YRab,Gal lines, potential recombinant F1 larvae were screened for tracheal DsRed fluorescence under an epifluorescence microscope. The presence of the YFP tag could already be identified as green larval fluorescence for YRabs1, 3, 6, 8 and 11. For both YRab,IR and YRab,Gal lines, initially 30 potential recombinant orange-eyed F1 males were individually crossed to DblBal virgins, allowed several days to fertilise, and then removed from the vials for genotyping.

At least two stable lines were established for each recombination from crosses where the male was genotyped YRab-positive. The location of insertion was not known for any of the three constructs, and it was therefore not possible to calculate expected recombination rates *ab initio*. Several YRabs required considerably more screening beyond the first set of 30 until recombinants could be identified. Second chromosome YRab recombinations with GFP-IR-I were trivial because no larval selection step was required, eliminating a bottleneck on the number of potential recombinant progeny. Regarding recombinations with btl-Gal4 and UAS-DsRed, the observed recombination rates suggest that UAS-DsRed is inserted close to the centrosome of chromosome 3, most likely on 3L near the Rab8 locus, and btl-Gal4 is inserted on 3R, close to the RabX4 and Rab7 loci. For YRab8, YRab23 and YRab26, no recombinants carrying both the btl-Gal4 and the UAS-DsRed construct could be identified. I only obtained flies of the genotype *w*;+ ; YRab,btl-Gal4* for these as evidenced by crossing the established lines to simple btl-Gal4 or UAS-GFP lines and testing for tracheal DsRed or GFP respectively. Conversely, YRabX4 generated several *w*;+ ; YRabX4,UAS-DsRed1* recombinants and, very rarely, the desired *YRabX4,btl-Gal4,UAS-DsRed1* recombination. This, together with data from the other Rabs (all of which had higher recombination rates), suggests the abovementioned locations.

Some homozygous viable YRab alleles were no longer viable in lines that carried either the GFP-IR-I or the Btl>DsRed constructs. To allow screening experimental crosses against the balancer at larval stage (thereby ensuring that the prepared larvae are YRab-homozygous), inviable YRab,IR chromosomes were balanced with a YFP-labelled CyO balancer and inviable YRab,Gal chromosomes were balanced with TM6b,Tb,Hu. Particular challenges were posed by YRab10, located on the X chromosome. This line was homozygous inviable and originally balanced with FM7c,B. This was replaced with a GFP-labelled FM7i balancer to allow selecting against balancer-containing larvae in experimental crosses. However, the YRab10,Gal lines generated from lost the YRab10 allele and the FM7i balancer after 3-4 generations. Yet, the *YRab10/FM7i,y*,w*,actin-GFP* and the YRab10,IR lines maintained the balancer and the YRab10 allele properly. The same loss of YRab10 and FM7i was observed in a line of genotype *YRab10/FM7i,y*,w*,actin-GFP; +; MKRS,Sb/TM6b,Tb,Hu*, suggesting that the presence of TM6b can cause the FM7i balancer to recombine. I therefore generated a line using a TM3 balander instead. The resulting *YRab10/FM7i,y*,w*,actin-GFP; +; btl-Gal4,UAS-DsRed1/TM3,Ser* line maintained its genotype for at least 15 generations.

3.2 Experimental crosses

Unless otherwise specified, experimental crosses were carried out at 29°C to maximise expression of desired transgenes induced by Gal4 drivers. Each set of parents consisted of 15-25 virgins and 5-10 males, which aged separately for 2 days after collection. Once fertilised, the parents were transferred to a fresh vial every 2 days to prevent overcrowding. Larvae were generally staged by size, behaviour and spiracle morphology.

Unless otherwise specified, wandering third-instar larvae were used; they were identified by selecting larvae which had left the food and ceased actively crawling around on the vial, with protruding anterior spiracles. I excluded larvae already undergoing early pupation by their response to touch. Larvae which did not begin moving after being picked off the vial wall were not analysed. Selected larvae were collected in deionised water and screened against TM6b using the Tb marker, and if present in the cross, against CyO and FM7i using the *dfd*-YFP and *act*-GFP markers respectively. In my experience, all of these markers are fully penetrant.

3.2.1 Crosses for phenomics and validation of RNAi constructs

To guarantee the correct genotype in progeny larvae, virgins of each RNAi line were crossed to Gal4 driver males. Btl>DcrGFP was the default driver line. For the control, w^{1118} virgins were used. Each cross was performed with one set of parents at 29°C and with another set of parents at 18°C. For Syx7-IR, the coexpression of Dicer2 caused full lethality. Using males of the Btl>GFP line (without the UAS-Dicer2 construct), I obtained some surviving wandering Syx7-IR larvae at 18°C but none at 29°C. These larvae were roughly 20% shorter than control L3 wandering larvae but had branched anterior spiracles typical of late L3 larvae. Rab5-IR produced no viable larvae even without the Dcr2 construct and was therefore crossed to the SRF>Ch line, which drives expression only in the terminal cells instead of the entire tracheal system.

The Rab5-IR and Syx7-IR constructs (Schottenfeld-Roames *et al*., 2014) as well as Strat-IR (Devergne *at al*., 2017) were previously tested. The Talin-IR construct was validated here by comparing its associated TC phenotype to the phenotype published for *talin* mutants (Levi *et al*., 2006). The Rab8-IR construct was validated here both by comparing its associated TC phenotype with the TC phenotype in YRab8-gfpIR, as well as by co-expressing UAS-tagRFP.Rab8, which resulted in full rescue (data not shown).

3.2.2 Crosses for YRab-gfpIR screen

All crosses were performed using virgins from the YRab,IR line and males form the corresponding YRab,Gal line. Where viable and fertile, YRab-homozygous virgins were used. If only the YRab,Gal line produced suitable females, virgins were used from that line instead. For YRabs 2, 6, 8, 10, X4 and X5, neither line produced fertile YRab-homozygous females. YRab6-gfpIR crosses had no viable progeny when cultured at 29°C and were therefore instead kept at 25°C.

3.2.3 Crosses for MARCM

Virgins with a Flippase Recognition Target (FRT) sequence on the right arm of chromosome 3 (FRT82B), followed by a null *rab* allele, were crossed to Btl-MARCM males (which express Flippase inducible by heatshock, btl-Gal4 and UAS-GFP, as well as the Gal4 suppressor Gal80 under the *tubulin* promoter downstream of an FRT82B site) and kept in vials at 25°C for 4-5 hours before transferring to a new vial. The collected embryos were heatshocked at 37°C for 45min to induce expression of Flippase and the vials were then returned to 25°C until third-instar larvae began wandering up the vial walls.

3.2.4 Crosses for epistasis experiments

To test epistasis by targeting two Rabs simultaneously with YRab-gfpIR, additional lines were generated; again two lines per YRab combination. All combinations tested were between Rabs located on different chromosomes and therefore did not require further recombinations. The previously described complications of YRab10 recombining with the GFP-labelled FM7 balancer and its general low viability again made it impossible to keep stable lines for the YRab10/YRab11 combination; unbalanced GFP-IR virgins and Btl>DsRed males were instead generated and F1 larvae were genotyped after imaging to ascertain YRab homozygosity. The experimental crosses themselves were carried out as above for YRab-gfpIR. The final genotypes of the parents used are described in Table 3.2.

Table 3.2 Parental genotypes in double-YRab-gfpIR crosses

Combination	Maternal genotype	Paternal genotype
YRab4/11	$\text{w}^{*};\frac{\text{YRab4,GFP-IR-I}}{\text{CyO,dfd-YFP}};\text{YRab11}$	$\text{w}^{*};\text{YRab4};\frac{\text{YRab11,}\textit{btl}\text{-Gal4,UAS-DsRed1}}{\text{TM6b,Tb,Hu}}$
YRab10/11	$\frac{\text{w}^{*}\text{,YRab10}}{\text{FM7c,y,w,B}};\frac{\text{GFP-IR-I}}{\text{CyO,dfd-YFP}};\frac{\text{YRab11}}{\text{TM6b,Tb,Hu}}$	$\text{w}^{*}\text{,YRab10;+;}\frac{\text{YRab11,}\textit{btl}\text{-Gal4,UAS-DsRed1}}{+}$
YRab11/35	$\text{w}^{*}\text{,YRab35;GFP-IR-I;YRab11}$	$\text{w}^{*}\text{,YRab35;+;}\frac{\text{YRab11,}\textit{btl}\text{-Gal4,UAS-DsRed1}}{\text{TM3,Ser}}$

For crosses testing Rab8 interactions with Rab6 and Strat, I first generated a "8IR,DsRed" driver line by crossing Rab8-IR and Btl>DsRed, with the resulting genotype of *w*; Rab8-IR/CyO,dfd-YFP; btl-Gal4, UAS-DsRed1/TM6b*,Tb,Hu. Obtaining this line was only possible by maintaining crosses at 18°C as the RNAi transgene is otherwise driven at lethal levels by Gal4. Virgins from the Rab6-IR and Strat-IR lines were crossed to 8IR,DsRed males. Crosses were cultured at 29°C as for YRab-gfpIR experiments. Non-Tb third instar larvae were screened for dfd-YFP to obtain control larvae expressing only Rab6-IR or Strat-IR, while dfdYFP-negative siblings co-expressed the same and Rab8-IR.

3.3 Sample preparation

3.3.1 Heat fixation

Heat fixation was used for all crosses assessing terminal cell phenotype (as opposed to protein localisation) because this method is vastly more time-efficient than dissection, and previous experience in the lab indicates that this method is less likely than chemical fixation and dissection procedures to impact terminal cell morphology or create artifacts. The selected larvae were heat-fixed by transferring to a cover slip with halocarbon oil 27 (Sigma), which was placed for 45s on a heatblock pre-heated to 65°C. A brush was used to spread the larvae out on the cover slip and mount them anterior-up and dorsal facing down on the cover slip.

3.3.2 Dissection and immunostaining

Dissections were performed for assessing YRab endogenous protein expression. Third-instar wandering larvae were taken from YRab line vials cultured at 25°C, cleaned in distilled water with a brush, and then transferred into phosphate-buffered saline (PBS) on a dissection dish. Larvae were dissected according to published protocol (JayaNandanan et al., 2014) and fixed in 8% paraformaldehyde at room temperature for 15min followed by washing in PBS. The filets were then transferred to a glass dish for all further treatments. First, they were incubated with blocking buffer, a 1% weight/volume bovine serum albumin solution in PBS, at room temperature for at least 45min. Primary rabbit anti-GFP and secondary Alexa568-conjugated anti-rabbit antibodies were diluted 1:500 in the same blocking solution. Blocking was followed by overnight incubation with primary antibody solution at 4°C and three washes (10min) in PBS at room temperature. Secondary antibody incubation was for 1h at room temperature, followed by three washes. The filets were mounted on a glass slide in VectaShield medium with diamidino-phenylindole (DAPI; Vector Laboratories) and topped with a coverslip, which was then sealed using nail polish for preservation. The five anti-GFP antibodies tested were: A-11122 (Thermo Fisher), TP401 (Torrey Pines Biolabs), mAb anti-GFP (Upstate Biotec), Ab290 (Abcam) and antiGFP 598 (MBL). A-11122 was used for reported stainings. Paraformaldehyde concentrations of 4% and 8% were tested, with no significant difference in their result. During a single session, two to three larvae each from five candidate YRabs were dissected and stained in parallel, plus two YRab1 larvae as positive controls for staining quality and two w^{1118} larvae as negative controls.

3.3.3 Larval anaesthesia

Anaesthesia was used to obtain time-lapses of live terminal cells, but also to assess protein localisation with maximum fidelity. For this procedure, larvae of the desired stage (Mid-L3 for time-lapses, wandering L3 for protein localisation) were washed in distilled water, dried by blotting on tissue paper, and transferred into an anaesthesia chamber as published (Kakanj et al., 2016). In this chamber, the larvae were exposed to diethyl ether (Merck) vapour for 2min 45s. They were then transferred to a coverslip coated in a thin film of halocarbon oil and mounted as after heat fixation. Each larva's response to anaesthesia could range from remaining mobile to dying, making it necessary to repeat the procedure until a larva was obtained where the body wall muscles had fully arrested movement, but the heart was still pulsing, or the head twitched occassionally as evidence of survival.

3.4 Confocal fluorescence microscopy

3.4.1 Microscope setups

The microscopes used were Zeiss model LSM780 or LSM880 inverted confocal laser scanning microscopes with identical manufacturer standard setups. This included, briefly: a diode laser for 405nm excitation of tracheal extracellular matrix autofluorescence and DAPI, an Argon laser for 488nm excitation of GFP and YFP and a DPSS 610-1 laser for 561nm excitation of DsRed and tagRFP, as well as a transmission photomultiplier tube detector (T-PMT, Zeiss) to detect transmitted light. Laser reflection was excluded using a dichroic mirror and two filters with narrow exclusion bands around the excitation wavelengths. Emitted fluorescence was detected with a PMT detector (autofluorescent emission at 410-498nm), a GaAsP spectral detector (YFP emission at 498-533nm) and a second PMT detector (DsRed emission at 611-697nm). When all three colours were imaged simultaneously, the channels were split into two tracks to exclude bleed-through from autofluorescence into the YFP channel and cross-excitation of DsRed. For terminal cell imaging, the objective used was a Plan-Apochromat 63X/1.4 Oil DIC M27 (Zeiss). For scoring dorsal tracheal anatomy phenotypes, a 20X Air Objective (Zeiss) was used as this allows a greater imaging depth, necessary to trace the sometimes very deep dorsal anastomoses. The LSM880 microscope was additionally equipped with an Airyscan detector module (Zeiss), which was used in Hi-Res mode for live timelapses and colocalisation microscopy.

3.4.2 Experiment-specific settings

For phenotype assessments, laser intensities and detector gains were adjusted for each cell to obtain optimal signal-to-noise ratios. This was admissible because the absolute quantitative information of emission intensity was not relevant for the analysis and therefore did not need to be controlled across samples. 3D-stacks were acquired at a voxel size of 220nm x 220nm x 1µm with a 1.5µm step size between slices and 1024x1024 pixel field of view. This resolution is not the optimum achievable, but represents a compromise in the interest of time investment while maintaining a resolution that allows identifying defects in the autofluorescent extracellular matrix. In most cases, a single field of view (225µm length, the maximum possible with this hardware) was not sufficient to capture an entire TC, and multiple separately acquired stacks needed to be stitched (see section 3.5.1).

For all other purposes, pictures were taken at optimal pixel resolution for the desired zoom as determined by the Zen software (Zeiss). To quantify YRab expression from stainings, all terminal cells on one microscopy slide were imaged in a single microscopy session and with the same technical parameters to ensure consistency across samples for quantification of staining intensity. Live-imaging was performed on the LSM880 using the Airyscan detector as described in section 3.4.1. In this case, a single colour channel was set up optimised for imaging tagRFP or YFP. In each case, the epidermis, which is close to the surface, contained some cells that strongly express the fluorophore. These cells were used to calibrate the Airyscan detector because a bright signal is required for this purpose. The calibrated detector was then used to detect the weaker signal found in terminal cells.

3.5 Image analysis

3.5.1 Image processing

Timelapses taken with the Airyscan detector were deconvolved using the Airyscan processing function in the Zen software and automatically optimised settings. Images to be analysed for terminal cell phenotypes were imported in FIJI (Schindelin et al., 2012). The Pairwise Stitching plugin of FIJI (Preibisch et al., 2009) was used to fuse images for cells that required multiple fields of view. To compute the overlap between the two images, a small ROI with a recognisable structure was selected on each picture and a Check Peaks setting of 5 was used. The images were fused using the maximum method, which for each pixel in the overlap region retains the higher pixel value of the two original images. For displaying the autofluorescence in terminal cells in figures, confocal stacks were manually edited in FIJI to remove autofluorescence from the larva's cuticle, and from other tracheal branches appearing at deeper levels. In each slice, the region containing cuticle was selected and the selected pixels' values were set to 0. These are unproblematic manipulations because at any given focal plane, there is sufficient distance between terminal branches and the epidermis to identify and selectively erase the cuticle.

3.5.2 Quantification of staining intensity

To quantify YRab protein expression, a simple segmentation method was implemented in FIJI: A Gaussian blur filter was applied to the staining channel (561nm fluorescence) to close gaps between more and less intensely stained regions. The resulting image was thresholded to obtain a mask of the terminal cell. A second region outside the terminal cell was chosen to measure detector noise. The mean intensity in the background region was then subtracted from the mean staining fluorescence intensity of the cell region for each cell to obtain a proxy of staining level. The resulting values for each YRab were compared to the negative control cells recorded in the same microscopy session.

3.5.3 Phenotype scoring

Terminal cell phenotypes were scored manually by tracing each branch from the stalk to the tip, noting occurrences of the different morphological feature classes throughout the process. I kept count of the number of tips and recorded this as the total branch number for each cell. Any branch which showed none of the features was counted as a "healthy" branch. For this purpose, the beginning of a branch was its tip, and the end was determined by tracing backwards through the branching points to the stem of the cell. At branching points, there is usually one daughter branch whose autofluorescence is thinner, and whose angle to the parent branch is close to 90°, while the other daughter branch has a similar thickness as the parent, and has an angle closer to 180°. The upstream segment was considered part of the thicker daughter branch. In cases where the difference was not clear, the parent was assigned to one daughter by coin toss.

The scoring for phenomic analysis was blinded by first assigning each image file a name consisting of larva ID, dorsal pair number, genotype, culture temperature and date. All files were then collected into a single folder and a Batch script was used to rename the files with random sequences of letters and digits. The script also creates a text file containing the mapping from original file names to the randomised names. Phenotype scores were labelled using the randomly named files, and additionally a guess for genotype and culture temperature was recorded for each cell. After all cells were scored, the text file was used to complete the scoring table with the original file names, from which the different sample identifiers could be extracted. Phenotypes related to dorsal branch anatomy were recorded manually during the microscopy session to reduce the amount of stored image data.

3.5.4 Colocalisation analysis

Particle-wise colocalisation was quantified using FIJI and a custom developed script. Confocal Airyscanned stacks were imported and both the RFP (RFP.Rab8) and YFP (YRab1, 6, 7 or 11) channels were extracted from individual 0.2µm thick optical sections. To isolate puncta, the Subtract Background function of FIJI was used with a rolling-ball radius of 14px (equivalent to 1.2µm diameter). The resulting image was automatically thresholded using the Intermodes threshold to create a binary template of puncta-containing pixels. The Analyze Particles function of FIJI was then used to create regions of interest (ROIs) of all particles larger than 0.05µm^2. All ROIs meeting this threshold were then merged to obtain the final particle mask. This procedure was repeated for each channel individually. A custom script was subsequently used to count the number of RFP particles that overlap with a YFP particle partially (minimum 1% of RFP pixels overlapping) or completely (minimum 90% of RFP pixels overlapping). Overlapping pixels in this sense were those pixels with a pixel value of 1 both in the RFP and the YFP particle masks.

3.6 Computational data analysis

3.6.1 Phenotype recording and processing

Counts of morphological features were recorded in a custom Excel table and then imported into R. All feature counts were divided by each cell's branch count to obtain the per-branch frequency shown in section 4.1.4. Plots were generated using the R package *ggplot* (Wickham, 2016). All comparative statistical analysis for this section was performed using the Estimation Stats online tool (Ho et al., 2018). Most of the feature types by definition can only occur up to once per branch (e.g. Curled Tip, Wavy Lumen), but some can occur multiple times on a single branch. This includes U-turn, Interjunction Curl, Double Lumen, Degenerate Lumen, Disconnect and Cyst. In practice, branches with more than one instance of any of these were very rare across all TCs in this study and therefore had a negligible impact on the results. For simplicity, the descriptions therefore equate "frequency per branch" with "fraction of branches with the feature", even though these two are not strictly the same for features that can occur more than once per branch. Where statistics are reported for the differences between feature frequencies per branch depending on temperature (i.e. to compare the dot plots in Fig. 4.5D-H to each other), the data used for estimation statistics included those cells with zero occurrences of the phenotype, which are omitted in the dot plots. P-values were calculated using a Mann-Whitney U-test.

For all downstream analysis (correlation, principal components, factor analysis, clustering), the original dataset was imported into R. Instead of adjusting feature counts by branch number, a relative size factor *sf* was calculated for each cell *c* by dividing its branch count by the geometric mean of all branch counts in the dataset:

$$sf_c = \frac{branch\ count_c}{\left(\prod_{i=1}^{n_{cells}} branch\ count_i\right)^{\frac{1}{n_{cells}}}}$$

All feature counts were then normalised by dividing by their cell's size factor. This results in the same distribution of data points as simply dividing by branch numbers but at a larger absolute scale (values between 0 and 14 rather than 0 and 1). To equalise the distribution ranges particularly between the control and non-control data points, all normalised counts were then scaled using a generalised logarithmic transformation according to the formula:

$$f(x) = \frac{\operatorname{asinh}(x) - \ln(2)}{\ln(2)}$$

The scaled normalised counts were then used for all downstream analysis. This normalisation procedure was developed with the help of B. Klaus.

3.6.2 Phenomic analysis

The correlation matrix between feature categories shows Pearson correlation coefficients and p-values, and was calculated in R using built-in functions. The plot was generated using the *corrplot* package (Wei and Simko, 2017). Feature pairs showing no number had a p-value < 0.0001. Principal components were calculated using built-in functions and analysed using the *factoextra* package (Kassambara and Mundt, 2017). Factor analysis was performed using the *psych* (Revelle, 2018) and *GPArotation* (Coen and Jennrich, 2005) packages, oblimin rotation and the correlation matrix as the supplied data. Both regression and correlation preserving were tested as methods to find factor scores, both of which yielded ultra-Heywood cases. The consensus method to identify suitable numbers of factors to extract was implemented by the *psycho* package (Makowski, 2018).

The Euclidean distance matrix was calculated and K-means clustering was performed using built-in functions in R. The knee plot and silhouette plot were generated using the *factoextra* package. Hierarchical clustering was computed and plotted using the Morpheus online tool (Gould, 2016) after exporting the scaled normalised dataset from R. Data points were clustered by Euclidean distance with average linkage. This linkage method groups clusters according to the average distance of all points in one cluster to all points in the other, as opposed to single or complete linkage, which compare only the distance of each cluster's closest or most distant point respectively. Multidimensional scaling was calculated in R using the

MASS package (Venables and Ripley, 2002) and plotted using the package *ggpubr* (Kassambara, 2018).

3.7 Genotyping

3.7.1 Primer design

Primers for genotyping were designed using Primer-BLAST provided by the website of the National Center for Biotechnology Information (Ye et al., 2012). The genomic sequence of each *rab* locus was obtained from FlyBase (Gramates et al., 2017) and the 300bp up- and downstream of the start codon were used as a "PCR template" for Primer-BLAST. The optimum melting temperature was set to 60°C and Specificity Checking was set to *Drosophila melanogaster*. Defaults were used for all other parameters. The returned primers were screened according to general design principles, avoiding repeats of more than 3 of any base, preferring primers beginning and ending with G or C, preferring lower self-complementarity, and choosing forward and reverse primers with similar predicted melting temperatures. Primers were synthesised by Sigma-Aldrich.

3.7.1 Squish extraction

DNA for genotyping was extracted using a standard squish extraction protocol. Larvae were collected from the cover slips immediately after imaging and kept at -20°C until further processing. For genoyping, each larva was squished in 35µL squish buffer using a pipette tip. The squish buffer was an aequeous solution containing 10mM Tris, 0.5mM EDTA, and 25mM NaCl, equilibrated to pH 8.2. Before use, 1µL Proteinase K (10mg/mL) was added to 1mL of squish buffer. The squish extract was then incubated at 37°C for 15min to digest protein contents, and subsequently heated to 95°C for 4min to destroy Proteinase K.

3.7.2 Polymerase chain reaction and gel electrophoresis

Genotyping PCRs were carried out in a T100 thermocycler (Bio-Rad) using the KAPA2G Fast Genotyping Kit (KAPA Biosystems). For each reaction, 10µL KAPA2G ready mix was diluted on ice with 7µL dH_2O, and 1µL was added of each 10µM primer solution and the DNA squish extract for a total of 20µL. Samples were spun down and incubated at 95°C for 1min for an intial denaturation. The samples then underwent 32 cycles of denaturation at 95°C for 15s, annealing at 55°C for 10s and extension at 72C° for 15s. After a final extension of 1min at 72°C, the samples were kept at 12°C until gel loading.

Gels were prepared by melting 1% w/v agarose in a standard Tris-Acetate-EDTA (TAE) buffer, pH 8.3. SYBR Safe (Thermo Fisher) was used to stain DNA (5µL per 60mL of gel). Gels were run at 90V for 15-20min and imaged using a UV trans-illumination chamber (PEQLAB) with a top-mounted camera, operated by Quantum-Capt software (Lourmat).

4. Results

4.1 Phenomic analysis of terminal cell phenotypes related to membrane trafficking

The aim of this chapter is to understand how genetic loss-of-function phenotypes manifest in TCs. The concept underlying this analysis is that genes have functions, and different genes can share part of all of each other's functions, for example because they act in the same molecular pathway, because they physically form a complex, or because they otherwise contribute to some common biological mechanism. When this is the case, the respective genes are considered "functionally associated". A common representation of this is a pathway diagram where functionally associated genes are connected by arrows. The logic behind experiments in reverse genetics is that functionally associated genes cause similar loss-of-function phenotypes when mutated. However, previous experiments in the lab and published studies have shown that perturbing genes whose functions are only remotely, if at all, associated can cause similar phenotypes of terminal cell (TC) tube morphology. For example, perturbations of *rab8* (this study)*, rab35* (Schottenfeld-Roames and Ghabrial, 2012), *talin* (Levi et al., 2006) and *btl* (Jarecki et al., 1999; Jones and Metzstein, 2011; Ukken et al., 2014) are all associated with TC phenotypes where the subcellular tube forms bundles. These genes are thus clearly functionally associated with respect to tube morphogenesis. However, the genes function in distinct and unrelated pathways including basal adhesion, chemotactic signalling and membrane trafficking. In this case therefore, a functional association exists despite the lack of a molecular or physical connection between the genes. This means the paradigm of "similar phenotype, similar function" traditionally used in reverse genetics might not resolve functional association to the desired level, i.e. molecular interaction pathways, when applied to TC tube morphology. I therefore sought to identify reliable methods of describing tube phenotypes that make it possible to infer functional associations with known genes ideally at the molecular level for new genes whose function is not known.

For this purpose, I performed a systematic quantitative analysis of wild type and morphologies resulting from RNAi expression. I defined the stereotypical tube morphology, compiled a comprehensive list of non-stereotypical morphological features ("abnormalities"), and recorded the per-branch and per-cell frequencies of all features in cells expressing RNAi against one of four selected genes. The four genes were *rab5*, *syx7*, *talin* and *rab8*. The first three acted as controls for this analysis because their associations are known, and the last was an additional test gene (Fig. 4.1): *rab5* and *syx7* are functionally associated in the form of a physical interaction during early endosome fusion (Morrison et al., 2008; Schottenfeld-Roames et al., 2014). They therefore belong to the same pathway, and should cause a similar loss-of-function or RNAi phenotype. A reliable method of analysing TC tube phenotypes should reflect this similarity in function. *Talin* is involved in adhesion at the basal membrane (Levi et al., 2006) and is not associated with either of the two. Its phenotype should be distinct, and the analysis should reflect this. *Rab8* is the test case, whose possible functional association is to be inferred from the similarity of its loss-of-function phenotype to the other genes'. A satisfactory method of interpreting phenotypes should associate all genes that function in the same molecular pathway with each other. In the case of the genes chosen here, this means that *rab5* should be associated with *syx7*, and *talin* should not be associated with either *rab5* or *syx7*.

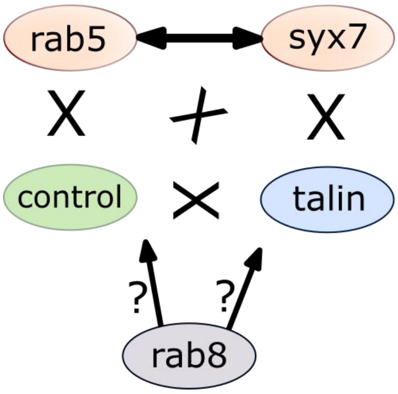

Figure 4.1 Expected associations between control genes
The approach in this study was to use genes whose relationships with each other are known, to test which methods of analysis lead to interpretations that are congruent with existing knowledge. *Rab5* and *syx7* are part of the same endocytic pathway and should therefore be indistinguishable by phenotype. A valid method of interpreting phenotypes should associate them with each other to be consistent with literature. Talin functions in basal adhesion and is therefore not related to either *rab5* or *syx7*. A valid analysis should separate it from *rab5* and *syx7*. Each method of analysis (qualitative, quantitative by invididual features, or phenomic) was tested for its ability to recapitulate this constellation. *Rab8* is the test case of unknown functional association; the *rab8* phenotype is to be used to infer which other genes it is functionally related to.

4.1.1 Qualitative description of wildtype and RNAi phenotypes

The simplest and most traditional method for evaluating phenotypes is categorisation by a human observer into "normal" or "wildtype" and any arbitrary number of "abnormal" classes based on a qualitative assessment. To evalute this method as an analytical approach, this section first provides detailed qualitative descriptions of the phenotypes observed under the different conditions, which may be regarded as an introduction to the range of morphologies exhibited by the subcellular tube network of terminal cells. This also serves as a reference for the sake of completeness. Having characterised the phenotypes in each sample, the following section then describes the experiment used to test whether purely qualitative analysis is suitable for determining which genes act in the same biological pathways.

Controls

The autofluorescence in control TCs (Genotype: *w-;;btl-Gal4,UAS-GFP*) is identical in phenotype to that of a wildtype strain (Oregon-R) and is therefore considered normal (Fig. 4.2A). A "healthy" branch reveals a single straight tube filled by autofluorescent matrix, which is symmetrically distributed around the perimeter of the tube and gradually decreases in diameter towards the branch tip. The lumen encased by the autofluorescent matrix corresponds to the gas-filled interior of the tube. By this description, wildtype TCs often form "unhealthy" branches. Most commonly, the tube does not run straight but instead meanders in wave-like shapes ("wavy lumen"). In some branches, the tube does not end in a blunt, thin tip, but instead runs in a small circle near the branch end ("curled tip"). Similarly, some tubes show one or more 180° turns just after branching off the parent tube ("post-junctional curl"). The morphology of branching points is quite variable. A "healthy" branching point is synchronised between the apical and basal domain, i.e. both the cytoplasm and the tube bifurcate at the same point. Occassionally, the branching point of the tube is shifted and the daughter tubes are parallel to each other until the cytoplasmic branching point is reached ("delayed branching"). There were no noticeable differences on a qualitative level between control cells from 18°C and 29°C cultures (Fig. 4.2B).

rab5-*RNAi*

Expression of the Rab5-IR construct in tracheal cells led to lethality before the third larval stage when driven by *btl*-Gal4, regardless of culture temperature or co-expression with Dicer2. To achieve more restricted expression, it was therefore expressed using the TC-specific driver *dsrf*-Gal4 (Guillemin et al., 2001). At 18°C, the resulting tube phenotype was extremely variable, with some cells showing reduced branching and aberrations in the autofluorescence throughout their tubular network (Fig. 4.2C), while other cells, even within the same individual, were indistinguishable from controls (Fig. 4.2C'). In those cells that were affected, the normally smooth autofluorescence took on a "fuzzy" or "hairy" appearance due to dilations, jitters and small additional tubules enveloping the main tube. Rarely, the autofluorescence was altogether undetectable for short distances, which could be sections where the tube collapsed. There were frequent curl-type defects at tips and after branching points, but also midway along the length of branches. Many branching points were "delayed", with the two daughter tubes running parallel to each other for long distances before finally separating into individual branches. At 29°C, branch numbers were reduced further but the morphology of the autofluorescence was largely similar to the 18°C phenotype (Fig. 4.2D). The main difference was that this phenotype was fully penetrant at 29°C.

syx7-*RNAi*

Like *rab5*-RNAi, animals co-expressing *syx7*-RNAi and Dicer2 yielded no third-instar larvae. Without the Dicer2 construct, viable larvae could be obtained from 18°C cultures but not 29°C. TCs in these animals showed drastic defects. All TCs in these larvae were severely reduced in size and branch number, and their tubes showed quite variable morphologies. Some cells had a single tube per branch, with jittery and sometimes "hairy" autofluorescence similar to *rab5*-RNAi cells (Fig. 4.2E'), while others had bundles of tubes, of which only a small number separated into an individual cytoplasmic branch (Fig. 4.2E). The bundled-up tubes were sometimes discontinuous and created a "hairy" morphology. At branch tips, there was usually only one tube, although this tube was sometimes curl-shaped, or formed a larger knot.

talin-*RNAi*

The RNAi transgene targeting *talin* mRNA recapitulated the phenotype that has been named *tendrils* according to the mutants in which it was discovered (Levi et al., 2006). It is characterised by a severe reduction in the number of branches formed, along with a bundling up of tubes in the remaining cytoplasm. At 18°C, the penetrance of the phenotype was variable, with some cells forming almost no branches and collecting large bundles of many tubes in their soma (Fig. 4.2F'), while others showed very little bundling and grew many branches (Fig. 4.2F). The morphology of the autofluorescence - besides the numerous turns forming bundles - was regular and continuous in larvae reared at 18°C. At 29°C (Fig. 4.2G), the phenotype was more severe as very few cells formed more than three branches. These branches seemed to contain overall less tube material, and the autofluorescence was sometimes discontinuous or abnormally thin.

rab8-*RNAi*

TCs expressing *rab8*-RNAi reached normal sizes and branch numbers at 18°C, and the autofluorescence had a normal morphology (Fig. 4.2H). However, tubes frequently formed curls at branch tips, and the main tube was often enveloped by additional small tubules, resulting in a "hairy" appearance. These were particularly frequent at branching points. Some of these tubules were attached to the main tube, i.e. branched off it, while others were discontinuous. Of those that were attached, some were also gas-filled. At 29°C, TCs appeared reduced in overall size and branch number (Fig. 4.2I). Most noticeably, the additional tubules seen at 18°C were much more numerous and ubiquitous throughout the cell, and tip-curls occurred at almost every branch.

4.1.2 Recognition of phenotypes by a human observer

I first tested whether a qualitative inspection of tube morphology is a reliable method of interpreting TC phenotypes. If this is the case, a human observer should be able to inspect the TCs and identify which RNAi construct was expressed in each case, with one exception. Since *rab5* and *syx7* are functionally associated, their phenotypes should be similar. It should therefore not be possible, or at least be difficult, to identify whether a TC is expressing *rab5*-RNAi or *syx7*-RNAi purely from its phenotype. To test this, I blinded the samples (see Methods) and then recorded a guess for each cell whether it is from a control sample, or if not, which RNAi construct the cell expressed, solely based on the autofluorescence channel of the recorded images. Overall, I correctly identified the RNAi construct (or lack thereof) for the vast majority of cells (Fig. 4.3). All samples were more reliably identified at 29°C, with 100% success rate for *rab5*-RNAi and *talin*-RNAi at 29°C, and *syx7*-RNAi at 18°C. *rab8*-RNAi had the highest misidentification rate, since I failed to identify almost 60% of the cells at 18°C. These were mostly mislabelled as control cells. Vice versa, of those control cells that were misidentified, most were labelled as *rab8*-RNAi at 18°C. Most notably, I was able to reliably distinguish *rab5*-RNAi and *syx7*-RNAi samples by their phenotype. This was primarily due to cell size; *rab5*-RNAi never resulted in as drastic a size reduction as *syx7*-RNAi did. Thus, the recall percentage in this assay primarily reflects penetrance of the phenotypes, highlighting the need for a more robust analytical method that can distinguish penetrance from functional association.

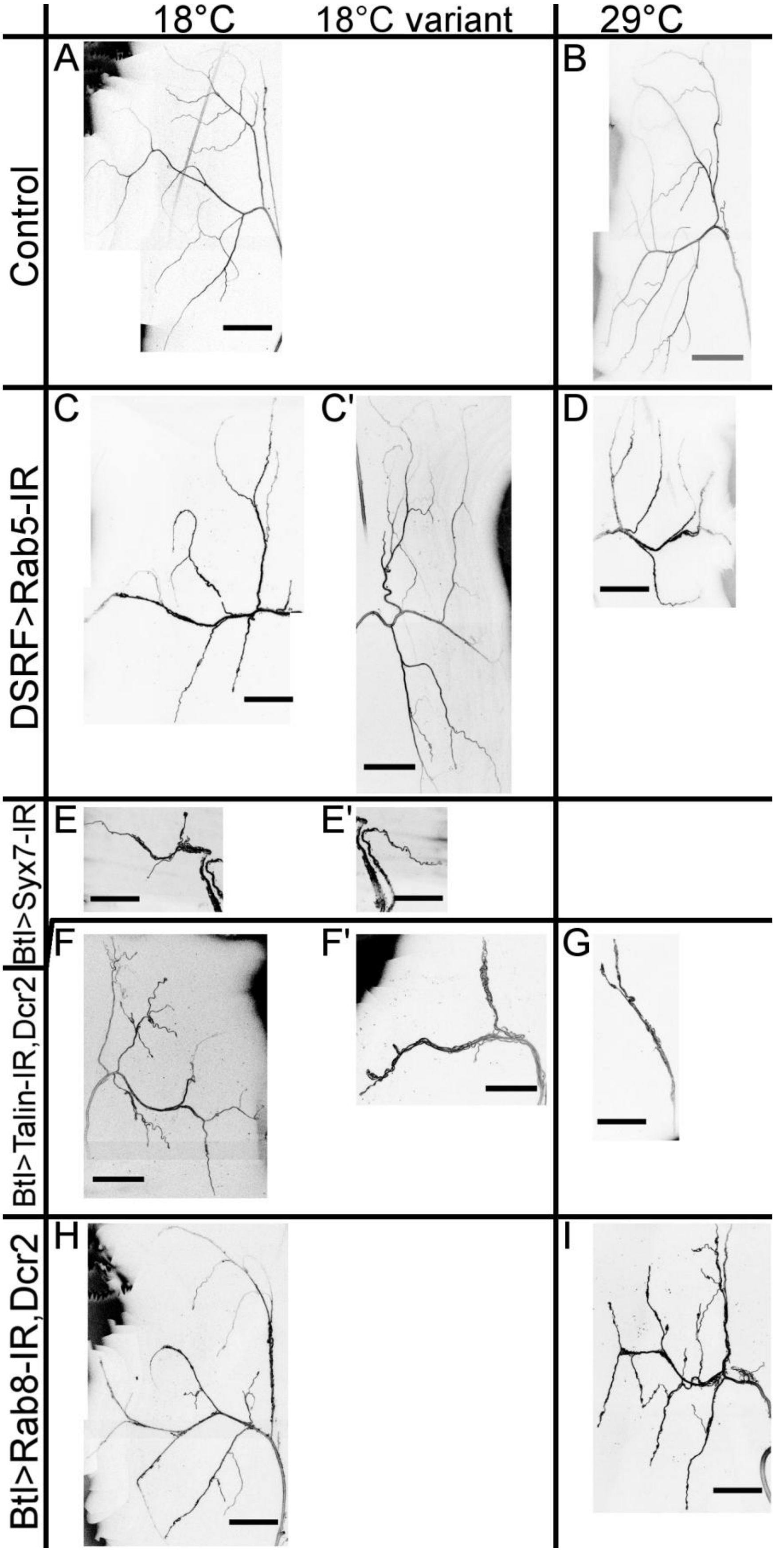
18°C
18°C variant
29°C
Control
A
B
DSRF>Rab5-IR
C
C'
D
Btl>Syx7-IR
E
E'
Btl>Talin-IR,Dcr2
F
F'
G
Btl>Rab8-IR,Dcr2
H
I

Figure 4.2: Representative terminal cells of each sample
Confocal laser scanning micrographs showing autofluorescence of the apical extracellular matrix in TCs illuminated with 405nm wavelength light. Larvae expressing Gal4 under control of either the Btl enhancer (expressed in all tracheal cells) or the SRF enhancer (expressed only in TCs) were raised at two temperature conditions, and heat-fixed and imaged at the wandering third larval stage. GFP was expressed alone in controls, or together with an RNAi construct and Dicer2 in the other samples as labelled. For those samples where variable phenotypes were observed, two representative examples are shown ("18°C variant"). *Syx7*-RNAi was lethal at 29°C. Scale bar, 50µm.

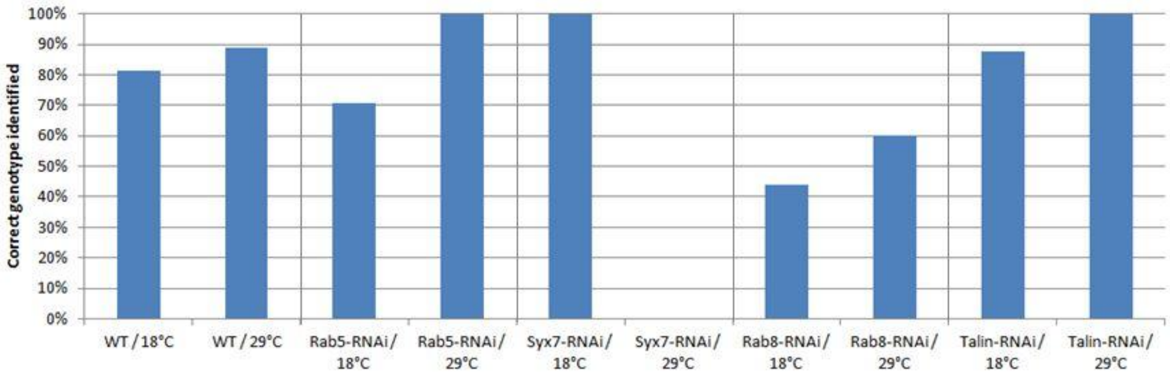

Figure 4.3: Blinded recognition of genotype from autofluorescence
Fraction of cells in each sample whose genotype a human observer was able to recognise by inspecting only the autofluorescence of each cell. Micrographs were stitched and cropped such that each image file contained one TC, and subsequently the files were blinded by replacing their file names with random sequences of letters and numbers. I then recorded a guess for each cell whether it is from a control sample, or if not, which RNAi construct the cell expressed.

4.1.3 Phenotypic feature categories

To describe TC phenotypes in a more systematic and quantitative manner, I screened all recorded cells for morphologies that deviate from the "healthy branch" and "healthy branching point" stereotype, and grouped all identified types of morphology into categories. This resulted in a total of 15 categories of morphological features that can be quantitated for all branches of a TC (Fig. 4.4). Even though many of these are probably genuine defects, they will be referred to as "features" or "feature categories" throughout this work because the occasional occurrence of most feature categories in control cells suggests that not necessarily all of these are consequences of some genetic deficiency. This section defines each feature category and the specific details that distinguish normal morphology from the feature, beginning with features that occur in control cells and loosely ordered by frequency.

- Wavy Lumen: If any stretch of the autofluorescence creates a wave shape instead of a straight line, an occurrence of this feature was counted. The specific definition of this feature presents a "dilemma of the heap" problem. A simple bend should not be interpreted as a special type of morphology, and a sequence of bends could effectively result in a wave shape. To be counted as

Wavy Lumen, bends in the autofluorescence had to be numerous and independent from any bends in the cell soma as visualised by the cytoplasmic fluorophore. They also had to present substantial deviations from a straight line drawn between the start of the "wavy" stretch to its end.

- Wavy Branch: As Wavy Lumen, but pertaining to the branch itself (soma) rather than the tube inside.
- U-turn: At a point where the soma branches, the tube does not have a branching point but instead traces up one branch, then makes a U-turn, returns to the branching point and follows the other cytoplasmic branch.
- Curled Tip: A morphological deviation from a blunt, straight end at the tip of an autofluorescent tube branch. To be considered a Curled Tip, the tube needs to make at least one turn greater than 90°.
- Post-junctional Curl (PJ-Curl): Several bends immediately after a branching point, after which the tube continues to grow at an approximate 80-100° angle from the parent tube. At least two sequential bends are required to qualify.
- Inter-junctional Curl (IJ-Curl): Knots anywhere along a tube other than after the branching point or at the tip. A single loop in the tube is sufficient to qualify.
- Double Lumen: An additional tube branched off the main tube that at no point separates into a cytoplasmic branch.
- Degenerate Lumen: As Double Lumen, but the additional tube is not connected to the main tube.
- Delayed Branching: A desynchronisation between the cytoplasmic branching point and the tube branching point, resulting in the two daughter tubes running parallel to each other for at least several micrometres before splitting into separate cytoplasmic branches.
- Disconnect: An interruption in the autofluorescence, resulting in stretches that are not connected to the main tubular network.
- Cyst: A localised dilation of the autofluorescence.
- Hairy Branch: Numerous additional, usually short and thin, tubules surrounding the main tube, resulting in a "hairy" appearance. These may be continuous and connected to the tube or not.
- Disrupted Tip: The usually very short distance between tube and branch tip is increased to several micrometres. Autofluorescent fragments are found in between.
- Hairy Junction: As "Hairy Branch", but occurring at a branching point. The additional tubules usually fill up the space between the daughter tubes instead of wrapping around them.
- Triple Junction: A branching point where the cell body splits into three instead of two daughter branches. The tube does not necessarily have to split into three at the same point.

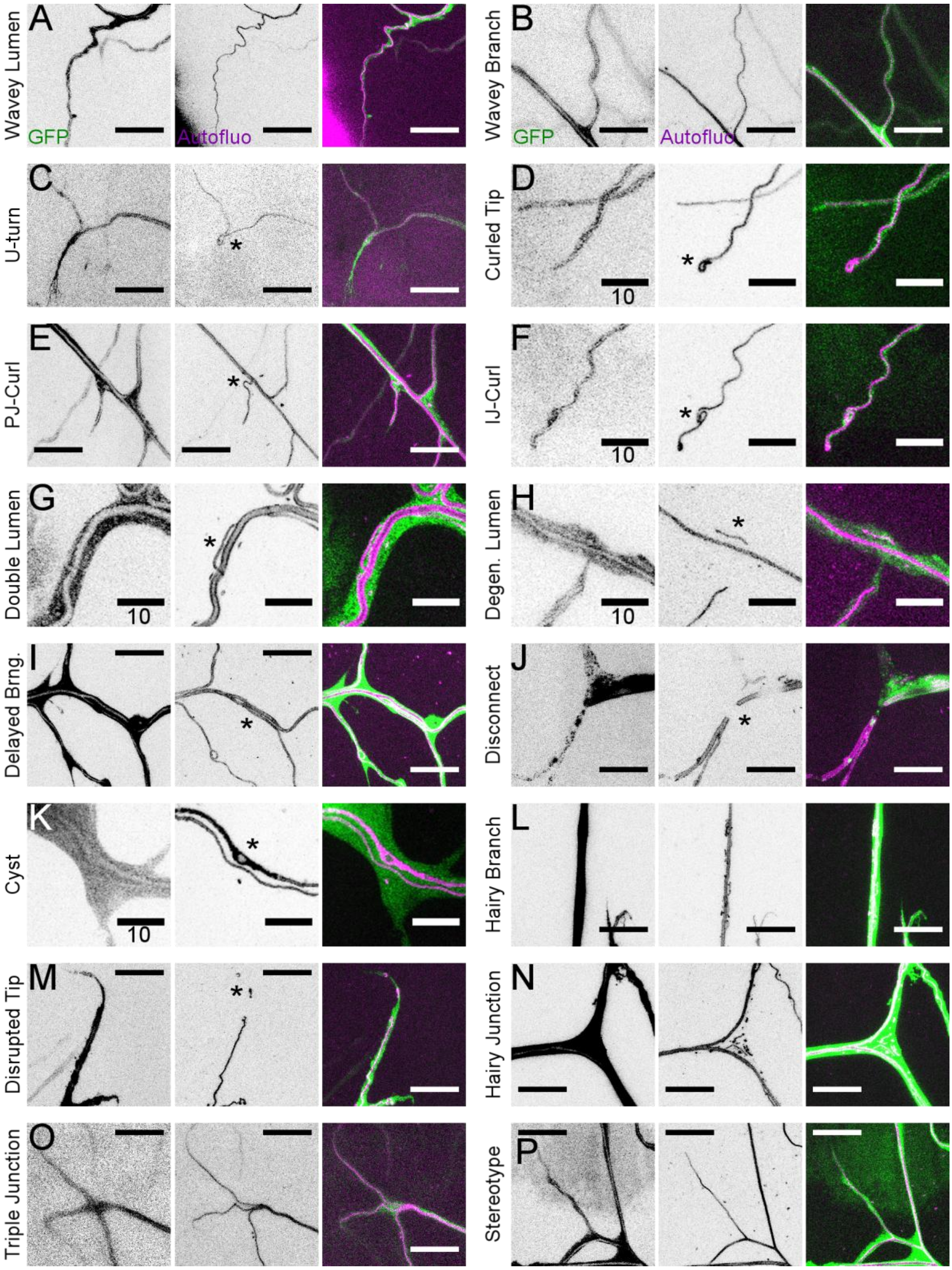

Figure 4.4: Examples of morphological feature categories
Cropped confocal fluorescence micrographs obtained as in Fig. 4.3. For each example, the GFP channel, the 405nm autofluorescence (apical extracellular matrix) and a merged image of both is shown. (P) Example of a "healthy" branch with stereotypical morphology. See appendix for genotypes. Asterisks highlight the respective feature. Scale bar, 20µm; for those labelled as "10", the scale bar represents 10µm.

4.1.4 Quantitative description and impact of culture temperature

The micrographs were stitched and separated such that each image file contained one TC. The files were then blinded for manual phenotype scoring (see Methods). In addition to counting the number of occurrences of each feature category listed in section 4.1.3, I recorded the total number of branches, i.e. the number of autofluorescent branch tips for each cell (Fig. 4.5A). Previous work in the lab has shown that branch number is a reliable readout for cell size (Sigurbjornsdottir, 2015), and has been used in the past as a phenotype of interest (Best, 2018; Jones et al., 2014; Levi et al., 2006). The number of branches also limits the possible number of tube-related phenotypes, and therefore needs to be adjusted for. I additionally recorded the number of "healthy" branches as an unspecific reflection of phenotype penetrance. For this purpose, any branch showing at least one of the features defined above counts as an "unhealthy" branch. Or vice versa, any branch whose morphology conforms to the stereotypical morphology is considered "healthy". The fraction of branches that were healthy in this sense will be referred to as the "healthy fraction". When analysing differences between samples, I report estimation statistics, which includes the mean, difference/delta and the 95% confidence interval [CI] of bootstrapped means (Ho et al., 2018). This is to convey the impact that a factor has on the variable of interest, rather than reducing it to a dichotomy of "effect or no effect". For some feature types, the frequency per branch (Fig. 4.5D-H) is not strictly identical to the fraction of branches that manifest the feature (because conceptually, they can occur more than once per branch), but in practice the difference is marginal and the two can be considered interchangeable (see Methods section 3.6.1). The following descriptive sections summarise the dataset obtained by this method of assessing TC phenotype and are provided primarily as a reference for detailed values that could not be represented graphically in Fig.4.5 in a practicable way.

I first observed whether any of the individual aspects of phenotype that were quantified here would be sufficient to recall the expected relationships between the test genes. This would be the case for any quantified variable (branch count, healthy fraction, and the 15 feature categories) whose distribution in control TCs is different from either *rab5*- and *syx7*-RNAi but not *talin*-RNAi, or from *talin*-RNAi but not *rab5*- and *syx7*-RNAi. Neither branch number nor healthy fraction satisfied these criteria. Out of the 15 features, 11 were found at least once in control TCs, suggesting that their appearance per se in a TC does not constitute a morphological defect. Out of these 11, five were sufficient to distinguish control cells from RNAi-expressing cells, but not to distinguish the different RNAi constructs from each other (Wavy Lumen, Curled Tip, Interjunction Curl, Postjunction Curl and Delayed Branching). Another five features were generally infrequent and did not show any clear pattern (Wavy Branch, U-turn, Double Lumen, Degenerate Lumen, and Triple Junction). The last of the 11 features, Disrupted Tip, was found once in one control TC. The remaining four categories were specific to the RNAi samples: Disconnect, Cyst, Hairy Branch and Hairy Junction. These four, and Disrupted Tip, were all found in TCs expressing *rab5*-RNAi and *syx7*-RNAi, but not in TCs expressing *talin*-RNAi. All of these also appeared with different frequencies in TCs expressing *rab8*-RNAi. These features are therefore likely to be related specifically to the shared aspects of the functions of *rab5* and *syx7*. However, the lack of features specifically related to *talin* means that a more generally applicable analytical method will be needed to study genes not included in this test set.

Control

Control TCs had on average 17.1 branches at 18°C and 21.7 branches at 29°C (Fig. 4.5A). The mean difference was 4.6 branches (95% CI: 1.2 to 7.6; p=0.0016; Fig. 4.5C), indicating an increase of TC growth at the higher temperature condition. I could not exclude that this might be caused by circumstances other than temperature, such as a lower oxygen concentration in the 29°C incubator (Jarecki et al., 1999). In the vast majority of control TCs, 70% of branches or more were healthy (Fig. 4.5B). The average fraction of healthy branches was 66% at 18°C compared to 76% at 29°C (delta: 0.10; 95% CI: 0.03 to 0.17; p=0.007; Fig. 4.5C), indicating that the 29°C environment not only increases the growth of TCs but also improves their ability to form healthy branches. The most common feature found in controls was Wavy Lumen, followed by Wavy Branch, Postjunction Curl and Curled Tip. The penetrance of Wavy Lumen per cell, i.e. the fraction of cells with at least one instance of Wavy Lumen on any branch, was 87% at 18°C and 60% at 29°C (Fig.4.5D'). Wavy Branches occurred in 65% of cells at 18°C and 40% at 29°C. In those cells that had any, the 29°C samples had a slightly lower penetrance per branch, i.e. frequency, of both types of feature (Fig. 4.5D'; Wavy Lumen: 0.15 per branch at 18°C vs. 0.10 at 29°C; delta: -0.06; 95% CI: -0.11 to 0.00; p=0.008. Wavy Branch: 0.09 per branch at 18°C vs. 0.04 at 29°C; delta: -0.05; 95% CI: -0.08 to -0.01; p=0.005). This provides additional information regarding the temperature as a possible cause of the differences between the two control samples. Hypoxia-induced branching increases are associated with a "tortuous" tube morphology (Jarecki et al., 1999), which resembles the Wavy Lumen and Wavy Branch features according to the definitions used here. The lower frequency of both features in cultures from the 29°C incubator environment therefore suggests that these larvae did not grow in a hypoxic environment. The three curl-type features (Tip, PJ and IJ) are found in 25-50% of cells and usually affect less than 15% of their branches. Curled Tip, Interjunction Curl and Triple Junction showed a trend towards slightly lower penetrance both per cell and per branch at 29°C compared to 18°C. The other features commonly found in control cells are Degenerate Lumen, Delayed Branching and U-turns. These three, as well as Postjunctional Curl, appeared in marginally more cells at 29°C but an impact of temperature on their frequencies per branch could not be determined with confidence. Considering their overall low frequencies, the effect of the 29°C condition on the proportion of healthy branches can be attributed primarily to the reduction in Wavy Lumens and Wavy Branches. Double Lumens or a morphology that qualified as a Disrupted Tip appeared once each in 77 cells with a total of 1500 branches. Overall, only four of the 15 feature categories were never found in control cells, suggesting that these are exclusively consequences of genetic defects: Disconnect, Cyst, Hairy Branch and Hairy Junction.

rab5-*RNAi*

TCs expressing *rab5*-RNAi showed a very different picture from controls. The number of branches and fraction of healthy branches reflected the variable penetrance seen when assessing phenotypes qualitatively. At 18°C, many cells reached branch numbers similar to controls but others had drastically reduced branch numbers as low as 3 (Fig. 4.5A). Similarly, some cells had more than 70% healthy branches while most others were below 25% (Fig. 4.5B). At 29°C, all cells had branch numbers similar to the more severely affected cells of the 18°C sample, with an average of 9.0 branches and very few healthy branches. This is a reduction in mean branch number of -5.8 from 14.8 at 18°C (Fig. 4.5C; 95% CI: -11.18 to -0.82; p=0.06). The fraction of healthy branches is reduced from 26.1% on average at 18°C to 6.1% at 29°C (delta: -19.9%; 95% CI: -35.6% to -5.8%; p=0.03). The cytoplasmic fluorophore was barely detectable in many *rab5*-RNAi cells, and in most others did not smoothly outline the cytoplasm but instead formed large aggregates. As a result, the shape of the cell itself could not be reliably traced for *rab5*-RNAi, and the feature Wavy Branch could not be assessed. All other feature categories were found in at least one temperature condition. The most common features were Wavy Lumen, Curled Tip and Hairy Branch, all of which were found in almost all TCs of either temperature (Fig, 4.5E'). The frequencies per branch of all three features varied from 0 to 1 per branch (Fig, 4.5E). Although abundant, Wavy Lumen was not affected by temperature (delta: 0.08; 95% CI: -0.09 to 0.23; p=0.2), suggesting that the penetrance observed here represents saturation, and showing that *rab5*-RNAi suppresses the beneficial effect of the higher temperature environment. Curled Tip and Hairy Branch both appeared more often at 29°C (Curled Tip: 0.28 per branch at 18°C vs. 0.45 at 29°C; delta: 0.17; 95% CI: 0.01 to 0.35; p=0.08. Hairy Branch: 0.35 at 18°C vs. 0.55 at 29°C; delta: 0.21; 95% CI: -0.00 to 0.42; p=0.06). The strongest impact of temperature was seen in the Disrupted Tip feature, which was very rare at 18°C (11.8% of cells, 0.03 per branch) but common at 29°C (70.6% of cells, 0.24 per branch; delta: 0.21; 95% CI: 0.10 to 0.31; p=0.0008). Hairy Junction, Delayed Branching, Postjunction Curl and Interjunction Curl all occurred with moderate penetrance but showed no consistent trends dependent on temperature. U-turn, Cyst, Triple Junction and Disconnect were found rarely. The latter two were slightly more frequent at 29°C, but the absolute counts were too small to interpret.

syx7-*RNAi*

TCs in this sample had drastically reduced branch numbers, reaching at most 5 branches (Fig. 4.5A). Usually, all branches showed phenotypic features. Only three cells were found (out of 14) that had any healthy branch at all (exactly one in each case) (Fig. 4.5B). The most common features were Wavy Lumen, Curled Tip, Delayed Branching, Hairy Branch and Disrupted Tip, all of which occurred with similar penetrance per cell (57 to 64%) and per branch (0.29 to 0.48; p=0.6 to 0.9 relative to Wavy Lumen). All other features were observed rarely; 0 to 3 times across all cells in this sample.

talin-*RNAi*

TCs expressing *talin*-RNAi had severely reduced branch counts (Fig. 4.5A) and rarely more than one healthy branch (Fig. 4.5B). Both the branch counts and fractions of healthy branches were similar at 18°C and 29°C. The 29°C sample merely had a slightly reduced spread around the mean of 8.4 branches (Fig.4.5A; vs. 8.9 at 18°C; p=0.95; Fig. 4.5C) and a larger fraction of cells had zero healthy branches (75% vs. 50% at 18°C; Fig.4.4B). The feature counts were dominated by Wavy Lumen, Curled

Tip and Delayed Branching, all of which were found in almost all *talin*-RNAi TCs (Fig. 4.5G'). These three feature categories are precisely those that best reflect the qualitative description of the phenotype associated with mutant alleles of *talin*. Their frequencies per branch spread from 0 to 1 (Fig. 4.5G). Curled Tip was almost absolutely saturated (appearing in every cell and almost every branch) but still showed an increase depending on temperature (0.71 per branch at 18°C vs. 0.85 at 29°C; delta: 0.14; 95% CI: 0.02 to 0.27; p=0.05). Wavy Lumen and Delayed Branching were unaffected by temperature, suggesting that the expression of the RNAi construct at 18°C already nearly eliminated the entire *talin* gene product. Cyst was the only feature that never occurred in this genotype. Postjunction and Interjunction Curls were found in less than 50% of cells and usually affected less than 25% of branches. The slight differences in their penetrances per cell represent too small absolute numbers of cells to be meaningful, and their frequencies per branch were similar at both temperature conditions (p=0.4 and p=0.3 respectively). All other features were very rare.

rab8-*RNAi*

Out of the different RNAi constructs tested, the impact of *rab8*-RNAi on TC morphology differed the most by culture temperature. At 18°C, branch numbers were normal (mean 21.7; Fig. 4.5A), as opposed to the reduced numbers seen at 29°C (mean 15.2; delta: -6.5; 95% CI: -11.5 to -2.0; p=0.02; Fig. 4.5C). The fraction of healthy branches, usually below 25% at 18°C, dropped well below 10% at 29°C (means: 0.254 vs. 0.004; delta: -0.21; 95% CI: -0.32 to -0.12; p=0.001; Fig. 4.5B). Seven of the 15 feature categories had nearly 100% penetrance per cell (Fig.4.5H'), although penetrances per branch of >50% were only observed in few cases (Fig.4.5H). Among these seven, Curled Tip and Delayed Branching had no difference between the two temperatures in their frequencies per branch (p=0.9 and p=0.8 respectively), suggesting that these frequencies represent saturation. Similarly, Wavy Lumen and Postjunction Curl showed a trend towards higher frequencies at 29°C, but the effect, if any, is likely to be very small (Wavy Lumen: delta: 0.09; 95% CI: -0.05 to 0.3; PJ Curl: delta: 0.04; 95% CI: -0.04 to 0.15). The culture temperature had the strongest effect on Interjunction Curl (0.16 per branch at 18°C vs. 0.4 at 29°C; delta: 0.24; 95% CI: 0.14 to 0.34; p=0.001), Hairy Branch (0.10 vs. 0.20; delta: 0.10; 95% CI: 0.03 to 0.18; p=0.02) and Hairy Junction (0.08 vs. 0.28; delta: 0.20; 95% CI: 0.11 to 0.33; p=0.0004). Disrupted Tips occurred at similar frequencies at both temperatures (p=0.11), but the penetrance per cell increased from 25% at 18°C to 67% at 29°C (Fig. 4.5H'). The remaining feature types were rare, seldomly appearing more than once per cell. U-turns were not observed in *rab8*-RNAi.

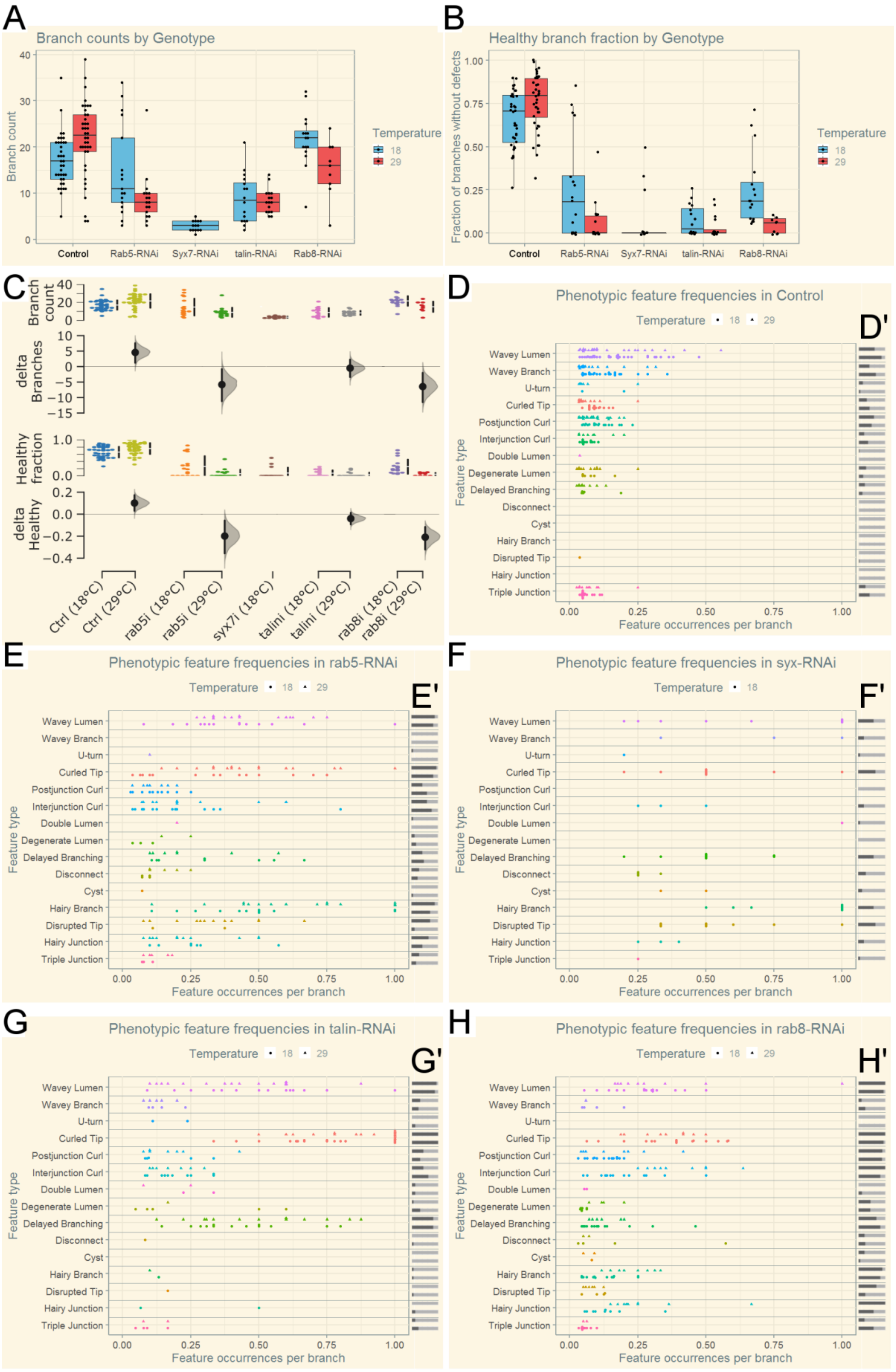
A
Branch counts by Genotype
Branch count
Temperature
18
29
Control
Rab5-RNAi
Syx7-RNAi
talin-RNAi
Rab8-RNAi
B
Healthy branch fraction by Genotype
Fraction of branches without defects
C
Branch count
delta Branches
Healthy fraction
delta Healthy
Ctrl (18°C)
Ctrl (29°C)
rab5i (18°C)
rab5i (29°C)
syx7i (18°C)
talini (18°C)
talini (29°C)
rab8i (18°C)
rab8i (29°C)
D
Phenotypic feature frequencies in Control
D'
E
Phenotypic feature frequencies in rab5-RNAi
E'
F
Phenotypic feature frequencies in syx-RNAi
F'
G
Phenotypic feature frequencies in talin-RNAi
G'
H
Phenotypic feature frequencies in rab8-RNAi
H'
Feature type
Wavey Lumen
Wavey Branch
U-turn
Curled Tip
Postjunction Curl
Interjunction Curl
Double Lumen
Degenerate Lumen
Delayed Branching
Disconnect
Cyst
Hairy Branch
Disrupted Tip
Hairy Junction
Triple Junction
Feature occurrences per branch
0.00
0.25
0.50
0.75
1.00

Figure 4.5: Quantification of TC phenotypes

Three aspects of TC morphology were scored for each cell. (A) Number of branches, which is identical to the number of branch tips. (B) Fraction of "healthy" branches, i.e. which had none of the fifteen non-stereotypical features defined in section 4.1.3. (C) Estimation statistics quantifying the impact of culture temperature on branch number and healthy fraction. The dot plots here are identical to the ones from (A) and (B) respectively. Each effect size estimation graph illustrates the potential range of the mean difference between the 18°C and 29°C samples, calculated by bootstrapping (large dot: mean difference/delta, black bars: 95% confidence interval, grey plot: distribution of bootstrapped mean deltas). P-values are not illustrated in order to avoid the known pitfalls (Ho et al., 2018). They are reported in the main text for completeness. (D-H) Frequency of each feature category per branch. Each dot represents the frequency of that feature found in one cell. Cells from 29°C are plotted as triangles, and those from 18°C as circles underneath. Note that in some samples, such as *syx7*-RNAi, branch numbers are so low that a feature occurring once in a cell can result in a frequency of 0.5 or 0.33 per branch. Dots from cells with 0 occurrences are omitted for better clarity. (D'-H') Frequency of each feature per cell. The dark portion of the bar represents the fraction of cells which had at least one occurrence of the feature. Except for *syx7*-RNAi, each feature type has two bar plots, one per temperature condition, with the upper being for 29°C. Number of cells scored: Ctrl/18°C: 37, Ctrl/29°C: 40, *rab5*-RNAi/18°C: 17, *rab5*-RNAi /29°C: 17, *syx7*-RNAi: 14, *talin*-RNAi/18°C: 16, *talin*-RNAi/29°C: 16, *rab8*-RNAi/18°C: 16, *rab8*-RNAi /29°C: 9

4.1.5 Correlation and principal component analysis

Analogous to the categorisation of phenotypes into "normal" and "abnormal" classes by an observer for qualitative assessment, the aim of a quantitative phenomic assessment is to identify groups of cells which are distinguishable by their phenotypic profiles, taking into account all feature categories rather than a single one. If the procedure for describing TC phenotypes developed here is adequate, a computational clustering algorithm should be able to detect biologically meaningful categories of cells. To optimise the detection of groups of similar cells, I first ensured that there are no redundant dimensions in the dataset, whereby each frequency of one feature category is one dimension. Redundant dimensions are those which contain the same information, because they are correlated. Their presence can bias clustering algorithms and potentially obscure the discovery of clusters (Toloşi and Lengauer, 2011). In addition, features that consistently correlate with another could be eliminated in future assessments, thereby making the time-consuming process of quantitation quicker.

To identify potentially redundant dimensions, I first performed a correlation analysis. For this purpose, all samples are pooled because such correlations between variables would be consistent across all genotypes and conditions. There are very few feature types whose occurrence correlated with any other (Fig.4.6A). As indicated by the blue ellipses in Fig 4.6A, some features correlated significantly ($p<0.0001$) with others, but the correlations were very weak ($-0.3 < r < 0.4$). The strongest correlation was observed between Delayed Branching and Curled Tip ($r=0.57$), followed by Disrupted Tip / Hairy Branch ($r=0.56$) and Hairy Junction / Hairy Branch ($r=0.5$; $p<0.0001$ for all three). These relationships probably derive from the frequencies of these feature pairs in *talin*-RNAi and *rab5*-RNAi respectively. Yet, even for these the correlation coefficients are so low that it is unlikely they contain redundant information.

To determine the degree to which the present correlations could influence clustering algorithms, I performed a principal component analysis (PCA). The aim of this method is to reduce the number of variables to be analysed effectively by collapsing correlated variables into principal components. In datasets where variables are redundant, the first handful of principal components account for nearly all of the variance (i.e. information) in the dataset and can therefore be used to analyse it instead of the original dimensions. If this method of analysis performs well, it is usually preferable to then identify clusters of cells using the principal components as variables rather than the original variables (i.e. feature frequencies).

The first and second principal component for this dataset only explain 20.4% and 11.4% of the variances in the dataset (Fig. 4.6B), indicating very low correlation between the original variables, as expected from the correlation analysis. Correspondingly, the correlations of the first two principal components with each variable (Fig.4.6C) only partially recapitulate the pairwise correlations between the variables (Fig.4.6A). For example, Curled Tip, Hairy Branch and Interjunction Curl correlate with each other to similar degrees (Fig. 4.6A), but Hairy Branch correlates both with the first and second principal component, while Curled Tip and Interjunction Curl only correlate with the second, but not the first principal component (Fig. 4.6C). In usual procedure, one would retain all successive principal components until the remaining components account for insubstantial fractions of variances. These remaining ones would then be discarded. Graphically, this would be reflected in a sudden drop in a scree plot (Fig. 4.6B). In this dataset, the successive principal components all account for linearly declining fractions of variances in the original variables. This shows that the first two components only reflect a small fraction of the information contained in the original dataset, and there is no basis to determine an appropriate number of subsequent components to include. This means that a cluster analysis is likely to yield better results and be more informative using the original variables rather than principal components. It also indicates that each feature contains unique information and a TC's phenotype can thus only be captured comprehensively when all are quantitated.

However, the correlation of variables with the first two principal components (Fig. 4.6C) suggests that there are at least two distinct categories of variables. The first group of features contains Disrupted Tip, Hairy Branch, Hairy Junction and Disconnect, while the second contains Wavy Lumen, Interjunction Curl, Curled Tip, Delayed Branching, and potentially Cyst and Double Lumen. The cause for this grouping could be that the feature categories in each group are influenced by a shared underlying mechanism. Such "hidden", but unmeasured (or unmeasurable) factors are also known as latent variables, and exploratory factor analysis (EFA) can be used to estimate the influence of such variables in a dataset. EFA requires that the subject of study is understood to a degree that allows making hypotheses about the nature of latent variables. In TCs, we could reasonably expect that the "hairy" feature types and the "curl" types could reflect common underlying mechanisms. An important question to answer for EFA is the number of factors the data should be fitted to. There are several methods for this, but no consensus about which is the best to use depending on the type of data. I therefore used a method agreement procedure to determine the number of factors recommended using each available method (Makowski, 2018). This yielded no consensus, as two methods each suggested 1, 4, 6 and 7 factors. Attempting EFA with any of these numbers caused ultra-Heywood cases, i.e. instances where the fitted model would be estimated to account for more than 100% of the variance of a variable. This indicates that the data violates the common factor model and therefore does not provide a basis for identifying latent variables. The aim of EFA is to determine "the number and nature of common factors needed to account for the pattern of correlations among the measured variables" (Norris and Lecavalier, 2010). The failure of EFA thus suggests that none of the different phenotype categories are connected by underlying causal factors. The two different groups of features distinguishable by PCA are consequently unlikely to reflect a connection of interest in this analysis.

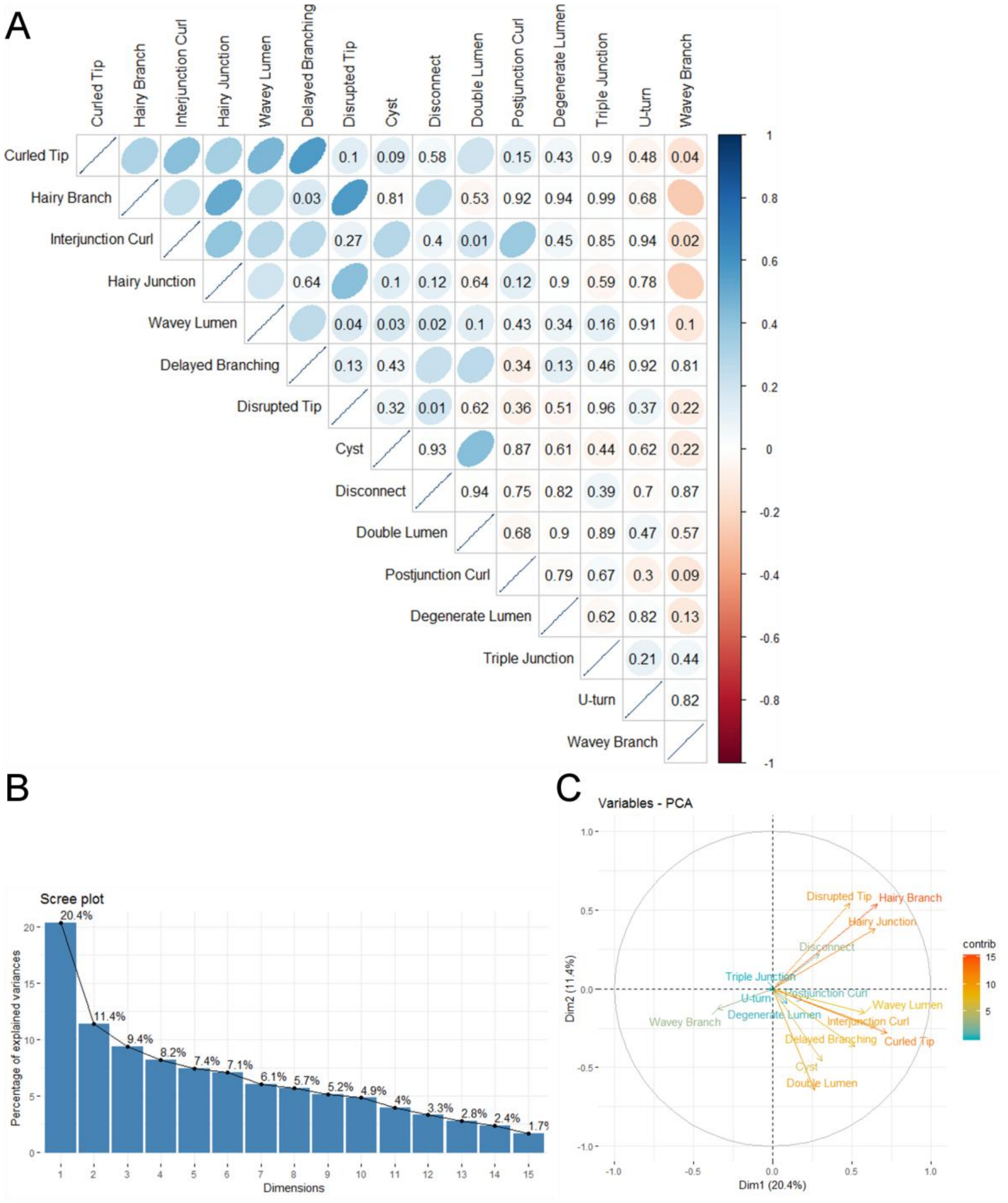

Figure 4.6: Analysis of correlation between feature categories

(A) Correlation matrix illustrating the Pearson correlation coefficient *r* between each pair of feature categories both by colour and shape of the ellipses, where a narrower ellipse represents stronger correlation. The p-value is given for those pairs whose p-value was larger than 0.0001. (B) Scree plot of dimensions calculated by principal component analysis, showing fractions of the original dataset's variances explained by each principal component. (C) Correlation of each feature category with the first (x) and second (y) principal component. Colour shading indicates the contribution to the first principal component (weighting percentage). Vectors with similar orientations indicate variables with similar relationships to the first two principal components. The discrepancies between these correlations and the pairwise correlations in (A) reflect the low percentage of variances explained by the first two principal components.

4.1.6 Phenomic cluster analysis

The aim of this analysis was to test whether the frequency of phenotypic features in the TC lumenal autofluorescence is a reliable readout of phenotype. If this was the case, the resulting feature counts should allow categorising cells according to the genetic function lost. Specifically, the analysis should categorise cells expressing *rab5*-RNAi together with those expressing *syx7*-RNAi (because the Rab5 and Syx7 proteins should interact physically and functionally), and it should distinguish both from TCs expressing *talin*-RNAi (an unrelated gene) and control cells. Computational clustering algorithms provide a systematic approach to categorising multidimensional data as produced by counting occurrences of 15 different phenotypic features. To test whether TCs can be grouped using this data, I compared the groupings produced by two different clustering algorithms. The K-means algorithm is an unsupervised machine learning method whereby a defined number (K) of seeds are randomly positioned within the sample space and data points (cells) are allocated to the seed closest to them by Euclidean distance. The second is a hierarchical clustering algorithm that recursively pairs data points with their closest neighbour until all points have been merged. This results in a tree of pairings within which distinct groups or clusters can be identified using a fixed distance cutoff or relative distances to other groups. The distance metric in hierarchical clustering can be Euclidean distance or other dissimilarity estimators such as Pearson correlation (or other correlation measures), or cosine similarity. One important difference between the two clustering algorithms is that K-means must assign all data points to a cluster, whereas hierarchical clustering allows individual data points to remain solitary when the tree is subdivided into clusters. Depending on the use, this constraint of K-means may be desired, though if some data points do not fit well into any group (outliers), it can cause misleading associations due to coercion into the closest cluster. Having identified the expected clusters, I used multidimensional scaling (MDS) to visualise the dataset as a two-dimensional map where the clusters can be inspected cell-by-cell. MDS as a dimensionality reduction method is related to PCA, but is more flexible in the measure of dissimilarity between data points that can be used. This makes it more suited to approximating the original dataset visually even when PCA cannot identify informative principal components to plot for the same purpose.

K-means clustering

K-means uses Euclidean distance to compare data points. A map of pairwise Euclidean distance for all TCs thus provides an intuitive insight into clusters that the algorithm might return (Fig. 4.7A). To identify clusters in this matrix using the K-means algorithm, the key factor that must be predetermined is the number of clusters, K. Identifying a meaningful K is the decisive step of discovery using this algorithm, since it answers the question of how many groups exist within the dataset. This is achieved by running the algorithm with a range of values for K and then testing the goodness of clustering in each run. Two methods are commonly used for this purpose. The "knee" method uses the sum of squared distances, which measures the dispersion of data points around their cluster's centre, and the silhouette method is based on the eponymous silhouette score, a measure of distance between clusters.

The "knee" plot results in a bow-shaped graph, which shows a kink ("knee") if a value for K produces a particularly low within-sum-of-squares, i.e. clusters with less dispersed data points. For the TC dataset, the plot produces two knees for K=2 and K=4 (Fig. 4.7B), indicating that these values produce less dispersed clustering than others. The silhouette method shows high average silhouette widths for K=2 and K=4 (Fig. 4.7C), indicating that these values produce clusters further apart from each other than other K values. Therefore, I decided to further inspect clusterings for K values ranging from 2 to 5, to include both the two good candidates (2 and 4) and two controls (3 and 5). All four produced one cluster containing all control cells (except for one cell in K=3) as well as a small number of cells from other samples that had low frequencies of phenotypic features (Fig. 4.7D). For example, the six *rab5*-RNAi/18°C cells grouped together with controls are the same aforementioned cells whose branch numbers were as controls and which did not show the phenotypic features present in other *rab5*-RNAi cells. For K=2, it thus seems that the two clusters distinguish normal from abnormal phenotypes.

At K=3, the remaining cells are split into one cluster containing all *talin*-RNAi cells, and a second cluster containing the remaining *rab5*-RNAi cells and most *rab8*-RNAi cells (Fig. 4.7D). *Syx7*-RNAi cells are roughly equally distributed across the three clusters. Given the separation of *talin*-RNAi and *rab5*-/*rab8*-RNAi cells, this could roughly reflect a grouping into control, "basal adhesion defective" and "membrane trafficking defective" cells. At K=4, the *rab5*-/*rab8*-RNAi group is further split into one cluster containing *rab5*-RNAi and *syx7*-RNAi cells, and another containing *rab8*-RNAi and the remaining *rab5*-RNAi cells. This categorisation comes very close to the outcome expected if the analysis reproduces known associations. It distinguishes controls from *talin*-RNAi, and both in turn from a combined *rab5*-/*syx7*-RNAi group. The final *rab5*-/*rab8*-RNAi cluster could therefore suggest a functional association between *rab5* and *rab8*. Lastly, K=5 produces the same three non-control clusters, but splits the control cluster into two roughly identical clusters. This split therefore, as predicted, does not provide any additional information and indicates that the data does not support the presence of more than 4 categories of phenotypically different cells in the dataset.

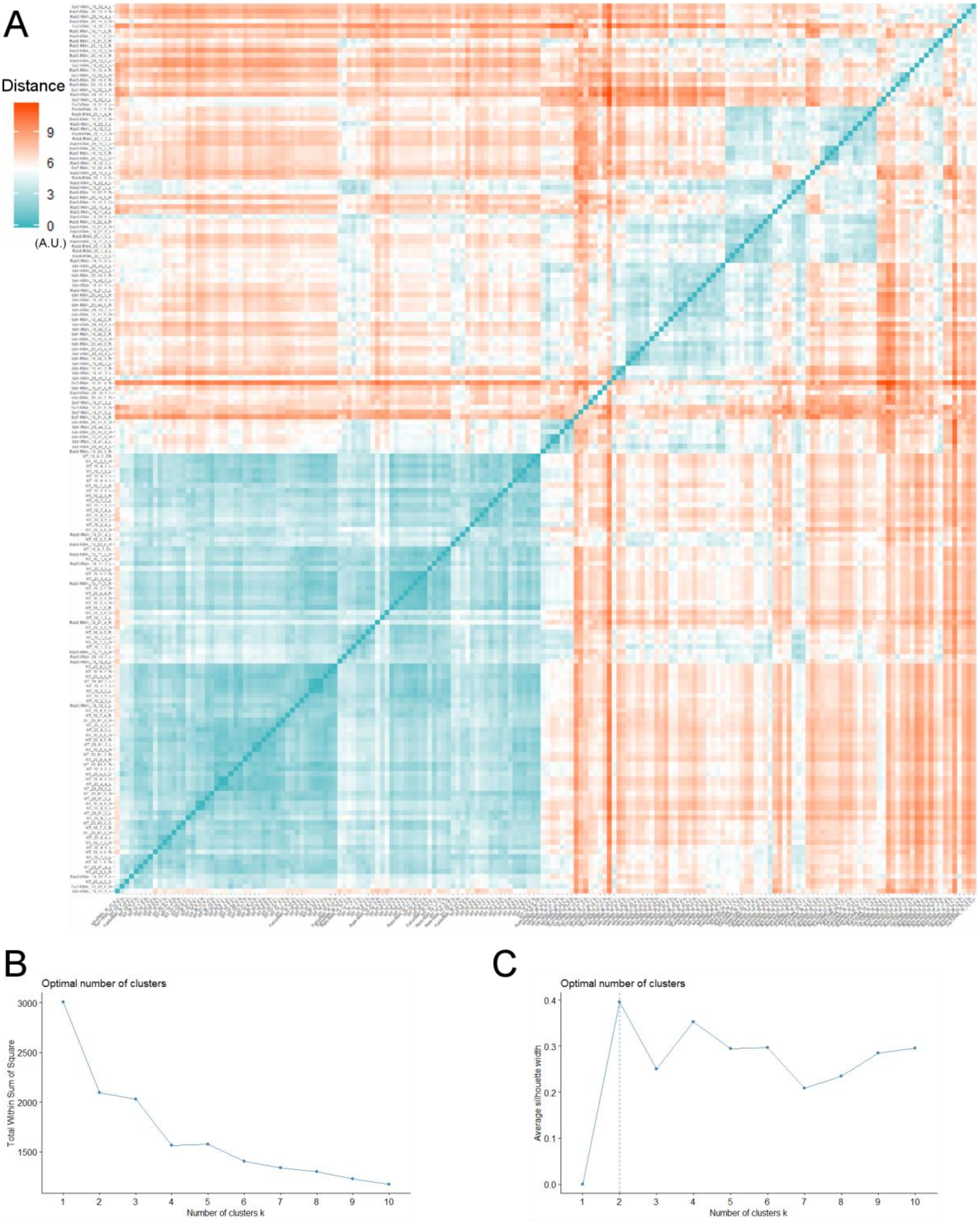

D

Kmeans

K=2

		Cluster 2	Cluster 1
Control	18°C	37	
	29°C	40	
rab5-RNAi	18°C	6	11
	29°C	1	16
syx7-RNAi	18°C	5	9
talin-RNAi	18°C		16
	29°C		16
rab8-RNAi	18°C	5	12
	29°C		9

K=3

		Cluster 3	Cluster 2	Cluster 1
Control	18°C	36	1	
	29°C	40		
rab5-RNAi	18°C	6		11
	29°C	1	1	15
syx7-RNAi	18°C	4	4	6
talin-RNAi	18°C		16	
	29°C		16	
rab8-RNAi	18°C	4	6	6
	29°C			9

K=4

		Cluster 1	Cluster 4	Cluster 3	Cluster 2
Control	18°C	37			
	29°C	40			
rab5-RNAi	18°C	6		3	8
	29°C	1		10	6
syx7-RNAi	18°C	3	4	6	1
talin-RNAi	18°C		15		1
	29°C		16		
rab8-RNAi	18°C	4	4		8
	29°C				9

K=5

		Cluster 1	Cluster 3	Cluster 5	Cluster 2	Cluster 4
Control	18°C	17	20			
	29°C	29	11			
rab5-RNAi	18°C	1	5		3	8
	29°C		1		10	6
syx7-RNAi	18°C	2	1	4	6	1
talin-RNAi	18°C			15		1
	29°C			16		
rab8-RNAi	18°C	3	1	4		8
	29°C					9

Figure 4.7: Cluster analysis by the K-means algorithm
(A) Distance matrix of Euclidean distance between each pair of cells in the 15-dimensional sample space across all feature frequencies. The K-means algorithm operates on this matrix. The large group of mutually closely positioned cells in the bottom left contains primarily control TCs. The group in the centre of the plot is mainly formed by *talin*-RNAi cells, and the smaller groupings near the top right consist of *rab5*-RNAi, *syx7*-RNAi and *rab8*-RNAi cells. (B) "Knee" plot to assess quality of clustering by K-means, showing within-sum-of-squares as a measure of the dispersion of points around their cluster centroid. "Knees" such as at K=2 and K=4 indicate less-than-average dispersion. (C) Assessment of clustering quality using the silhouette method, showing silhouette score as a measure of distance between clusters. The dashed line indicates the highest silhouette score, i.e. maximum between-cluster difference. (D) Resulting assignments of cells from each sample into clusters by K-means. The specific numbering of clusters is arbitrary. For display, clusters were rearranged to keep those with similar compositions between different K-means runs in the same order.

Hierarchical clustering

The dendrogram produced by the hierarchical clustering method shows four main groups, and five cells that do not fit well into any other (Fig. 4.8A). The cells from each sample were distributed in these four groups in a similar manner as they were distributed by K-means into clusters when specifying K=4 (compare Fig. 4.8B to 4.7D). However, this approach sorted a larger number of *rab8*-RNAi/18°C cells, as well as some *talin*-RNAi cells into a cluster with control cells. Four *syx7*-RNAi cells remained solitary in the hierarchical approach, indicating that they are distant from all other cells. In turn, the control and *talin*-RNAi clusters only contain one *syx7*-RNAi cell each, suggesting that the grouping of these cells by K-means was the consequence of the condition that all cells must be assigned to a cluster. This supports the conclusion from K-means clustering that the dataset contains four distinct groups of cells that reflect the associations expected. Controls and *talin* interference are distinguished, and *rab5* is associated with *syx7*. Lastly, *rab8* was again associated with *rab5*.

Visualising the feature frequencies along with the dendrogram shows that the Control cluster contains cells with low frequencies of all features, and contains a sub-cluster with (non-control) cells that have a moderate to high frequency of Curled Tip and Wavy Lumen but no or few other features (Fig. 4.8A). The *talin*-RNAi cluster has a characteristic combination of high frequencies of Delayed Branching, Curled Tip and Wavy Lumen. The *rab5*-/*syx7*-RNAi cluster is defined by high frequency of Hairy Branch and absent Postjunction Curl and Interjunction Curl, combined usually with high frequencies of Curled Tip and Disrupted Tip. It further subdivides between cells that also had Wavy Lumen and others that did not. Those *syx7*-RNAi cells that were not sorted into this cluster either had no Hairy Branch occurrences, or had a high frequency of Wavy Branch and Disconnect. Finally, the *rab5*-/*rab8*-RNAi cluster unifies moderate to high frequencies of Hairy Branch, Postjunction and Interjunction Curl, Hairy Junction, Curled Tip and Wavy Lumen, but low frequencies of Disrupted Tip. Degenerate Lumen, Double Lumen, Cyst, U-turn and Triple Junction do not seem to contribute towards segregating cells into specific clusters and are therefore unlikely to be specific consequences of the RNAi constructs.

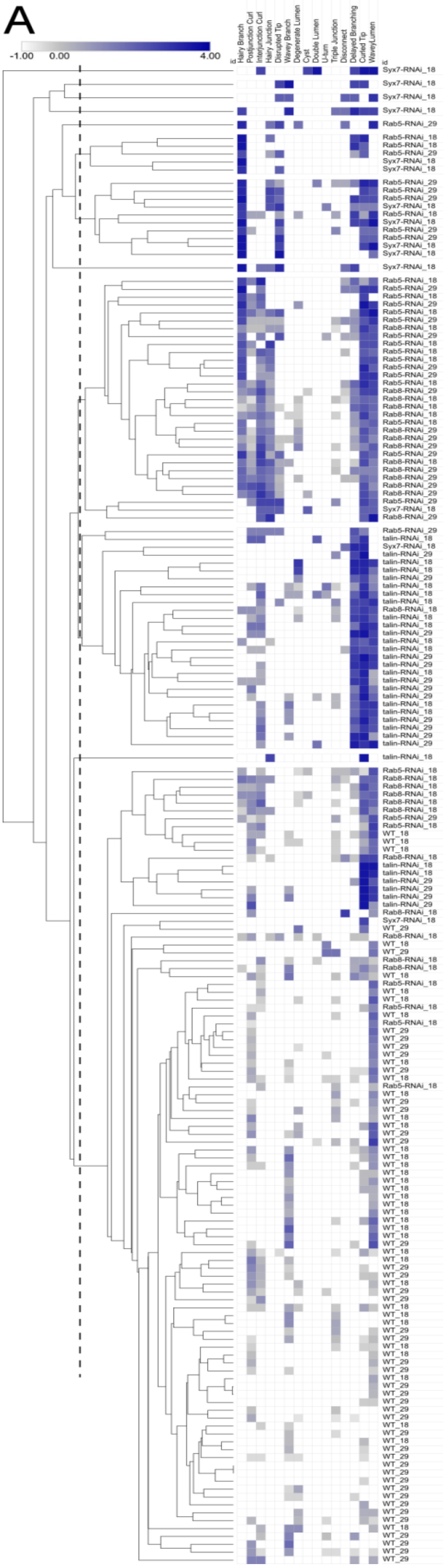

B

Hierarchical clustering (Euclidean distance)

		Cluster 4	Cluster 3	Cluster 1	Cluster 2	Unclustered
Control	18°C	37				
	29°C	40				
rab5-RNAi	18°C	6		3	8	
	29°C	1	1	7	8	
syx7-RNAi	18°C	1	1	7	1	4
talin-RNAi	18°C	3	13			
	29°C	4	12			
rab8-RNAi	18°C	10	1		5	
	29°C				9	

Figure 4.8: Cluster analysis by hierarchical clustering

(A) Dendrogram showing groupings produced by a hierarchical clustering algorithm operating on Euclidean distance. Horizontal length of dendrogram lines corresponds to dissimilarity. In the heat map, each row corresponds to one TC and each column to one feature category. Colour indicates normalised log-transformed feature frequency (see Methods) of that feature for that cell from low (grey) to high (blue) frequency. Completely absent features have a log-transformed frequency of -1 and are indicated by a white square. Empty lines in the heatmap indicate groupings after applying a dendrogram height cutoff (dashed line). Column headings, left to right: Hairy Branch, Postjunction Curl, Interjunction Curl, Hairy Junction, Disrupted Tip, Wavey Branch, Degenerate Lumen, Cyst, Double Lumen, U-turn, Triple Junction, Disconnect, Delayed Branching, Curled Tip, Wavey Lumen.

(B) Clustering results using the indicated dendrogram height cutoff, with subsequent fusion of the top-most cluster where the root node was slightly above the dendrogram cutoff.

Multidimensional visualisation

The cluster analysis demonstrates that phenomic assessment of TC phenotypes as presented here is capable of revealing expected functional associations between genes. This is effectively a more comprehensive implementation of the traditional "similar phenotype, similar function" paradigm of reverse genetics. It allows inferences of gene function when penetrance is incomplete on two levels (penetrance per cell and penetrance per branch of each cell), and when genes whose functions are not associated at the resolution of interest are associated with qualitatively similar aberrant morphologies. An intuitive way of inspecting the quality of discrimination between different TC phenotypes can be provided by plotting the data points and their cluster assignments. However, this is impossible for a multidimensional dataset such as this, and a method of dimensionality reduction is required to visually represent the data in a two-dimensional plot. One common technique to achieve this is to perform PCA, and then plot the first two principal components for each data point as the x- and y-axis. However, since the first two principal components only capture a small fraction of this dataset's variance (see Fig.4.6B), this plot would not produce a realistic impression of the original data. An alternative technique to achieve this is multidimensional scaling (MDS), a more generalised algorithm similar to PCA but better suited for graphical representation of multidimensional data in a plot.

Using Kruskal's non-metric MDS algorithm and the Manhattan distances between the data points results in a two-dimensional plot that illustrates both the segregation of the identified clusters (Fig. 4.9A) and the structures in the underlying data that permitted this categorisation by the clustering algorithms (Fig. 4.9B). Control cells form a tightly clustered group to the left of the plot. Distant from it, to the bottom right, is a group of *talin*-RNAi cells. The space above these two groups is occupied by mixed groups of *rab5*-, *syx7*- and *rab8*-RNAi cells. This illustrates that the RNAi-expressing cells that were assigned to the same cluster as controls both by K-means and hierarchical clustering are located very close to the control cells in the multidimensional space. Their cluster assignment is therefore reflect the quantitative similarity of these cells to controls. The mixing of cells from different clusters in Fig. 4.9A, and the location of the four cells without cluster assignments, demonstrate that MDS only provides an approximate view of the sample space. In the 15-dimensional sample space, the boundaries of different clusters do not overlap and unassigned cells lie outside of all clusters' boundaries. Fig. 4.9A also shows that *syx7*-RNAi phenotypes spread across large distances in the sample space. This is due to these cells' low branch numbers, which causes a small absolute count of morphological features to translate into high per-branch frequencies. Despite these shortcomings, this visualisation illustrates that phenomic cluster analysis is a suitable method for distinguishing phenotypes in TCs in a way that enables functional inference according to the traditional paradigm of reverse genetics.

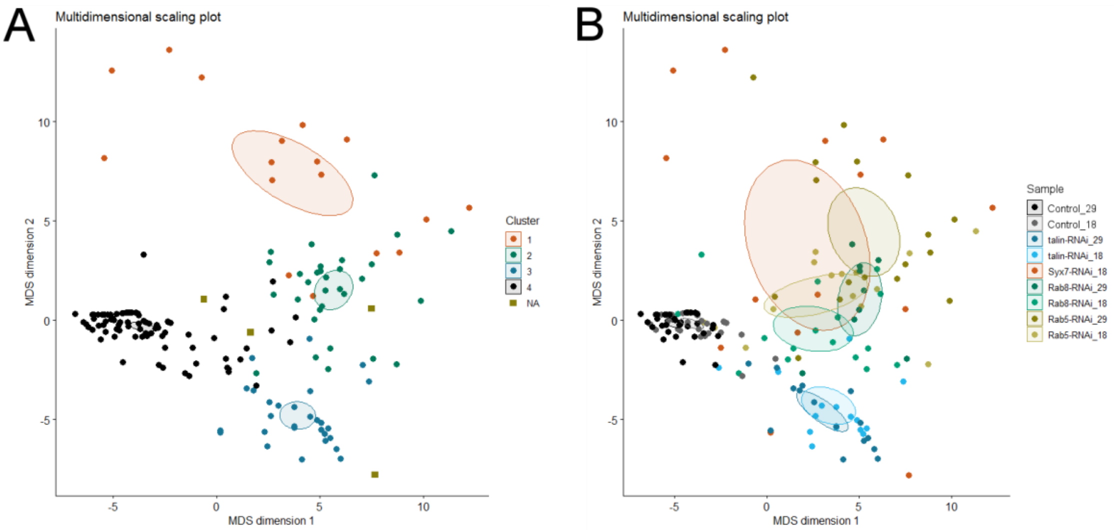

Figure 4.9: Multidimensional scaling of feature frequencies
Two-dimensional representation of the 15-dimensional sample space obtained using Kruskal's non-metric multidimensional scaling and Manhattan distances. Each point represents one TC. Both (A) and (B) show the same data, coloured either by cluster assignment according to hierarchical clustering (A), or sample (B). Ellipses show 95% confidence estimations of the location of the respective cluster or sample's mean.

4.2 YRab-gfpIR: An indirect RNAi screen for Rabs involved in tracheal morphogenesis

Having identified suitable methods for analysing TC phenotypes, I performed an RNAi-based knockdown screen of the *rab* family of genes. These "master regulators of membrane trafficking" (Pfeffer, 1994, 2017) were a promising candidate family to study for understanding how TCs achieve their large size and complex morphology, coordinating the simultaneous growth of polarised membrane surfaces with branching morphogenesis. In RNAi knockdown screens, a major concern are false positives. The transgenic elements that are used to integrate RNAi constructs in the genome have been shown in some cases to cause mutant-like phenotypes simply due to the insertion itself, rather than a specific interference with a target gene (Green et al., 2014). Additionally, RNAi constructs can unspecifically interfere with expression of genes other than the one targeted (Echeverri et al., 2006), also known as off-target effects. This was a particular concern for TCs, where wildtypes and experimental controls produce various morphologies that could be considered defects (see section 4.1). Off-target effects could impact the overall health of the cell and lead to increased frequencies or severities of these unspecific morphological features. To circumvent this risk, I used the library of *Drosophila* lines with endogenously YFP-tagged *rab* genes. Expressing an RNAi transgene targeting YFP in these lines should eliminate the *rab* gene product, while the same transgene can be expressed in a line without YFP-tagged genes to control for off-target effects. I prepared the *Drosophila* lines required to obtain larvae in which all mRNA of a target *rab* contains the YFP sequence, and which express an RNAi construct targeting YFP in all tracheal cells using *btl*-Gal4. I screened these larvae for abnormalities in their dorsal TCs to identify Rabs involved in TC development. The tools used throughout this chapter are targeted against GFP, but also function against YFP due to the similarity in their DNA sequences and protein structures.

4.2.1 Endogenous expression level of YFP-tagged Rab proteins

Given the structure of TCs, many genes' functions are associated with specific distributions of their mRNA or protein products within the cell. Several Rabs have been reported to show polarised distributions in embryonic tracheal cells of the dorsal trunk, for example with enrichments near the apical membrane (Caviglia et al., 2016). Such localisation patterns are often functionally relevant for Rabs in particular, indicating membrane compartments involved in their associated trafficking pathways. To test if any Rabs show specific enrichment patterns in TCs, I dissected wandering third-instar larvae of each YRab line and stained the YRab protein using an anti-GFP antibody.

Out of the 27 YRabs, none showed a striking pattern in their localisation in TCs (Fig. 4.10). All YRabs had a combination of more or less uniform punctate and diffuse staining at varying intensity levels. The YRab with the strongest staining was YRab1 (Fig.4.10B), followed by YRab7 (Fig.4.10F) and YRab11 (Fig.4.10I). Despite testing several antibodies from different manufacturers and different variations of the dissection protocol (see Methods), TCs in negative controls (the non-transgenic mutant line w^{1118}) consistently showed a punctate staining (Fig. 4.10A, top panel). This unspecific staining was weak but sufficient to distinguish the TC's contour from detector noise. Consequently, individual punctae in such stainings do not specifically indicate vesicles carrying a Rab protein, and it was not possible to determine whether YRabs with low staining intensity were expressed or not. Instead, to assess YRab expression levels semi-quantitatively, the mean staining intensity in the cell was measured, the detector background was subtracted, and the resulting difference was compared to the corresponding measurement of the negative control (Fig. 4.10M). The quantification indicates that TCs also express YRabs 2, 5, 6, 8, 10, 39 and 40.

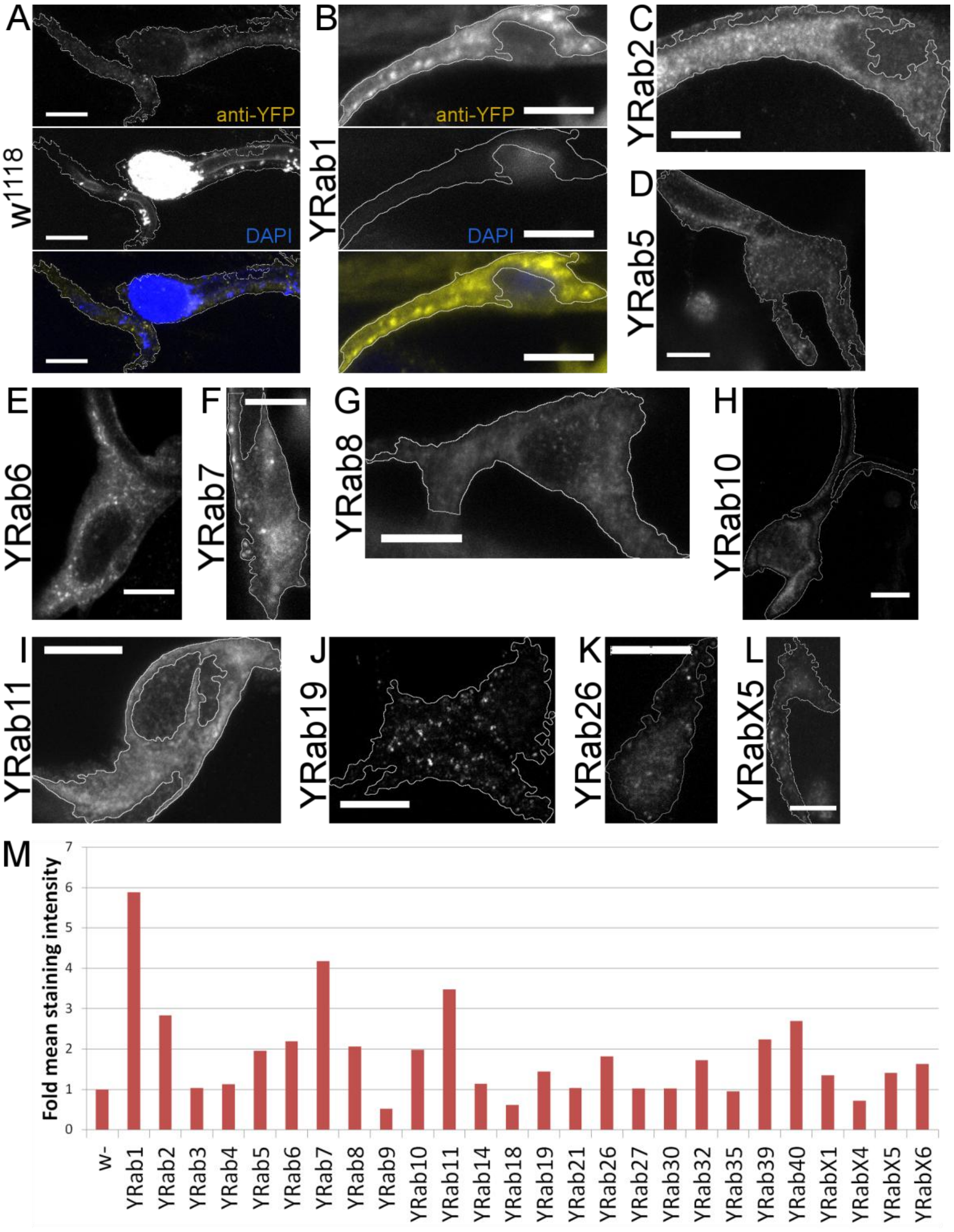

Figure 4.10: Expression of endogenously YFP-tagged Rab proteins in terminal cells

Immunostained dorsal terminal cells of third-instar wandering larvae collected from the indicated *Drosophila* lines. The primary antibody used was a rabbit anti-GFP and also recognises YFP. The secondary was an anti-rabbit antibody labelled with Alexa Fluor 568, emitting orange to red light. The staining can therefore be distinguished from endogenous yellow fluorescence. All micrographs were acquired with the same settings and 20 slices of 290nm thickness were z-projected for quantification and display. Thin white outlines indicate the region within which staining was quantified.

(A) Negative control terminal cell of the w^{1118} line that expresses no GFP or YFP. An unspecific punctate staining was consistently found in control cells. Top: Fluorescence signal from the secondary antibody labelled with Alexa Fluor 568. Mid: 405nm channel. Detects both diamidino-phenylindole (DAPI) and autofluorescence of the apical extracellular matrix inside the tube. Bottom: Overlay of the above two pictures.

(B) Positive control terminal cell of the YRab1 line where Rab1 is endogenously tagged with an N-terminal YFP insertion. The nucleus (DAPI channel) appears faint because it is located below the focal plane. Top: Fluorescence signal from the secondary antibody labelled with Alexa Fluor 568. Mid: 405nm channel. Detects both diamidino-phenylindole (DAPI) and autofluorescence of the apical extracellular matrix inside the tube. Bottom: Overlay of the above two pictures.

(C-L) Examplary terminal cells are shown from some YRab lines with high expression and some that were later found to be associated with defect phenotypes. In each case only the 568nm channel is shown, detecting anti-GFP staining.

(M) Quantification of YRab expression levels relative to negative control. Controls and YRab samples were dissected, stained and imaged in parallel. A simple segmentation procedure was used to identify the region corresponding to cytoplasm and the mean pixel intensity was measured. The mean intensities were averaged across all cells for each YRab and divided by the mean of the control cells in the same sample.

4.2.2 Selection of YFP-interference construct

There are several published RNAi and nanobody constructs to knockdown GFP or its derivates including YFP. RNAi constructs express RNA products that bind a complementary mRNA and cause its degradation. Nanobodies are single-domain antibodies derived in this case from the V_HH fragment of camelid heavy-chain antibodies, containing the epitope-binding domain. Fused to the N-terminal F-box of the ubiquitin ligase Slimb, the product causes degradation of a targeted protein. I tested two different RNAi constructs and the deGradFP nanobody construct (nicknamed "vhhGFP4") (Caussinus et al., 2012) inserted using two different transposon elements (a P- and an M-element). Due to its high expression both in TCs and epidermal cells, YRab1 was used as a knockdown target to compare the different constructs. YRab1 is uniformly and strongly expressed in all epidermal cells. The amount of YFP-tagged Rab1 protein in these cells is sufficient to visualise punctate structures in the cytoplasm by imaging YFP, without the need for immunostaining (Fig. 4.11A-D). I induced expression of the different constructs using the *engrailed*-gal4 driver, which is expressed in a striped pattern in the epidermis of third-instar larvae. This allows visualisation of wildtype and knockdown-expressing cells within one individual for juxtaposed comparison (Fig. 4.11A'-D'). For all constructs, yellow fluorescence was abolished incompletely. The most efficient elimination by fraction was achieved by GFP-IR-I (Fig. 4.11E), making this the construct of choice for future experiments.

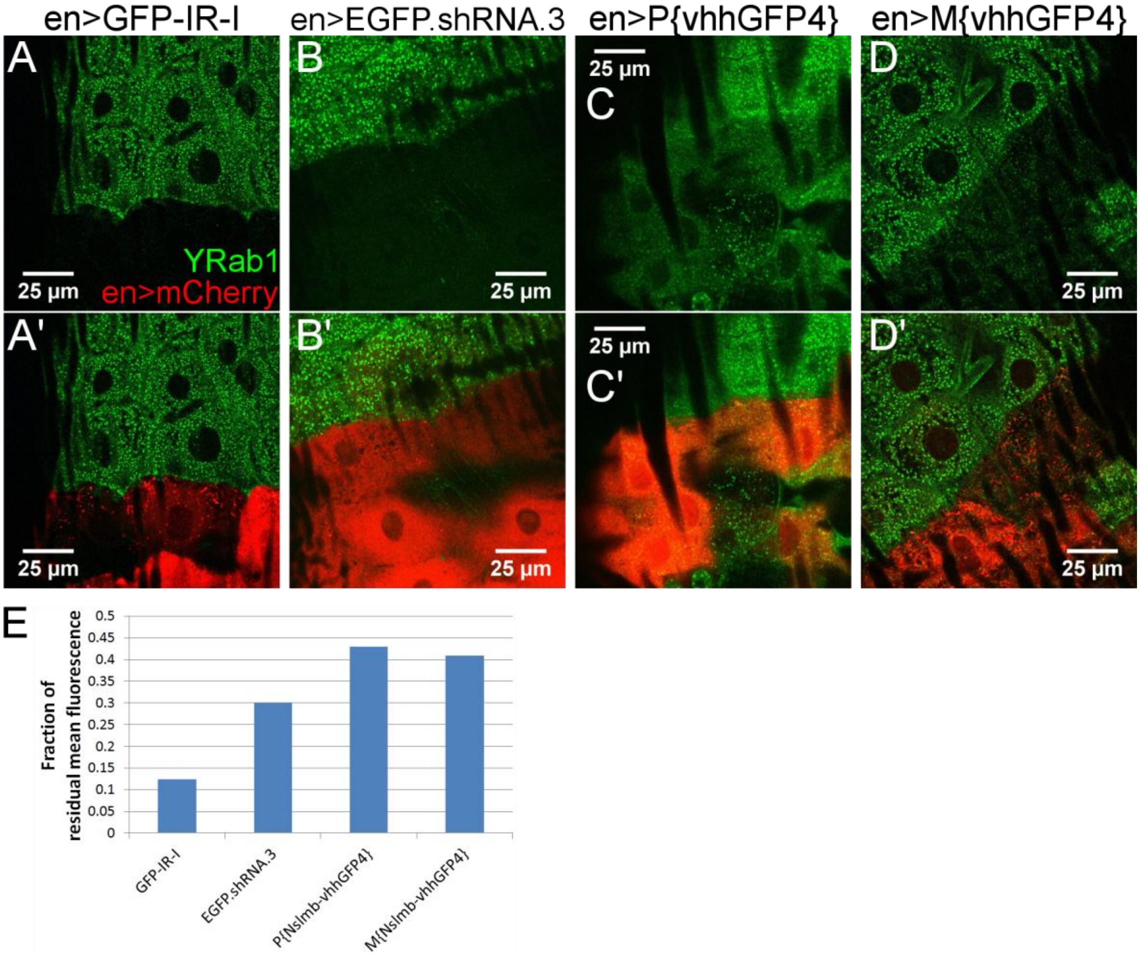

Figure 4.11: Comparison of GFP-interference constructs in the epidermis

Four transgenic constructs to interfere with GFP expression were tested for their ability to eliminate expression of the endogenously YFP-tagged Rab1 protein. The constructs are controlled by UAS and driven by *engrailed*-Gal4, which is expressed in a stripe pattern in the epidermis, thereby providing sample and control within the same animal. An additional UAS-controlled mCherry transgene marks Gal4-expressing cells. GFP-IR-I and EGFP.shRNA.3 are RNAi constructs targeting different portions of the GFP sequence. Nslmb-vhhGFP4 (vhhGFP4) encodes the deGradFP nanobody (Caussinus et al., 2012) that targets the YFP-tagged protein for degradation, inserted into the genome using a P- or M-element.

(A-D') Micrographs show emission from fluorescent proteins in 1.5µm thick optical slices acquired from the epidermis of heat-fixed third-instar larvae. Green: fluroescence from YFP-tagged Rab1. Red: fluroescence from mCherry driven by *engrailed*-Gal4.

(E) Quantification of relative YRab1 fluorescence in cells expressing the interference construct compared to those not expressing it. The mean pixel intensity of YRab1 emission in an area within the *engrailed* stripe was divided by the mean intensity in an area outside of the stripe in the same image.

4.2.3 Preparation of YRab-gfpIR **Drosophila** *lines and experimental procedure*

To knock down a YFP-tagged Rab in the tracheal system, the experimental larvae needed to be homozygous for the YRab allele of the *rab*, and additionally express GFP-IR-I under the *btl*-Gal4 driver. Gene product not tagged with YFP would not be affected by the knockdown, and it was assumed that knocking down the product from only one of the two *rab* alleles would be insufficient to elicit defect phenotypes. To obtain animals of this genotype, two *Drosophila* lines were required for each YRab: one carrying the YRab allele and GFP-IR-I, and one carrying the YRab allele and *btl*-Gal4. This implied that to test all 27 YRabs, a total of 54 lines were needed. The *rab* loci are distributed across all three chromosomes of the *Drosophila* genome (seven on X, ten each on the 2nd and 3rd chromosome), GFP-IR-I is inserted on the 2nd and *btl*-Gal4 on the 3rd chromosome. I therefore devised six crossing schemes resulting in the two required genotypes depending on the chromosome on which the YRab was located (Appendix 8.2). I also designed genotyping primer pairs flanking the start codon of each *rab* gene's protein coding region such that wildtype and YRab alleles can be distinguished by the size of their PCR products (see Methods and Appendix 8.3), and the insertion can be additionally confirmed by sequencing the PCR product. Using these primers, I verified the homozygosity of the YRab allele for each stock generated. Some lines were not viable with a homozygous YRab chromosome and were therefore kept over a balancer with a selectable marker. This made it possible to select either homozygous adults for the YRab-gfpIR experimental cross, or homzoygous F1 larvae if adults were not viable.

When generating YRab-gfpIR larvae for experiments (see Methods), the correct genotype was confirmed by microscopy and PCR: Presence of *btl*-Gal4 was confirmed by including the UAS-DsRed construct, leading to expression of the DsRed fluorescent protein in tracheal cells. The DsRed protein and mRNA structures are not derivatives of GFP and are therefore not targeted by GFP-knockdown constructs. Presence of the GFP-IR-I construct and homozygosity for the YRab allele were confirmed by genotyping PCR from squish extracts of the screened larvae.

4.2.4 Validation of YRab-gfpIR

The principle of interfering with expression of endogenously tagged *rab* genes by expressing an RNAi construct against the YFP-tag sequence ("YRab-gfpIR") has been tested in the past (Dunst et al., 2015). Here, GFP-RNAi was used to knock down YRab23 and YRab35 in the wings. I additionally validated the application of the technique to the tracheal system.

Elimination of endogenous YRab1 fluorescence

The measurable endpoint of RNAi is the reduction of the protein product's concentration in the target cell. YRab1 presented a valuable tool as its endogenous expression level in TCs is high enough for fluorescent visualisation. Similarly to epidermal cells, it forms punctate structures also in TCs (Fig. 4.12A). To test the efficacy of YRab-gfpIR on YRabs in TCs, I performed a preliminary RNAi-cross producing individuals heterozygous for the YRab allele. In this constellation, only some of the *rab* mRNA contains the YFP sequence, allowing the wildtype copy to rescue deleterious effects caused by RNAi. The resulting TCs had no detectable YFP signal (Fig. 4.12B), indicating a drastic reduction in the targeted gene product.

Functional comparison between RNAi and nanobody

Even though in the previous test in the epidermis (section 4.2.2), the nanobody (vhhGFP4) construct did not reduce YRab1 to undetectable levels (Fig. 4.11C-D'), I tested whether the nanobody was more efficient than RNAi in the tracheal cells. Rather than quantifying residual protein fluorescence, I identified a quantifiable functional readout of the knockdown, i.e. phenotype. As described further below, YRab19-gfpIR caused an excess number of cells to assume the TC fate (Fig. 4.12C). I tested whether YRab19-gfpNano was able to induce a stronger phenotype, but found that the frequency of excess TCs was similar as caused by RNAi (mean delta: 1.3; 95% CI: -0.5 to 3.3; p=0.4; Fig. 4.12C'). This indicates that despite their different efficiencies in the epidermis, nanobody and RNAi achieve a comparable efficiency of knockdown in the tracheal system.

Recapitulation of known Rab-related terminal cell phenotypes

Overall, not many Rab-related tracheal phenotypes have been published. The following TC phenotypes could be expected based on the literature: tube dilations for Rab5 (Schottenfeld-Roames et al., 2014), excess tubules near the nucleus for Rab35 (Schottenfeld-Roames and Ghabrial, 2012) and reduced branch numbers for Rab10 and Rab11 (Jones et al., 2014). Of these, the phenotype for Rab5 was associated with the *rab5*^{2} null allele, a p-element induced deletion of the *rab5* promoter up to the first exon (Wucherpfennig et al., 2003), whereas the other three were associated with overexpression of variant Rab proteins that are predicted to be inactive due to a mutation in the predicted GTP-binding site (Zhang et al., 2007). RNAi induces loss-of-function similar to a deletion of the targeted gene, meaning that the Rab5 phenotype should be reproduced, but the phenotypes associated with Rab10, 11 and 35 may not be elicited by RNAi since these were not necessarily loss-of-function phenotypes. In addition to this, the phenotypes found in the preceding phenomic study (section 4.1) for Rab5-IR and Rab8-IR should be reproduced.

For YRab5-gfpIR, assessing TC morphology was not possible because no larvae of the correct genotype hatched (*YRab5,GFP-IR-I/YRab5;*btl-*Gal4,UAS-DsRed).* Embryos of all stages could be found, however, suggesting that death occurred close to the end of embryogenesis or during hatching of the larva from the egg. Lethality at this stage could be due to suffocation because the tracheal system failed to replace the liquid in the lumen with gas, a process for which Rab5 is required (Tsarouhas et al., 2007). The observed lack of surviving larvae is thus consistent with pan-tracheal Rab5 loss. YRab5-heterozygous siblings (Y*Rab5,GFP-IR-I/CyO;*btl-*Gal4,UAS-DsRed*) were viable and had a normal tracheal phenotype. To confirm that TCs in YRab5-gfpIR had similar phenotypes as when expressing Rab5-IR, I attempted to generate YRab5-gfpIR animals with the *dsrf*-Gal4 driver instead of *btl*-Gal4, thereby restricting expression of the RNAi transgene to TCs rather than the entire tracheal system. However, no YRab5-homozygous larvae could be obtained with this driver either. YRab5-heterozygous larvae were also not viable with this driver, suggesting that the observed lethality was not due to effects in tracheal cells. The *dsrf*-Gal4 driver is specific to TCs in the tracheal system, but it also drives expression in cells outside the tracheal system, which could be the reason for this lethality.

YRab-gfpIR larvae for YRab10, YRab11 and YRab35 showed no abnormal phenotypes in their dorsal TCs that corresponded to the phenotypes associated with each Rab in published literature. At least five YRab-gfpIR larvae (approx. 70 dorsal TCs in total) were screened for each Rab.

YRab8-gfpIR caused an abnormal TC phenotype which was qualitatively similar to the "hairy" phenotype caused by expression of Rab8-IR (Fig. 4.12F & H). Neither of the two produced defects as severe as observed during the phenomic study (section 4.1), because in that case the experiment included overexpression of Dicer2, which amplifies the efficiency of RNAi. The TC phenotype was normal in heterozygous YRab8-gfpIR animals, i.e. larvae with one wildtype copy of the *rab8* gene and one endogenously YFP-tagged allele (Fig.4.12G), indicating that a partial interference with Rab8 does not significantly impact TC morphogenesis. TCs also had a normal phenotype in YRab8-homozygous animals that were not expressing GFP-IR-I (data not shown), indicating that the defects are not due to the YFP-tag itself.

Recapitulation of known Rab-related tracheal phenotypes

Since the *btl*-Gal4 driver was chosen to target all tracheal cells with YRab-gfpIR, I also tested whether published phenotypes associated with Rabs for the tracheal system as a whole were reproduced. In this regard, besides the requirement of Rab5 for tracheal lumen clearange as described above, Rab39 is known to be involved in the dorsal anastomosis of fusion cells (Caviglia et al., 2016). The phenotype associated with Rab39 is a failure of the dorsal branch fusion process and was observed when overexpressing a putative inactive mutant Rab39 protein under the *btl*-Gal4 driver. This phenotype therefore does not necessarily reflect a loss-of-function, like previously the TC phenotypes associated with overexpressed Rab mutants. In YRab39-gfpIR larvae, an average of 1.7 of the total 8 dorsal branch pairs failed to fuse, as opposed to 0.6 pairs in the control (mean delta 1.1; 95% CI: 0.5 to 1.7; $p<0.0005$; Fig. 4.11D).

Based on these experiments, I concluded that YRab-gfpIR was a viable method for discovering tracheal loss-of-function phenotypes related to Rabs. In YRab-gfpIR larvae, the fluorescence of YRab proteins is undetectable, and expected loss-of-function phenotypes are reproduced. Additionally, this showed that the GFP-IR-I construct targeting *yrab* mRNA induces loss-of-function at a similar level as the deGradFP nanobody targeting YRab protein.

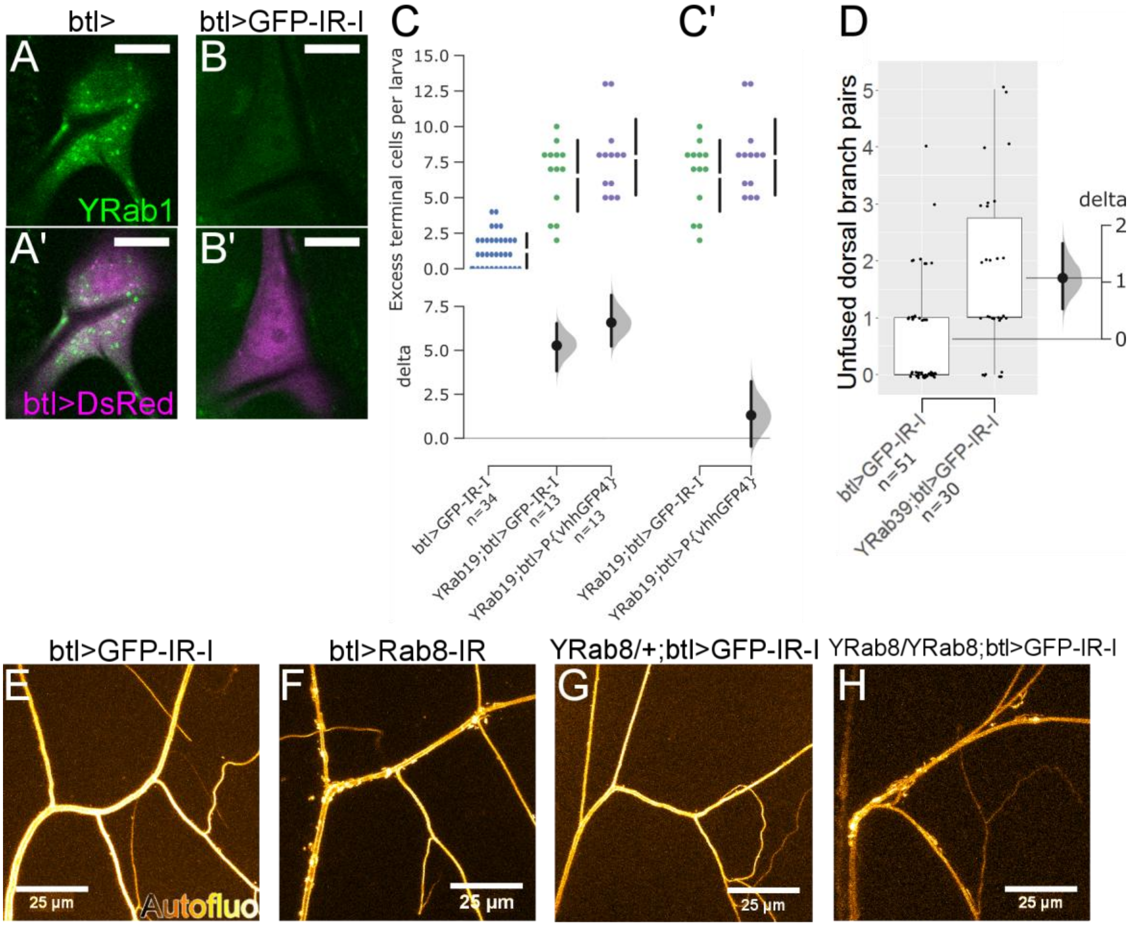

Figure 4.12: Validation of the YRab-gfpIR method in terminal tracheal cells
(A-B') Indirect elimination of YRab1 protein expression in terminal cells by targeting YFP-tagged *rab1* mRNA with the RNAi construct GFP-IR-I (combination referred to as YRab-gfpIR). (A) Dorsal terminal cell of a heat-fixed third-instar control larva with one of the two *rab1* alleles endogenously tagged with YFP (YRab1), and expressing the DsRed fluorescent protein under control of *btl*-Gal4, which drives expression in all tracheal cells. Green: YRab1 fluorescence. (A') Overlay of (A) with the DsRed channel (magenta). (B) Terminal cell prepared and imaged in parallel to (A) in a larva that additionally expresses GFP-IR-I driven by *btl*-Gal4. (B') Overlay of (B) with the DsRed channel.
(C) Functional comparison estimating the impact of GFP-IR-I, which degrades target mRNA, and of deGradFP (vhhGFP4), which degrades target protein, on the number of excess dorsal terminal cells formed in third-instar larvae with both copies of *rab19* endogenously YFP-tagged (YRab19). This defect was discovered in the screen described later and retroactively used for a quantitative comparison. Constructs were driven by *btl*-Gal4, and mothers of observed larvae were YRab19-homozygous. Controls had two wild type copies of *rab19*. Any terminal cell originating from a dorsal branch in addition to the stereotypical single one was considered excess. Each dot in the upper graph represents one larva. In the lower panel, each effect size estimation graph illustrates the potential range of the mean difference between each sample and control, calculated by bootstrapping. Large dot: mean difference/delta. Black bars: 95% confidence interval. Grey plot: distribution of bootstrapped mean deltas. P-values are not illustrated to avoid the known pitfalls (Ho et al., 2018), but are reported in the main text for completeness.

(C') Estimation of the difference between the GFP-IR-I and the deGradFP (vhhGFP4) samples shown in (C).
(D) Validation of a defect phenotype expected from literature. Rab39 is associated with a tracheal defect where the fusion of dorsal branch pairs fails (Caviglia et al., 2016). The box and dot plots show the frequency of unfused dorsal branch pairs in control larvae, expressing GFP-IR-I in all tracheal cells driven by *btl*-Gal4, compared to larvae where additionally, Rab39 is endogenously YFP-tagged (YRab39) and therefore subject to degradation by GFP-RNAi. Each dot represents one larva. The overlaid graph estimates the effect size associated with the presence of the YFP-tag on Rab39 in the same manner as the graphs in (C).
(E-H) Validation of a defect phenotype expected from the preceding phenomic study. Rab8 is associated with a terminal cell defect where the tube morphology becomes "hairy". Micrographs show autofluorescence emitted by the apical extracellular matrix of dorsal terminal cells in heat-fixed third-instar wandering larvae of the indicated genotype. Expression of GFP-IR-I (E, G, H) or Rab8-IR (F) was driven in all tracheal cells by *btl*-Gal4. An additional DsRed marker was co-expressed as in (A') but is not shown here. The effect of indirect RNAi against Rab8 via the endogenous YFP-tag was assessed in larvae with one of the two alleles tagged (G) and larvae with both alleles tagged (H).

4.2.5 Effects of YRab-gfpIR on terminal cell morphogenesis

Having validated the YRab-gfpIR method for use in the tracheal system, I performed YRab-gfpIR experiments for all 27 YRabs using the 54 lines I generated and screened for loss-of-function phenotypes related to TCs. From this, I aimed to establish an overview of membrane trafficking routes that are active in TCs and involved in their morphogenesis. Rabs are assigned general importance for cells' ability to function in articles related to them, and my main hypothesis was that TCs depend on Rab-mediated membrane trafficking to grow and coordinate the relative sizes of their basal and apical membrane domains. Consequently, I expected severe loss-of-function phenotypes in TCs for many Rabs. For this experiment, I generated YRab-gfpIR larvae for each of the 27 endogenously YFP-tagged Rabs. These larvae carried the *btl*-Gal4 element, driving expression of a GFP-RNAi construct and DsRed as a reporter in all tracheal cells. Additionally, both alleles of one *rab* gene had a YFP sequence inserted at the beginning of the protein coding region. In tracheal cells, the GFP-RNAi construct therefore mediates degradation of the tagged *rab* mRNA and leads to a loss-of-function of that Rab. As a negative control, I tested whether expressing the GFP-IR-I construct causes TC defects by itself, using larvae that express GFP-IR-I under *btl*-Gal4 but have no GFP- or YFP-tagged genes. Any phenotypic differences observed in YRab-gfpIR should therefore be due to loss-of-function of the endogenously YFP-tagged *rab* gene. To interpret phenotypes observed during this screen, I used the morphological feature categories identified in the preceding phenomic analysis of TC morphology. The results of this analysis showed that these features, when quantitated, provide a valid basis for inferring functional associations between genes. All YRab-gfpIR crosses were carried out at 29°C to increase the efficiency of RNAi and obtain the highest possible penetrance for any potential phenotypic defects.

During preliminary screening, I extended the set of morphological features with an additional category denoted "asymmetric autofluorescence". This refers to a particularly bright region of autofluorescence which is not in line with the regular, symmetric tube autofluorescence in wildtype cells. This took two different forms. Either a brightly fluorescent stripe lined a portion of a tube longitudinally (Fig. 4.13E & F), or the width and brightness of the autofluorescent layer was increased drastically at one point (Fig. 4.13G & H). The second case was often followed by a collapse of the tube immediately distal to the point of asymmetry (i.e. a "Disconnect"). After scoring all cells, I removed the categories Cyst and Disrupted Tip from the analysis because these defects had not occurred in any of the samples.

I screened all dorsal TCs of the third to seventh dorsal branch pairs (positioned in the larval abdominal segments 3-6) in at least five larvae for each Rab, resulting in a minimum of approximately 50 TCs screened per YRab-gfpIR cross. As during the phenomic study, I observed the TCs' cellular morphology using the cytoplasmic fluorescent protein (DsRed in this case) and the morphology of their subcellular tube using the autofluorescence that the apical extracellular matrix (aECM) in the lumen emits when illuminated with a 405nm wavelength laser. I recorded complete micrographs of at least 2 TCs for each Rab for phenomic scoring regardless of phenotype. For those Rabs where TCs appeared abnormal during screening, a larger number was recorded for quantitative scoring, and the YRab-gfpIR cross was repeated with a second set of parents to confirm the result. YRab6-gfpIR larvae did not survive until the third instar stage at 29°C and the cross was therefore repeated at 25°C to obtain larvae of the correct developmental stage.

Figure 4.13A shows the mean frequencies of each morphological feature per 100 branches. This can also be thought of as the percentage of branches showing the respective feature per cell, because none of the features occurred more than once on any branch. The values given for *n* indicate only the number of TCs that were quantitated. The total number assessed qualitatively was at least 50 in each case. Abnormal TC phenotypes were only observed in YRab-gfpIR larvae for Rab2, Rab6, Rab8 and Rab10.

Like previously observed with Rab8-IR in the phenomic study, the number of branches formed by TCs in YRab8-gfpIR larvae was substantially reduced compared to the average of 28.6 branches in negative control TCs (Fig.4.13C; mean 16.4; delta: -12.3; 95% CI: -9.2 to -15.7; $p<0.0001$). Likewise, the fraction of "healthy" branches, i.e. branches showing none of the various morphological features, was lower than the average healthy fraction of 0.85 in controls (Fig. 4.13D; mean 0.61; delta: -0.25; 95% CI: -0.16 to -0.35; $p<0.001$). Despite the presumed lower RNAi efficiency due to the lower culture temperature, YRab-gfpIR against Rab6 had a stronger impact on the overall health of TCs, with few of the affected cells forming more than 10 branches (mean 7.8; delta: -20.9; 95% CI: -18.4 to -23.3; $p<0.001$). These TCs also only rarely formed healthy branches (Fig.4.13D; mean 0.15; delta: -0.70; 95% CI: -0.53 to -0.81; $p<0.001$). In contrast, TCs in YRab2-gfpIR and YRab10-gfpIR larvae had normal numbers of branches (Fig.4.13C). Despite this, the fraction of healthy branches was lower than controls in both cases. YRab10-gfpIR had a similar reduction as YRab8-gfpIR (mean 0.67; delta vs. control: -0.18; 95% CI: -0.11 to -0.27; $p<0.001$), while the reduction in YRab2-gfpIR TCs was milder (mean 0.74; delta: -0.11; 95% CI: -0.05 to -0.19; p<0.05).

The YRab-gfpIR phenotype associated with Rab8 was characterised by the same defects as previously found for expression of the Rab8-IR construct, namely the Hairy Branch and Hairy Junction feature categories (Fig. 4.12F & H; Fig. 4.5H). The other three cases, Rab2, Rab6 and Rab10, were all associated with similar defects in the arrangement of the aECM within the lumen, the Asymmetric Autofluorescence defect category (Fig. 4.13E-H). The defects caused by YRab6-gfpIR and YRab8-gfpIR were highly penetrant. In both cases, almost every TC (88% and 94% of TCs respectively) had at least some branches with the respective characteristic feature. Among the affected YRab8-gfpIR cells, on average 13% of branches were Hairy Branches and among the affected YRab6-gfpIR cells, 37% of branches had Asymmetric Autofluorescence. The Asymmetric Autofluorescence defects caused by YRab2-gfpIR were moderately penetrant, occuring in 38% of cells and 9% to 27% of branches within affected cells. YRab10-gfpIR caused the same defect with a very low penetrance, affecting 23% of cells and only one branch per cell. One TC of the 20 scored YRab8-gfpIR cells also had one branch with aysmmetric autofluorescence.

The features described above are considered defects because they never appeared in control cells. In addition to these, there were also significant differences in the frequency of some features that also appear in controls. The frequency per branch of Wavy Lumens was increased in YRab21-gfpIR (delta: 0.18 per branch; 95% CI: 0.07 to 0.27; p=0.024), as well as YRab6-gfpIR (delta: 0.21; 95% CI: 0.04 to 0.41; p=0.08), YRab39-gfpIR (delta: 0.19; 95% CI: 0.02 to 0.37; p=0.08), YRab2-gfpIR (delta: 0.07; 95% CI: 0.009 to 0.14; p=0.07) and YRab3-gfpIR (delta: 0.09 per branch; 95% CI: 0.01 to 0.18; p=0.052). Conversely, YRab1-gfpIR had a lower frequency of Wavy Lumens than the control (delta: -0.05; 95% CI: -0.10 to 0; p=0.076). Considering that out of the various features, Wavy Branch is the one most frequently observed in controls, and that even with the increased frequencies, the feature's mean penetrance was still below 50% in all cases, these were not further investigated. The frequency of Postjunctional Curls was increased relative to the control frequency of 0.026 per branch in YRab6-gfpIR (delta: 0.15; 95% CI: 0.03 to 0.31; p=0.038), YRab10-gfpIR (delta: 0.07; 95% CI: 0.03 to 0.12; p=0.015) and YRab8-gfpIR (delta: 0.06; 95% CI: 0.02 to 0.10; p=0.040). All three of these samples also showed clear defect phenotypes as described above.

Maternal effect in TC phenotypes

The YRab-gfpIR system makes it possible to test whether mRNA of a *rab* gene is maternally contributed by comparing larvae whose mothers were heterozygous for the YRab allele to those descendent from YRab-homozygous mothers. The larvae themselves need to be YRab-homozygous, as for all YRab-gfpIR experiments. If there is maternal contribution of mRNA and it has a significant effect on the relevant biological processes, the YRab-heterozygous mother will contribute some *rab* mRNA without a YFP tag sequence to be targeted by RNAi. This will lead to a lower RNAi efficiency in her offspring, until the maternal mRNA is degraded naturally. Consequently, defects related to the morphogenetic processes that take place while the maternal product is still present should have a lower severity or penetrance if the mother of YRab-gfpIR larvae had a wildtype *rab* allele. Since the larva itself is YRab-homozygous, the RNAi will affect zygotic mRNA to the same degree regardless of the parental genotype. Any differences between progeny of YRab-heterozygous and YRab-homozygous mothers should therefore exclusively be due to the single copy of maternally contributed untagged *rab* mRNA and/or protein.

Since TC morphogenesis takes place during the larval stages, the YRab-gfpIR system offers an opportunity to test whether the maternally contributed product is maintained until these late stages of development, at least for those four Rabs that were associated with defect phenotypes. However, YRab8-homozygous females were sterile and no YRab-homozygous females hatched for YRab2, YRab6 and YRab10. The phenotypes observed here were found in YRab-homozygous larvae descendent from YRab-heterozygous mothers. The defects therefore occurred despite maternal product, if these Rabs are maternally deposited and the maternal contribution is maintained and involved in larval TC morphogenesis.

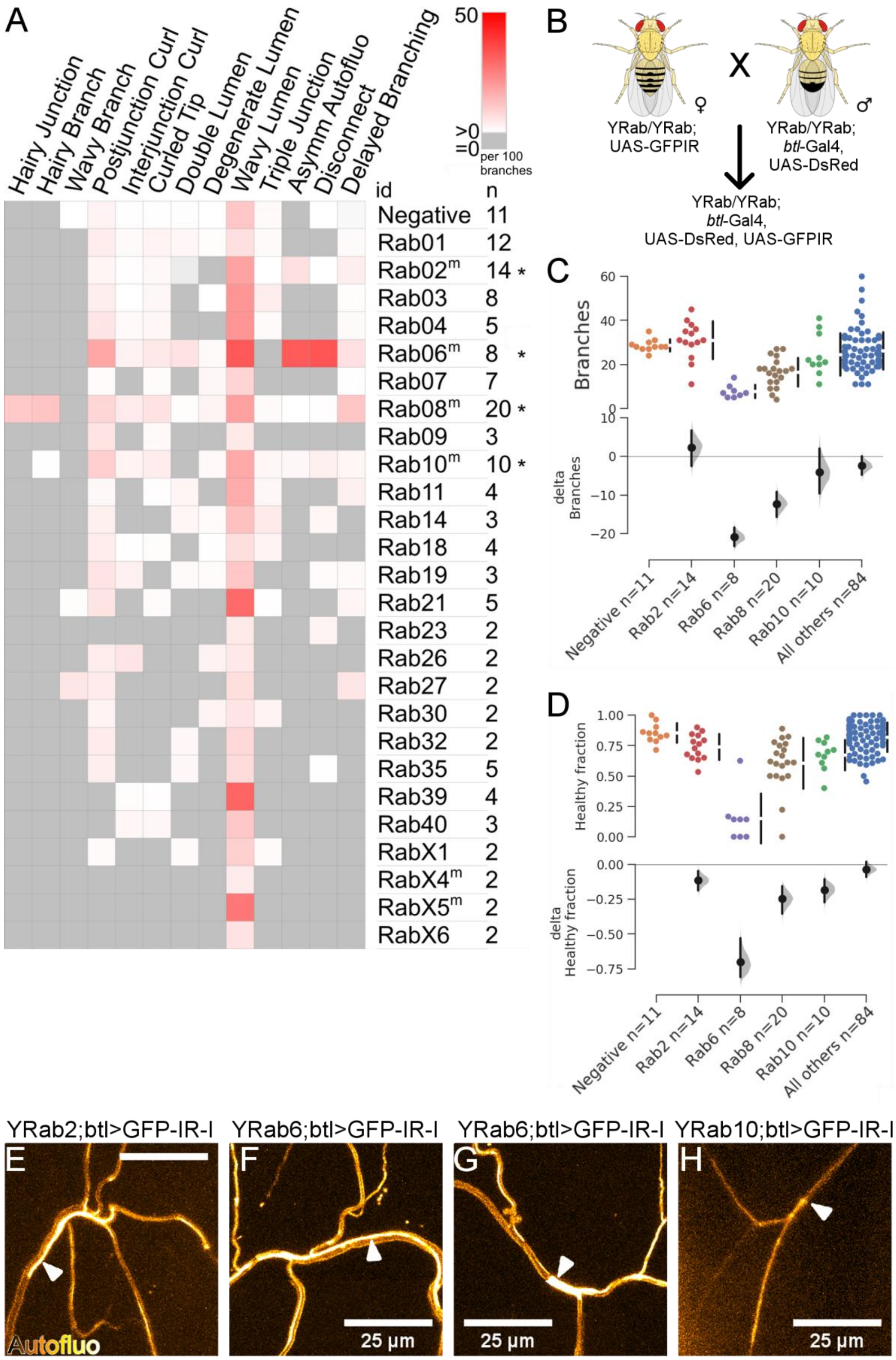
A
Hairy Junction
Hairy Branch
Wavy Branch
Postjunction Curl
Interjunction Curl
Curled Tip
Double Lumen
Degenerate Lumen
Wavy Lumen
Triple Junction
Asymm Autofluo
Disconnect
Delayed Branching
50
>0
=0
per 100 branches
id
n
Negative 11
Rab01 12
Rab02m 14 *
Rab03 8
Rab04 5
Rab06m 8 *
Rab07 7
Rab08m 20 *
Rab09 3
Rab10m 10 *
Rab11 4
Rab14 3
Rab18 4
Rab19 3
Rab21 5
Rab23 2
Rab26 2
Rab27 2
Rab30 2
Rab32 2
Rab35 5
Rab39 4
Rab40 3
RabX1 2
RabX4m 2
RabX5m 2
RabX6 2
B
YRab/YRab; UAS-GFPIR
♀
X
YRab/YRab; btl-Gal4, UAS-DsRed
♂
YRab/YRab; btl-Gal4, UAS-DsRed, UAS-GFPIR
C
Branches
60
40
20
0
delta Branches
10
0
−10
−20
Negative n=11
Rab2 n=14
Rab6 n=8
Rab8 n=20
Rab10 n=10
All others n=84
D
Healthy fraction
1.00
0.75
0.50
0.25
0.00
delta Healthy fraction
0.00
−0.25
−0.50
−0.75
Negative n=11
Rab2 n=14
Rab6 n=8
Rab8 n=20
Rab10 n=10
All others n=84
YRab2;btl>GFP-IR-I
E
Autofluo
YRab6;btl>GFP-IR-I
F
25 µm
YRab6;btl>GFP-IR-I
G
25 µm
YRab10;btl>GFP-IR-I
H
25 µm

Figure 4.13: Phenomic characterisation of terminal cell phenotypes under YRab-gfpIR

(A) Frequencies of morphological features per 100 branches, alternatively percentage of branches showing each feature, since no feature occurred more than once on an individual branch. For reference examples of features see Fig. 4.4. Each square indicates the mean frequency of the respective feature in *n* dorsal terminal cells of heat-fixed third-instar wandering larvae that originated from a YRab-gfpIR cross for the respective Rab. At least 50 cells in at least 5 larvae were screened for each cross. If none of the cells appeared substantially different from controls, only a small number was recorded for quantification. Controls expressed GFP-IR-I and DsRed in all tracheal cells driven by *btl*-Gal4. YRab-gfpIR larvae expressed the same, but additionally had the indicated *rab* gene endogenously tagged with YFP, whose sequence is targeted for degradation by GFP-IR-I. YRab5-gfpIR is absent because larvae were not viable. Scale, grey: zero, white to red: non-zero to 50 average occurrences per 100 branches. m, samples where mothers were heterozygous for the YRab allele - all others had YRab-homozygous mothers. Asterisks, samples with significant loss-of-function phenotypes.

(B) Cross scheme for YRab-gfpIR. YRab-homozygous parents from the respective YRab,IR and YRab,Gal lines are crossed to obtain YRab-gfpIR larvae in which both alleles of the targeted Rab are endogenously YFP-tagged and expression of the GFP-RNAi construct is driven in all tracheal cells by *btl*-Gal4.

(C) Number of branches per terminal cell (top) and estimation of the effect size relative to control (bottom). Each dot represents one terminal cell.

(D) Healthy fraction of each terminal cell (top), i.e. fraction of branches with a stereotypical morphology (showing none of the features in [A]), and estimation of the effect size relative to control (bottom).

(E-H) Examples of the two manifestations of the feature "asymmetric autofluorescence", showing autofluorescence from the apical extracellular matrix of dorsal terminal cells in third-instar wandering larvae. In YRab2-gfpIR (E) and YRab6-gfpIR (F), some cells had a portion of the tube where the autofluorescent matrix accumulated on one side of the tube, forming a longitudinal stripe. In YRab6-gfpIR (G) and YRab10-gfpIR (H), some cells had points along the tube where the autofluorescent matrix filled the entire lumen, usually distally transitioning into a stripe on one side of the tube.

4.2.6 Effects of YRab-gfpIR on dorsal branch morphogenesis

While screening for abnormal phenotypes related to TCs, most observed defects were not related to TC morphology but rather the number and positions of TCs and anastomoses in the dorsal part of the tracheal system, all of which are determined during the morphogenesis of the dorsal branches (DBs). Specifically, the anatomy of the DBs in larvae depends first on the number of cells that invaginate from the tracheal pit and form the bud of the DB during mid-embryogenesis, and subsequently on the fate specification of the two tip cells that lead the migration of the DB towards the dorsal midline during late embryonic development. One of the two cells normally adopts the TC fate and the other the fusion cell fate, subsequent to which they continue migrating and then undergo respectively TC morphogenesis or anastomosis with the contralateral fusion cell. Stereotypically, eight larval segments, beginning with the thoracic segment 2 and up to the abdominal segment 6, each contain two bilateral DBs that fuse at the dorsal midline. Distal and anterior to this fusion point, one TC ramifies on each side (Fig. 4.14A).

Five types of defects were found (Fig. 4.14A'): (1) additional TCs, where the additional TC's stalk was attached either to the DB proximal to the fusion point, on the fusion bridge itself, or on another TC's stalk distal to the fusion point; (2) misguided TCs, growing either posterior to the fusion point into the next segment, anterior into the previous segment, laterally or interior, usually failing to tracheate the stereotypical target muscle; (3) missing TCs; (4) unfused DB pairs; and lastly (5) misfused DBs, where fusion occurred laterally with the DB from the previous or next segment, or diagonally across the midline with a DB from another segment, rather than the contralateral DB of the same segment. The "missing TC" and "unfused DB" defects are different from the rest in that they are limited to a maximum of 8 or 16 occurrences respectively, which are the stereotypical numbers of DB anastomoses and TCs per larva. Additional TCs and missing TCs sometimes both occured in the same larva when some DBs had more than one TC while others had none. All of these defects were observed occassionally in control larvae (Fig. 4.14B, first line) and were also found in wild type strains (data not shown). While additional TCs and unfused DB pairs could be considered common even in controls with on average 1, respectively 0.6 instances per control larva, misguided or missing TCs and misfused DBs were rare events with 0.3 or fewer instances per larva.

I counted these anatomical defects in the entire dorsal tracheal system of at least 6 larvae for each YRab-gfpIR experiment, descendent from at least two sets of parents. The mean frequencies (occurrences per larva) of each anatomical abnormality are shown in Fig. 4.14B. Given that all types of defects occur in wild type and control larvae, the presence of such defects in itself does not provide any information regarding a gene's function. However, defects that occur substantially more frequently in a YRab-gfpIR sample compared to controls are likely to result from the loss-of-function of that Rab. Fig.4.13B' therefore shows the average fold-increase over control frequencies. Black frames in either graphic highlight significant increases, where the lower boundary of the 95% CI is positive and $p<0.05$.

To determine whether any of the anatomical defects are causally connected by underlying biological mechanisms, I analysed correlations between them. The frequencies of additional TCs, missing TCs and unfused DBs were increased in some samples without correlating increases in other defect types, indicating that they can develop independently of other defects. In contrast, misfused DBs were only increased in frequency when unfused DBs were also increased, and misguided TCs appeared more often only when there were also an increased number of additional TCs and unfused DBs. This could suggest some inductive or permissive relationship between these defects, i.e. when one defect happens, another is more likely to occur (inductive) or a defect cannot develop unless first another occurs (permissive). Either of these relationships could result in a numeric correlation between the two defect types, and I therefore performed a pairwise correlation analysis between all defect classes similar to the analysis in the previous chapter (section 4.1.5). However, there were no strong correlations between any of the defects. The correlation coefficient between unfused

DB and misfused DB events was the highest of any pairwise correlation (r=0.55, p<0.0001), but still below a level that would suggest a mechanism where the failure of a fusion event induces a misfusion with another DB. These data therefore provide no evidence of any mechanistic relationship between the defect types.

Rab7 was the only case where YRab-gfpIR caused increases in all five types of abnormalities. This was followed by Rab19, where all defects were increased except for the number of missing TCs. Rabs 32, 35 and 40 each had unique combinations of the different abnormalities. Rabs 27 and 39 both had increased frequencies of unfused DBs and misfused DBs. There were five Rabs that selectively had an increased number of additional TCs (Rabs 4, 11, 14, 23 and 26) and two Rabs with normal anatomy except for an increased number of missing TCs (RabX4 and RabX5). There were mild increases of additional TCs for Rab18, RabX1 and RabX6, as well as missing TCs for Rab32 and unfused DBs for Rab21, which did not meet the default 95% confidence cutoff. However, they would fall within a 90% confidence cutoff. The most penetrant phenotypes were observed for Rab19, RabX5, Rab27 and Rab7. In the case of Rab19, more than 25% of DB pairs failed to fuse, and almost every DB had more than the stereotypical single TC. Unfused DBs were similarly penetrant for Rab7 as for Rab19, although additional TCs were much less frequent for Rab7. In YRabX5-gfpIR, 70% of larvae had at least one missing TC, and many had several, and in YRab27-gfpIR, 71% of larvae had at least one misfused DB pair.

As described in the previous section 4.2.5, the YRab-gfpIR method makes testing maternal contribution of Rabs relatively simple. If a Rab is maternally deposited, YRab-gfpIR larvae descendent from YRab-heterozygous mothers should have a different phenotype from larvae whose mothers were YRab-homozygous. I performed this experiment for YRab7-gfpIR and YRab19-gfpIR since the penetrance of these Rabs' loss-of-function phenotypes was high enough to resolve any potential maternal effect. Most abnormalities occurred similarly often in larvae descendent from YRab-heterozygous mothers and larvae with homozygous mothers. Significant differences were observed only for the frequency of additional TCs in YRab19-gfpIR (Fig. 4.14C; mean 2.4 per larva from YRab-heterozygous mothers vs. 6.5 per larva from YRab-homozygous mothers; delta: 4.1; 95% CI: 2.4 to 5.5; p<0.001) and in the frequency of unfused DBs in YRab7-gfpIR (Fig. 4.14D; mean 0.9 vs. 2.9 per larva; delta: 2.0; 95% CI: 0 to 3.25; p=0.03). Therefore, maternally deposited Rab7 contributes to a functional fusion process, but does not prevent misfusion events or the development of additional TCs. Likewise, maternally deposited Rab19 contributes to development of a normal number of TCs, but does not prevent misfusion events or the failure of fusion events. Both YRab7-gfpIR and YRab19-gfpIR caused increases in several types of defect. Despite this, the maternally contributed product only impacted one type of defect for each of the two Rabs. This is most likely due to different sensitivities of the different processes to a reduction of the amount of the respective Rab protein.

Although none of the observed loss-of-function phenotypes were fully penetrant, these observations implicate many Rabs in tracheal DB morphogenesis for which no involvement was previously known, and provide evidence that maternally deposited *rab7* and *rab19* mRNA persist throughout embryogenesis in tracheal cells. This morphogenetic process should be of particular interest for determining the functions of Rab19 and RabX5, for which little data are available in any biological system.

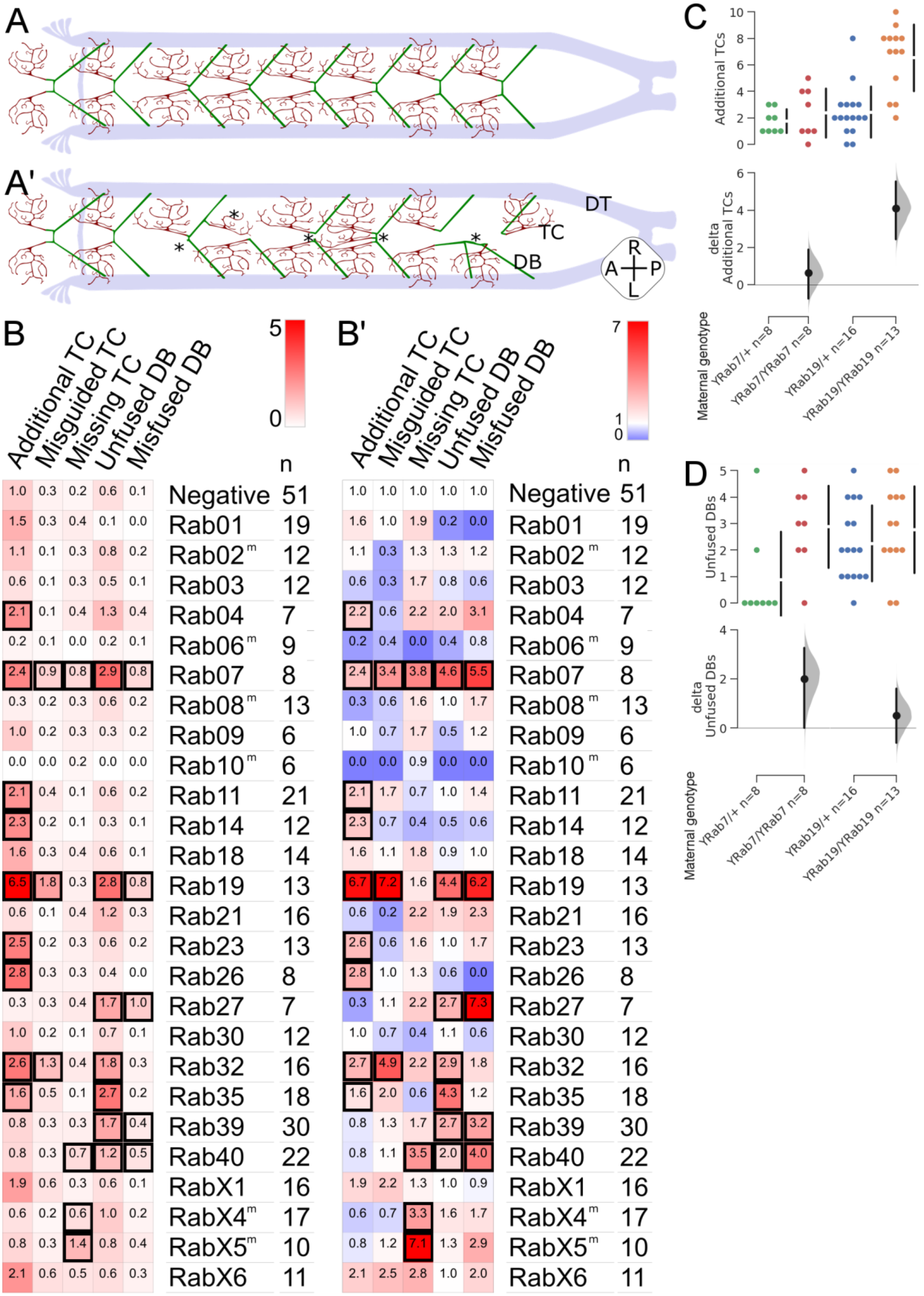

B

Additional TC	Misguided TC	Missing TC	Unfused DB	Misfused DB		n
1.0	0.3	0.2	0.6	0.1	Negative	51
1.5	0.3	0.4	0.1	0.0	Rab01	19
1.1	0.1	0.3	0.8	0.2	Rab02^{m}	12
0.6	0.1	0.3	0.5	0.1	Rab03	12
2.1	0.1	0.4	1.3	0.4	Rab04	7
0.2	0.1	0.0	0.2	0.1	Rab06^{m}	9
2.4	0.9	0.8	2.9	0.8	Rab07	8
0.3	0.2	0.3	0.6	0.2	Rab08^{m}	13
1.0	0.2	0.3	0.3	0.2	Rab09	6
0.0	0.0	0.2	0.0	0.0	Rab10^{m}	6
2.1	0.4	0.1	0.6	0.2	Rab11	21
2.3	0.2	0.1	0.3	0.1	Rab14	12
1.6	0.3	0.4	0.6	0.1	Rab18	14
6.5	1.8	0.3	2.8	0.8	Rab19	13
0.6	0.1	0.4	1.2	0.3	Rab21	16
2.5	0.2	0.3	0.6	0.2	Rab23	13
2.8	0.3	0.3	0.4	0.0	Rab26	8
0.3	0.3	0.4	1.7	1.0	Rab27	7
1.0	0.2	0.1	0.7	0.1	Rab30	12
2.6	1.3	0.4	1.8	0.3	Rab32	16
1.6	0.5	0.1	2.7	0.2	Rab35	18
0.8	0.3	0.3	1.7	0.4	Rab39	30
0.8	0.3	0.7	1.2	0.5	Rab40	22
1.9	0.6	0.3	0.6	0.1	RabX1	16
0.6	0.2	0.6	1.0	0.2	RabX4^{m}	17
0.8	0.3	1.4	0.8	0.4	RabX5^{m}	10
2.1	0.6	0.5	0.6	0.3	RabX6	11

B'

Additional TC	Misguided TC	Missing TC	Unfused DB	Misfused DB		n
1.0	1.0	1.0	1.0	1.0	Negative	51
1.6	1.0	1.9	0.2	0.0	Rab01	19
1.1	0.3	1.3	1.3	1.2	Rab02^{m}	12
0.6	0.3	1.7	0.8	0.6	Rab03	12
2.2	0.6	2.2	2.0	3.1	Rab04	7
0.2	0.4	0.0	0.4	0.8	Rab06^{m}	9
2.4	3.4	3.8	4.6	5.5	Rab07	8
0.3	0.6	1.6	1.0	1.7	Rab08^{m}	13
1.0	0.7	1.7	0.5	1.2	Rab09	6
0.0	0.0	0.9	0.0	0.0	Rab10^{m}	6
2.1	1.7	0.7	1.0	1.4	Rab11	21
2.3	0.7	0.4	0.5	0.6	Rab14	12
1.6	1.1	1.8	0.9	1.0	Rab18	14
6.7	7.2	1.6	4.4	6.2	Rab19	13
0.6	0.2	2.2	1.9	2.3	Rab21	16
2.6	0.6	1.6	1.0	1.7	Rab23	13
2.8	1.0	1.3	0.6	0.0	Rab26	8
0.3	1.1	2.2	2.7	7.3	Rab27	7
1.0	0.7	0.4	1.1	0.6	Rab30	12
2.7	4.9	2.2	2.9	1.8	Rab32	16
1.6	2.0	0.6	4.3	1.2	Rab35	18
0.8	1.3	1.7	2.7	3.2	Rab39	30
0.8	1.1	3.5	2.0	4.0	Rab40	22
1.9	2.2	1.3	1.0	0.9	RabX1	16
0.6	0.7	3.3	1.6	1.7	RabX4^{m}	17
0.8	1.2	7.1	1.3	2.9	RabX5^{m}	10
2.1	2.5	2.8	1.0	2.0	RabX6	11

Figure 4.14: Defects in dorsal branch anatomy under YRab-gfpIR
(A) Dorsal view of the larval tracheal system's stereotypical anatomy. The dorsal trunks (DT, purple) are the main tracheal tubes and connect to the atmosphere. From these, eight bilateral pairs of dorsal branches (DBs, green) migrate towards the dorsal midline during embryogenesis. Of the two leading DB tip cells, one adopts the terminal cell (TC, red) fate and the other becomes a fusion cell that forms a connection with the fusion cell of the contralateral DB.
(A') Illustration of observed defects in the dorsal tracheal anatomy. Asterisks indicate defects (left-to-right): Missing TC, misguided TC, unfused DB, additional TC, misfused DB.
(B) Mean frequency of each defect per larva in *n* scored YRab-gfpIR larvae where the indicated Rab is endogenously tagged with YFP. Negative controls expressed GFP-IR-I and DsRed in all tracheal cells driven by *btl*-Gal4. YRab5-gfpIR is absent because larvae were not viable. Scale, white to red: 0 to 5 average occurrences per larva. Black frames, significant differences to control (lower boundary of 95% CI > 0 and p<0.05). m, samples where mothers were heterozygous for the YRab allele - all others had YRab-homozygous mothers.
(B') Relative frequencies of each defect compared to negative control, i.e. ratio of mean frequency per larva in the indicated YRab-gfpIR sample to the mean frequency in the negative control. Underlying data is displayed in (B). Scale, blue to white: 0 to 1, white to red: 1 to 7 times control frequency.
(C) Test for maternal effect on the frequency of additional TCs in YRab-gfpIR samples for Rab7 and Rab19. Each dot in the upper plot represents the frequency of additional TCs in one larva descendent from either a YRab-heterozygous (YRab/+) or YRab-homozygous mother (YRab/YRab). The larvae themselves were YRab-homozygous and expressed GFP-IR-I and DsRed in all tracheal cells driven by *btl*-Gal4.
(D) Test for maternal effect on the frequency of unfused DBs in the larvae represented in (C).

4.2.7 Controls for negative results

Several Rabs are reported to play important roles in membrane trafficking, and I therefore expected severe loss-of-function defects related to these Rabs in TC morphogenesis. Specifically, the functions of Rab1, Rab7 and Rab11 are conserved throughout evolution and central to many biological processes in a variety of cell types (Dunst et al., 2015). All three are expressed at high levels by TCs as evidenced by YRab detectability, and a previous study reported a tube defect with RNAi against Rab11 (Jones et al., 2014). Rab4 and Rab35, while not detectable in TCs when endogenously tagged with YFP, are similarly important proteins for many cell types (Stenmark, 2009). The small number of Rabs that caused defects in TCs in the YRab-gfpIR screen was therefore surprising, and deserved further investigation. There are two intuitive (and not mutually exclusive) explanations for the negative results of this screen: First, the YFP-mediated knockdown by a GFP-RNAi construct may be too weak to significantly impact the membrane trafficking systems a Rab is involved in, even though the validation experiments demonstrated that the YRab protein becomes undetectable (sections 4.2.2 and 4.2.4). I addressed this possibility using the established Mosaic Analysis with a Repressible Cell Marker (MARCM) technique (Lee and Luo, 2001) to induce *rab* mutant TCs in larvae that are otherwise heterozygous for a wildtype allele. The second explanation is genetic redundancy. Some *rab* genes' mRNA or protein products might be involved in regulatory feedback loops, and eliminating them might upregulate expression of other genes to compensate. Although no instance of this type of relationship between Rabs is known, the promiscuity of many Rab GEFs, effectors and GAPs could allow such redundancy of functionally related Rabs. This possibility was addressed by performing YRab-gfpIR targeting two Rabs simultaneously. Three pairs of Rabs that could reasonably be expected to compensate for each other's functions were tested.

Rab *mutant terminal cells using MARCM*

Rab1^{S147213} (Sechi et al., 2017), *rab7*^{d1} (Hegedűs et al., 2016), and *rab11*^{j2D1} (Chen et al., 2005) are validated null alleles of the respective *rab* genes. Homozygous mutant larvae were not viable for any of the three. Therefore, I used MARCM to observe phenotypes of zygotic *rab* mutant TCs, a genetic system designed to circumvent homozygous mutant lethality. The MARCM system is based on the recombinase Flippase (Flp) and Flippase recognition target (FRT) sites, mediating recombination of mutant-bearing chromosome arms with wildtype homologue arms in mitotic cells of a heterozygous animal. This is combined with Gal4-mediated expression of a fluorescent marker and a Gal4-repressor inserted in *cis* to the wildtype allele (Fig.4.15A-B'). The marker-expressing cells are therefore zygotic homozygous mutants that inherit not only maternally contributed gene products but also those expressed by their parental cell prior to recombination. I generated the required *Drosophila* strains and adapted the protocol such that the recombination efficiency was low enough to obtain individual TCs carrying homozygous mutations in the *rab1*, *rab7* or *rab11* gene.

Rab1 mutant TCs had a uniform loss-of-function phenotype (Fig. 4.15B), forming at most 4 branches and revealing tube defects reminiscent of the asymmetric autofluorescence seen in YRab-gfpIR against Rab6, Rab2 and Rab10. The phenotypes of *rab7* and *rab11* mutant TCs were variable, but always clearly distinguishable from wildtype cells. Four types of defects were prominent in these cells. Of these, three were consistent with previously identified morphological features: Asymmetric Autofluorescence, Disconnect, and Curled Tips. A small fraction of *rab7* (1 out of 9) and *rab11* (4 out of 30) mutant TCs displayed a type of defect not previously associated with any Rab. In these cells, some branches contained between two and nine tubes running parallel to each other. This phenotype was reminiscent of the tube bundles observed in *talin* mutant TCs (Levi et al., 2006) and would be considered Delayed Branching or Double Lumen according to the phenomic feature classes.

The mutant TCs of all three Rabs could be categorised into five classes depending on branch number and severity of the defects. TCs in class 1 ("near-wildtype") had a normal number of branches as well as tube and aECM morphology, except for one stretch of tube where the autofluorescence was asymmetric and/or one stretch where the tube was disconnected (Fig. 4.15C). TCs in class 2 had normal or slightly reduced numbers of branches, and most of the total length of tubes had asymmetric autofluorescence (Fig. 4.15D). TCs in class 3 had a substantially reduced branch count, with most of the autofluorescence being asymmetric and additional presence of disconnects or curled tips (Fig. 4.15E). TCs in class 4 had severely reduced branch numbers (below 6), subdivided by aECM morphology into those with normal autofluorescence (class 4-1; Fig. 4.15F), those with asymmetric autofluorescence (class 4-2; Fig. 4.15F') and those with long stretches of no autofluorescence (disconnect) and asymmetric autofluorescence where visible (class 4-3; Fig. 4.15F"). TCs in class 5 were degenerate, i.e. unbranched, and had asymmetric autofluorescence in the remaining stalk (Fig. 4.15G).

TCs with a *rab1* mutation consistently fell into class 4 (Fig. 4.16A), while TCs with *rab7* mutations were evenly distributed across classes 1 to 4. *Rab11* mutant TCs most often formed less than 6 branches and therefore fell into class 4, but there were also many cells with a only mild defects. The ranges of phenotypic variability associated with these *rab* mutants were therefore different, but the types of defects were similar in all three. All TCs with mutations in one of the three Rabs were clearly distinguishable from wildtype TCs. In contrast, TCs from YRab-gfpIR experiments targeting YRab1, YRab7 and YRab11 never had any of the defects observed in mutant TCs and also showed no other abnormalities. As discussed later, there are potential confounding factors in the MARCM method that could contribute to the phenotypes observed. Given the severity of the defects, these results nevertheless indicate that the loss-of-function induced by the YRab-gfpIR method targeting YRab1, YRab7 and YRab11 is milder than a null mutation in the corresponding *rab* gene. Yet, the previous tests showed that YRab-gfpIR reduces the expression of YRab1 protein to undetectable levels (section 4.2.2, Fig. 4.11 and section 4.2.4, Fig. 4.12). This suggests that the TCs observed in the YRab1-, YRab7- and YRab11-gfpIR experiments expressed an undetectable residual amount of YRab protein that was sufficient to provide normal function to the cell. Consequently, it is also possible for other YRabs that the indirect RNAi approach used here does not induce loss-of-function at an efficiency required to manifest the Rab's associated phenotypic defects.

Combined YRab-gfpIR against pairs of Rabs

To test the hypothesis that a functionally related Rab could compensate for the loss of another Rab's function, I generated additional *Drosophila* lines carrying the endogenous YFP-tag on two Rabs. As before, the YRab-gfpIR experiment was carried out by crossing two lines for each combination of Rabs. One line carried the *btl*-Gal4 construct and the two YRab alleles, and the other carried the GFP-IR-I construct and the same YRab alleles. I tested the following combinations of YRabs:

- Rab10 and Rab11, since one publication suggests they function redundantly in TCs (Jones et al., 2014)
- Rab11 and Rab35, based on a collaborator's suggestion (M. Brankatschk, personal communication)
- Rab4 and Rab11 as these are both associated with recycling endocytosed material back to the plasma membrane (Mizuno-Yamasaki et al., 2012)

As previously, I carried out the double YRab-gfpIR experiments by crossing the two corresponding lines at 29°C, using mothers that were homozygous for both *yrab* alleles (except for YRab10/YRab11 because YRab10-homozygous females were infertile). As before, I collected third-instar wandering larvae and screened their dorsal TCs for abnormalities in the tube morphology or aECM as reflected by its autofluorescence. Subsequently, I confirmed the genotype of the collected larvae by PCR.

The vast majority of TCs in all samples had a normal phenotype (Fig.4.16B), with occassional occurences of morphological features such as Wavy Lumen or Curled Tip. These features also occur in wildtype and control TCs, and were never found in frequencies that could be considered abnormal during these double YRab-gfpIR experiments. However, a small fraction of TCs had asymmetric autofluorescence along a portion of their tube in the combined YRab-gfpIR targeting Rab4 and Rab11, as well as the combination of Rab11 and Rab35, but not when targeting Rab10 and Rab11. These observations are analogous to synergistic epistasis with respect to asymmetric autofluorescence, whereby none of the individual YRab-gfpIR experiments caused this defect but YRab-gfpIR against combinations of Rab4, Rab11 and Rab35 did. Surprisingly, the combination of YRab10 and YRab11 did not produce any cells with asymmetric autofluorescence, even though YRab10-gfpIR on its own did.

The observations made for Rab4, Rab11 and Rab35 are consistent with functional redundancy with respect to the asymmetric autofluorescence defect and therefore support my hypothesis that functionally related Rabs can compensate for one another. However, it is not possible to infer the molecular basis of redundancy based on these experiments alone. Besides a feedback mechanism upregulating other Rabs' expression levels, a probable explanation for these results could be that all three Rabs are involved in trafficking of the same cargo molecule, which is delivered via other trafficking routes when one route is defective. The unexpected observations for the combination of Rab10 and Rab11 suggest that the molecular pathway that causes asymmetric autofluroescence involves some inhibitory interaction. However, it is not possible to infer at which level or in which direction inhibition takes place, because RNAi does not induce a full loss-of-function and therefore allows for multiple possible configurations of the interaction.

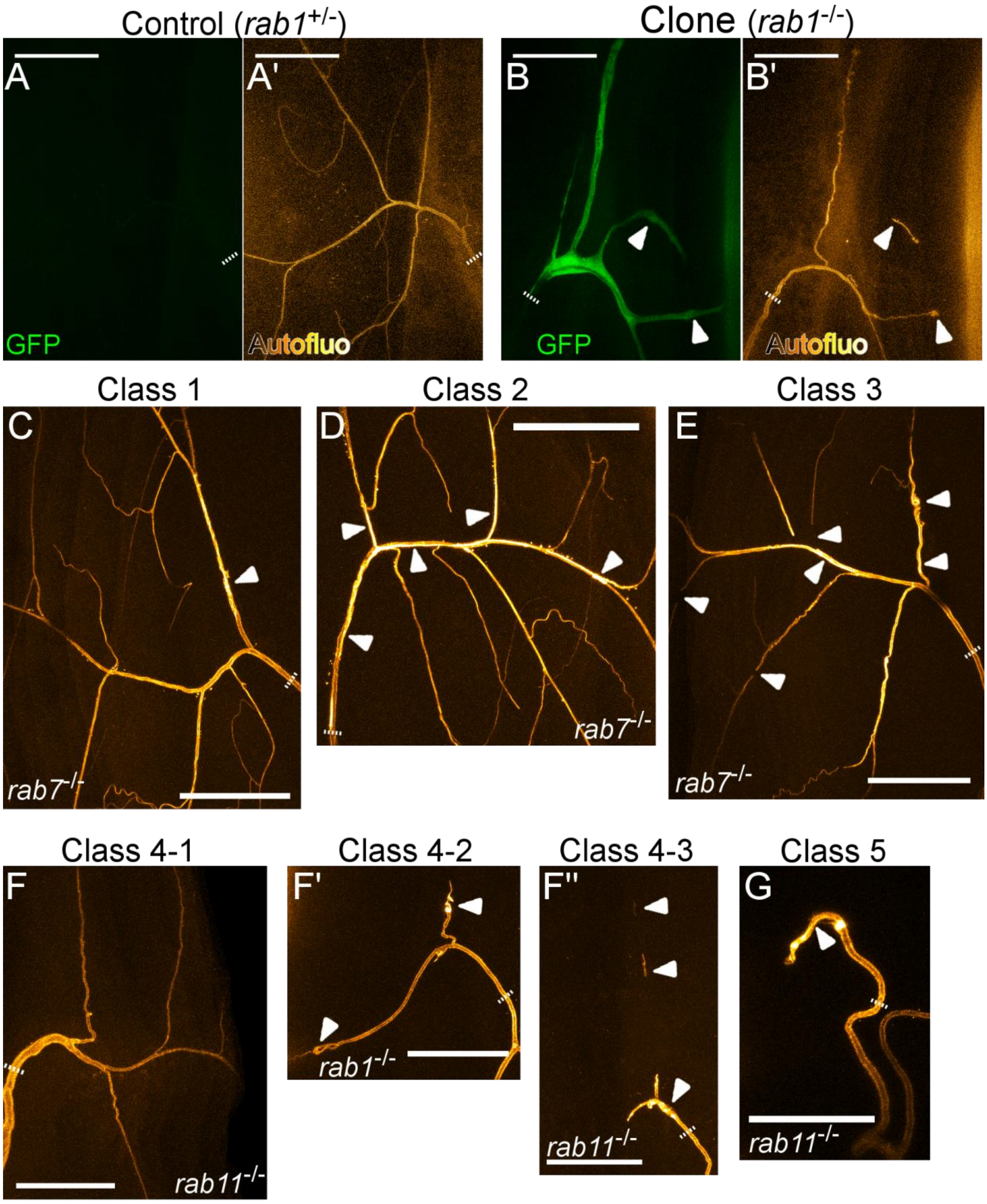

Figure 4.15: *Rab* mutant terminal cell clones obtained using MARCM
Examples of *rab* mutant terminal cell clones of the various defect severity classes. Images represent z-projected optical stacks of varying depth. Dotted lines, beginning of terminal cell stalk. Arrowheads, tube defects: disconnected tube portions, curled tube tips and asymmetric autofluorescence. Scale bars, 50µm.
(A-A') Micrograph of a negative control dorsal terminal cell in a heat-fixed third-instar wandering *rab1*$^{S147213/+}$ MARCM larva. GFP was driven by *btl*-Gal4 and the chromosome with a wildtype *rab1* allele carried the Gal4-repressor Gal80 under control of the *tubulin* promoter.

(B-B') Micrograph of a positive terminal cell clone reporting the lack of Gal80 and therefore *rab1*^{S147213} homozygosity by expressing Gal4-driven GFP. This terminal cell was the contralateral neighbour of the cell in (A).

(C-G) Mutant terminal cell clones of the indicated *rab* gene obtained using MARCM. Representative examples of the five classes of defect severity identified across *rab1*, *rab7* and *rab11* mutant TCs. Quantification in Fig.4.15.

(C) Class 1 ("near-wildtype"): normal number of branches as well as tube and aECM morphology, except for one stretch of tube where the autofluorescence was asymmetric and/or one stretch where the tube was disconnected.

(D) Class 2: normal or slightly reduced number of branches: most of the tube network has asymmetric autofluorescence.

(E) Class 3: approximately halved branch count, with most of the autofluorescence being asymmetric and additional presence of disconnects or curled tips.

(F-F'') Class 4: severely reduced branch numbers (up to 5), subdivided by aECM quality; (F) Class 4-1: normal autofluorescence, (F') Class 4-2: asymmetric autofluorescence, (F'') Class 4-3: disconnected pieces of tube with large distances and asymmetric autofluorescence.

(G) Class 5 ("degenerate"): unbranched, asymmetric autofluorescence in the remaining stalk.

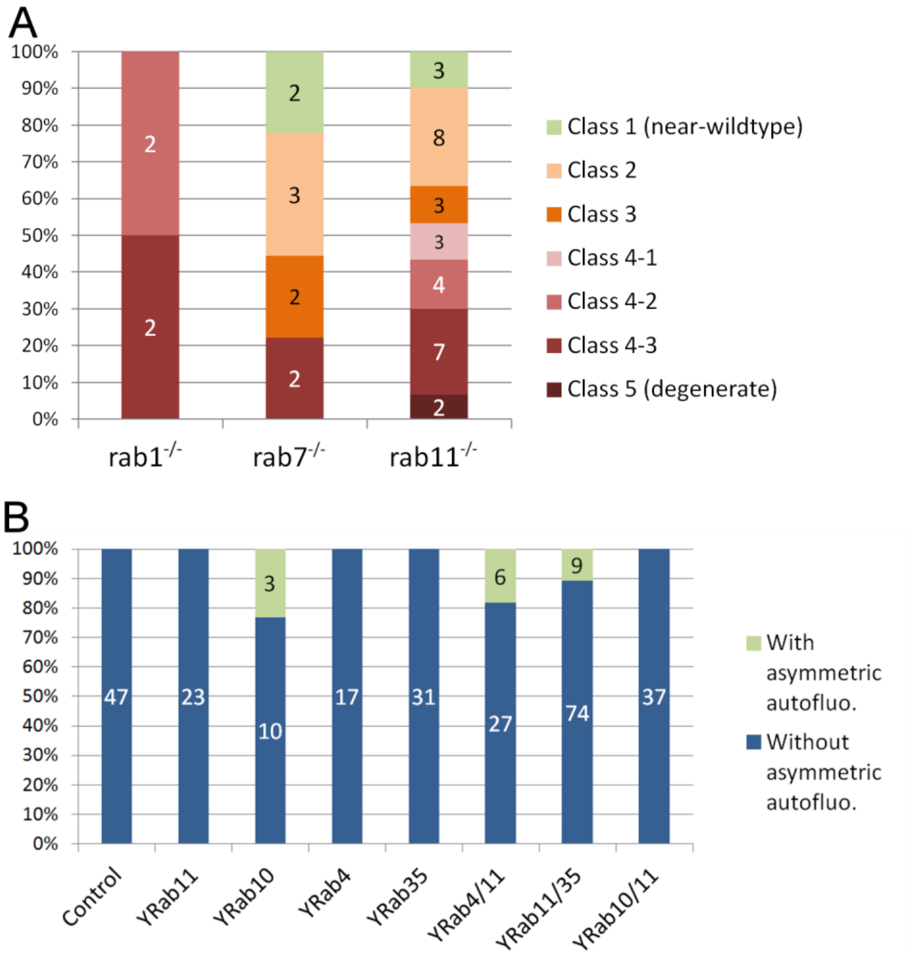

Figure 4.16: Quantification of *rab* mutant phenotypes and YRab-gfpIR targeting pairs of Rabs

(A) Number of *rab* mutant terminal cell clones of each phenotype severity class found in *rab* MARCM larvae. Examples of each class are in Fig.4.15.

(B) Number of YRab-gfpIR terminal cells showing asymmetric autofluorescence anywhere along their subcellular tube. Control larvae expressed GFP-IR-I and DsRed in all tracheal cells driven by *btl*-Gal4. YRab-gfpIR larvae expressed the same and additionally had both copies of the indicated Rabs endogenously YFP-tagged.

4.3 Rab8-mediated control of tube shape

The YRab-gfpIR screen and the complementary experiments revealed many Rab proteins to be necessary for proper morphogenesis of the tracheal dorsal branch, and the following eight Rabs to be necessary for proper terminal cell (TC) morphogenesis: Rab1, Rab2, Rab4, Rab6, Rab7, Rab8, Rab10 and Rab11. Additionally, Rab4 and Rab35 were implicated as functional interaction partners of Rab11. Strikingly, all Rabs were associated with only two distinct types of morphological defects that are reflected by the autofluorescent apical extracellular matrix (aECM), which lines the interior of the subcellular tube. The first defect manifests as a "hairy" appearance of the tube, caused by additional tubules that branch off the main tube and wrap around it. The aECM within the main and additional tubes appears normally organised. This defect was associated with Rab8, and previously appeared in a similar form during the phenomic study with specific RNAi against Rab5. All other Rabs were associated with the second type of defect, in which the tube shape appears mostly normal, but the autofluorescence of the aECM is asymmetric, indicating a disorganised aECM.

For my further work, I focussed on Rab8 because its phenotype suggests that it is involved in the determination of apical membrane shape. It is also poorly characterised in *Drosophila* as of yet, and in other model systems has been found to interact with different and unrelated trafficking routes in different contexts. My main aim was to pinpoint the trafficking pathway and the endomembrane compartment on which Rab8 performs its function in TCs. Considering the phenotype caused by Rab8 loss-of-function, this part of the trafficking machinery should be associated with apical membrane shape. Following this, I attempted to identify a cargo protein whose trafficking involves Rab8.

4.3.1 Rab8 function depends on Rab6

Rabs are involved in all steps of the endomembrane trafficking system. For protein trafficking, the highest-level candidates where Rab8 could act are: 1) at the endoplasmatic reticulum (ER), in which case its function could impact the entirety of the cell's membrane and secreted protein synthetis system; 2) at the Golgi apparatus, in which case its function would likely impact secretion pathways in particular; 3) the endosomal systems, which would allow for a variety of specific functions such as polarised secretion, endocytosis, as well as sorting and recycling of endocytosed material. To identify which of these Rab8 is associated with, I took advantage of the defect phenotype identified for Rab6 in the preceding screen. Perhaps the most significant advantage of YRab-gfpIR is the confidence that identified defects are true positives. Rab6 was a good candidate since YRab6-gfpIR caused defective terminal cell (TC) morphogenesis with high penetrance, and Rab6 performs a highly conserved function across the eukaryotic kingdom (Liu and Storrie, 2015). Its associated defect phenotype is also consistent with its conserved role in maintaining Golgi integrity and thereby upkeeping the secretory system (see Discussion). Rab6 is therefore suitable as a reference point, and by investigating its functional relationship to Rab8, it should be possible to identify whether Rab8 functions upstream (probably ER), parallel (probably Golgi) or downstream (probably endosomal system) of it.

I screened publicly available *Drosophila* lines carrying RNAi constructs against Rab6 and identified a line that reproduced the defects found in YRab6-gfpIR (Fig. 4.17B). The identified construct will be referred to as Rab6-IR. Expression of Rab6-IR under *btl*-Gal4 caused asymmetric aufluorescence as observed in YRab6-gfpIR in all dorsal TCs (Fig. 4.17G). 60% of cells additionally had discontinuities in their autofluorescence, resulting in disconnected fragments (Fig. 4.17H). Similar to YRab6-gfpIR, the number of branches formed by TCs was drastically reduced (Fig. 4.17E).

To test whether *rab6* and *rab8* interact, I induced TCs to co-express RNAi constructs against both and compared the resulting phenotypes to those resulting from expression of the individual constructs. I also attempted to reproduce the results by generating double YRab-gfpIR larvae in which both YRab6 and YRab8 are targeted by GFP-IR-I, but larvae of the appropriate genotype did not survive past the L2 stage. TCs expressing both Rab6-IR and Rab8-IR qulitatively had very similar phenotypes as TCs expressing only Rab6-IR (compare Fig. 4.17D to B and C). The number of branches was much lower than in individual Rab8-IR expression, but slightly higher than in the Rab6-IR sample (Fig. 4.17F; mean delta: 1.8; 95% CI: 0.3 to 3.6; p=0.10). When comparing the penetrance of the individual phenotypic features that characterise Rab6-IR and Rab8-IR, a consistent picture emerges (Fig. 4.17G-J). The percentage of Rab6-IR and Rab8-IR co-expressing TCs that displayed each feature was always more similar to the Rab6-IR sample. Overall therefore, the defects that Rab8-IR normally induces are suppressed by co-expression of Rab6-IR. This is consistent with a model where Rab8 functions downstream of Rab6, suggesting that Rab8 is involved in endosomal trafficking and its function depends on a functioning Golgi apparatus.

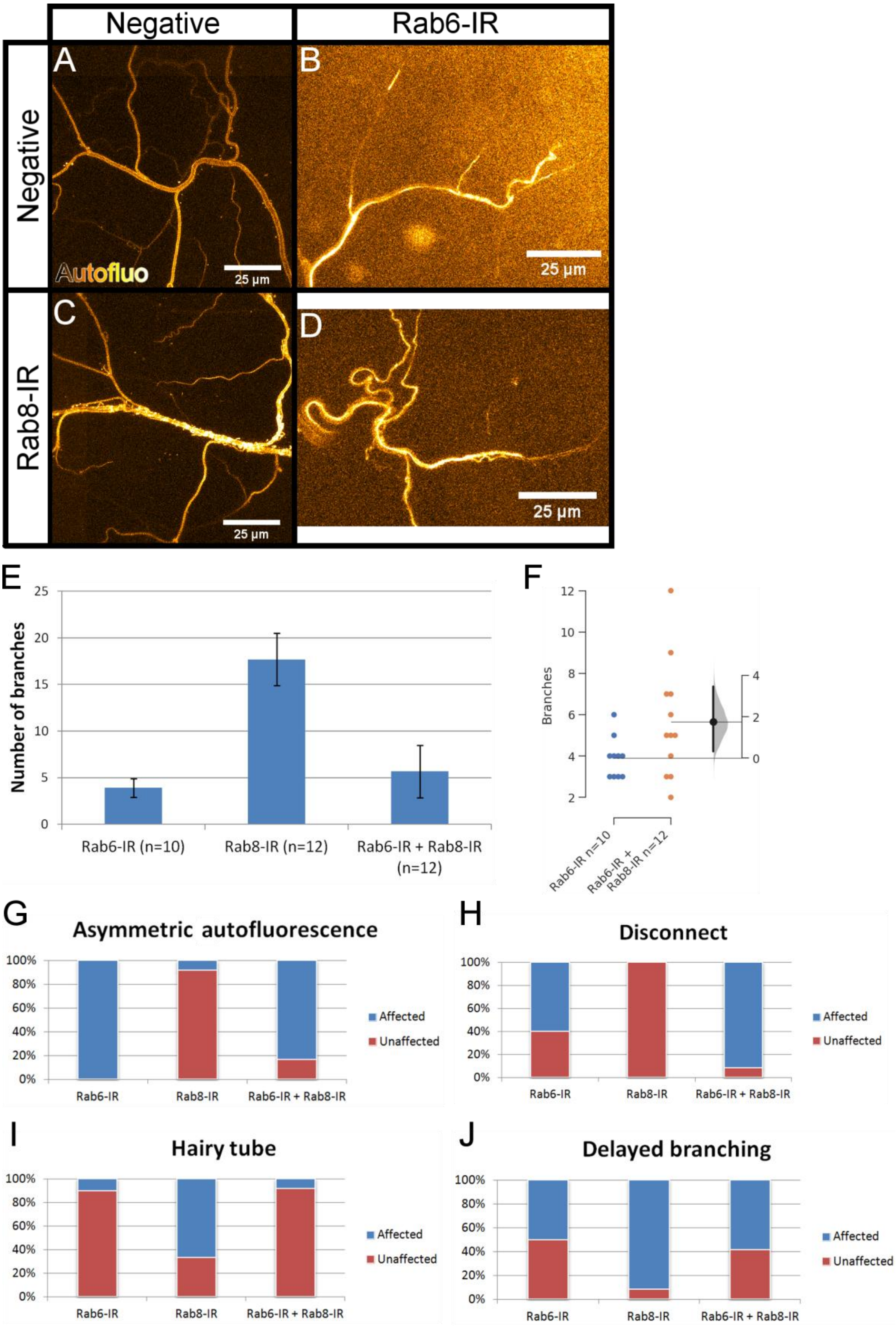
Negative
Rab6-IR
Negative
Rab8-IR
A
B
C
D
Autofluo
25 µm
25 µm
25 µm
25 µm
E
Number of branches
25
20
15
10
5
0
Rab6-IR (n=10)
Rab8-IR (n=12)
Rab6-IR + Rab8-IR (n=12)
F
Branches
12
10
8
6
4
2
4
2
0
Rab6-IR n=10
Rab6-IR + Rab8-IR n=12
G
Asymmetric autofluorescence
H
Disconnect
I
Hairy tube
J
Delayed branching
100%
80%
60%
40%
20%
0%
Rab6-IR
Rab8-IR
Rab6-IR + Rab8-IR
Affected
Unaffected

Figure 4.17: Epistasis of Rab6 and Rab8 in subcellular tube morphogenesis
The genetic interaction between Rab6 and Rab8 with respect to the morphology of the terminal cell tube or the autofluroescent apical extracellular matrix was tested using RNAi constructs against *rab6* and *rab8*. Animals expressing Rab8-IR were siblings of the respective counterpart not expressing it and were identified by the absence of a marked balancer chromosome.
(A-D) Z-projected optical stacks showing apical extracellular matrix autofluorescence of dorsal terminal cells in heat-fixed third-instar larvae.
(A) Terminal cell in a larva expressing DsRed in all tracheal cells. Sibling of the larva in (C).
(B) Terminal cell in a larva expressing DsRed and Rab6-IR in all tracheal cells. Branching is severely reduced and the apical extracellular matrix is abnormal in that it is asymmetric and sometimes pieces are disconnected from the rest. Sibling of the larva in (D).
(C) Terminal cell in a larva expressing DsRed and Rab8-IR in all tracheal cells. The tube is enveloped by a multitude of smaller tubules ("Hairy tube").
(D) Terminal cell in a larva expressing DsRed, Rab6-IR and Rab8-IR. As in (B), branching is severely reduced and the autofluorescence of the apical extracellular matrix is asymmetric and sometimes disconnected.
(E) Quantification of branch numbers in RNAi-expressing larvae. Error bars show standard deviation.
(F) Estimation of the impact of Rab8-IR on branch numbers of terminal cells expressing Rab6-IR. Each dot represents one terminal cell. Data are the same as in (E).
(G-J) Penetrance of the defects visible in (A-D) in the same cells as quantified in (E). Each bar shows the percentage of cells which showed the respective defect anywhere along their tube network.

4.3.2 Subcellular localisation and dynamics of Rab8

If Rab8 indeed functions post-Golgi in the endosomal trafficking system, it could be possible to identify which endosomal compartment(s) it is associated with based on its subcellular localisation. To test this, I used a transgenic line generated by S. Sigurbjörnsdottir in the lab, with an insertion of a UAS-inducible RFP-tagged Rab8 (RFP.Rab8). I generated larvae that express tagRFP.Rab8 driven by *btl*-Gal4 and simultaneously have an endogenously YFP-tagged marker Rab (YRab). The YRabs used were Rab1, a marker for pre-Golgi intermediate compartments (Charng et al., 2014); Rab6, a marker for *trans*-Golgi compartments and Golgi-derived vesicles (Liu and Storrie, 2015; Sandoval and Simmen, 2012); Rab7, a marker for late endosomes and lysosomes (Stenmark, 2009); or Rab11, a marker for endosomal recycling compartments (Zerial and McBride, 2001).

In TCs of heat-fixed larvae, RFP.Rab8 and all four YRabs had a punctate distribution in the cytoplasm. To assess the degree of overlap between Rab8 and each marker Rab, I therefore segmented punctate structures in the RFP and the YFP channel and then determined the fraction of Rab8 puncta that coincided with puncta of the respective marker Rabs (Fig. 4.18A). Rab8 puncta where at least 1% of their area was also positive for the marker Rab were considered partially overlapped, and Rab8 puncta where at least 90% of their area was shared with the marker Rab were considered fully overlapped. Rab1 and Rab6 had similar patterns of overlap with Rab8, labelling 24-50% of Rab8-enriched structures (Fig. 4.18A & B). A substantial fraction of these structures only partially overlapped with the respective YRab signal, 30-67% in case of Rab1 and 14-30% in case of Rab6. Rab7 showed very little overlap with Rab8, labelling only a small fraction of Rab8 puncta (Fig.4.18C). By far the largest overlap was observed with Rab11 (Fig.4.18D), which colocalised with 31-82% of Rab8 puncta, and fully overlapped with almost all of these (0-25% partially overlapped).

These results suggest that Rab8-enriched structures are predominantly recycling endosomes, although a substantial fractions of Rab8 structures are Golgi-associated membranes. The predominant localisation on endosomal membranes is consistent with a function downstream of the Golgi apparatus as suggested by the previous RNAi experiment.

The large variability of the overlap with marker Rabs suggested that Rab8 is a dynamic protein, with large amounts of the total Rab8 pool shifting between different membrane compartments. I attempted to corroborate this result by observing the subcellular dynamics of Rab8 in live larval terminal cells. Live-imaging of *Drosophila* larvae at high spatial resolution presents a notorious challenge of proper anaesthesia and published protocols did not lead to the same results as published. Despite this, I succeeded in obtaining live captures of *btl*-Gal4 driven overexpressed RFP-tagged Rab8 in third-instar larvae.

Most Rab8-enriched structures appeared static across large time spans (~30min). Some smaller Rab8 puncta, presumably vesicles, were found moving along branches at velocities of approximately 300nm/s , but I was not able to capture enough of these to identify patterns among their movement. Most intriguingly, in some TCs (n=3) I identified a large dynamic Rab8-enriched structure spanning approximately 1.4µm in the apicobasal axis around 3µm longitudinally, usually residing near the tube or roughly centred between tube and basal membrane. I observed what appeared to be approximately 300nm thick tubules extending from these structures and then receding back into them, sometimes making contact with the tube in the process. These projections reached lengths between 1µm (Fig.4.18B) and 5µm (Fig.4.18C) and were sometimes observed extending, partially retracting, and then extending into a different direction before fully receding. Of note, I never observed such a tubule projecting towards, or contacting, the basal membrane across a total observation time of such structures of 1h30min in three different cells. At times, the structures appeared to partially fuse with a pool of Rab8 located at the tube (Fig. 4.19D), remaining merged with it for approximately 10s before separating again.

Overexpressed tagged Rab8 protein thus appears to exhibit a preference for enriching at structures near the apical membrane, or structures that interact with the apical membrane.

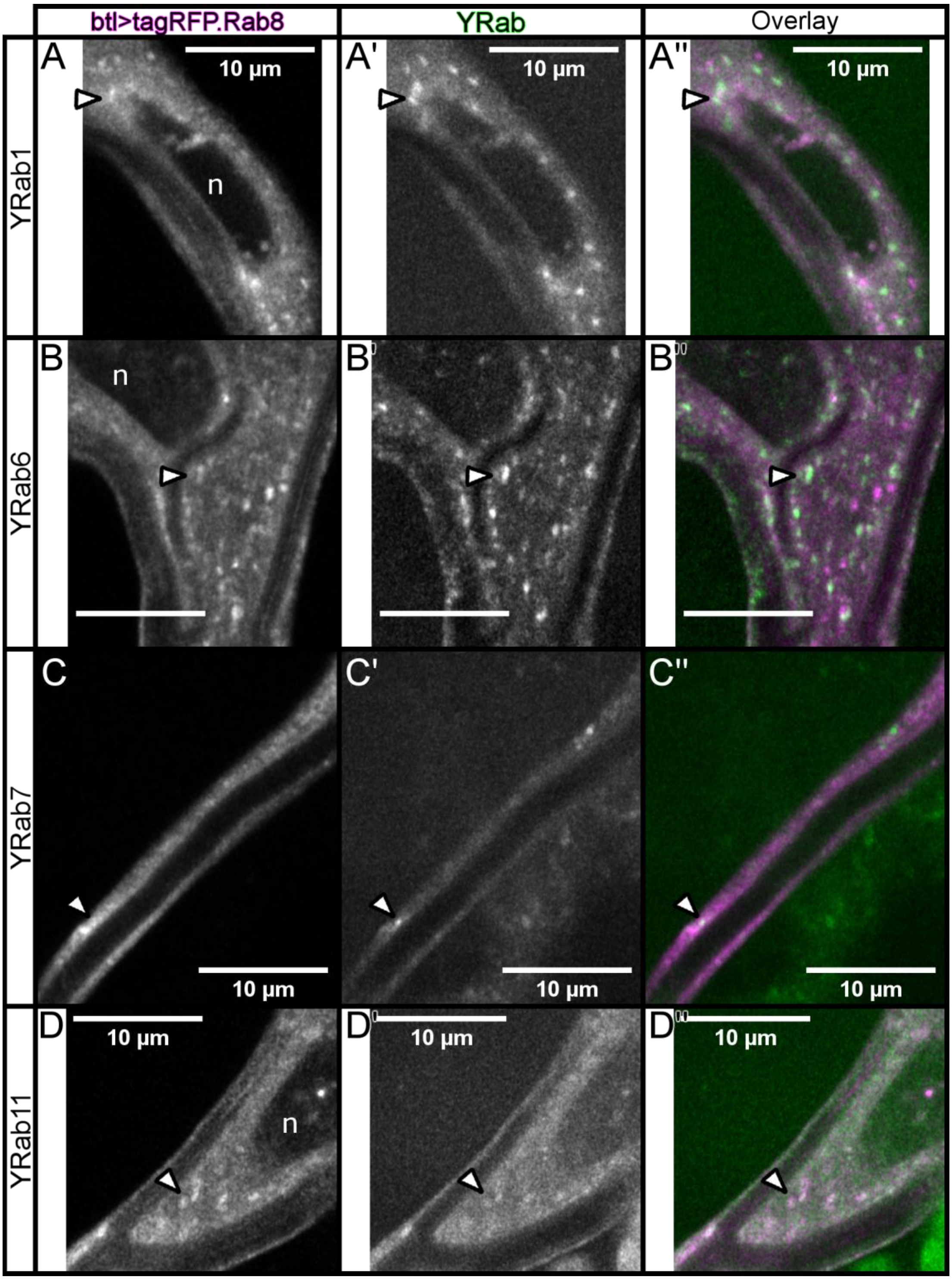

Figure 4.18: Colocalisation of Rab8 with endogenously YFP-tagged marker Rabs
Expression of tagRFP-tagged Rab8 was induced in all tracheal cells by *btl*-Gal4 in animals with an endogenously YFP-tagged marker Rab. Rab1 marks pre-Golgi compartments, Rab6 labels trans- and post-Golgi membranes, Rab7 marks late endosomes and lysosomes, and Rab11 labels endosomal recycling compartments. Images show 200nm thick optical sections of dorsal terminal cells (or a terminal branch in case of YRab7) in heat-fixed third-instar larvae. Quantification in Fig. 4.19A. Arrowheads, examples of overlapping structures. n, nucleus. Scale bars, 10µm.

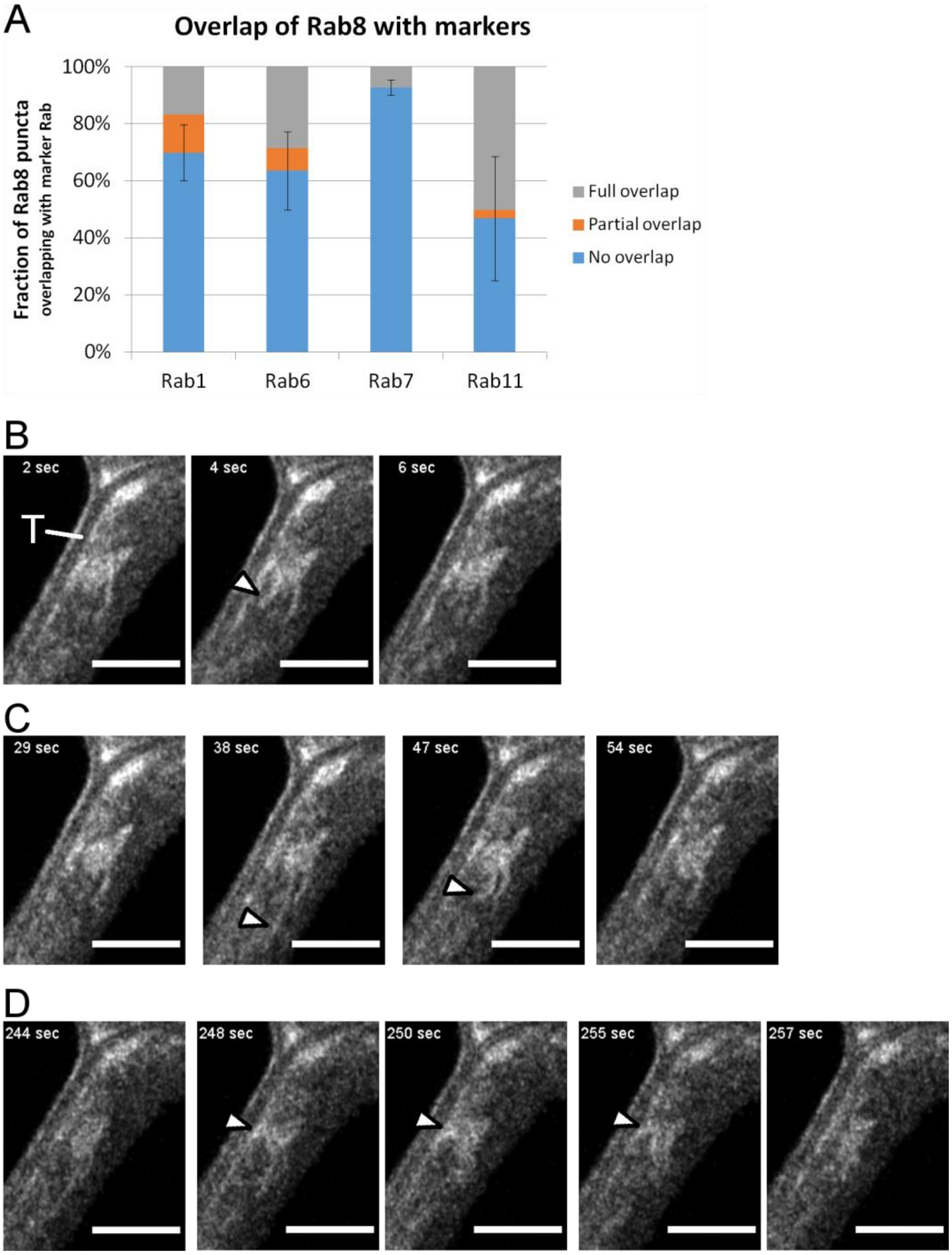

Figure 4.19: Quantification of Rab8 colocalisation and Rab8 subcellular live dynamics

(A) Particle-wise colocalisation of Rab8 with the respective marker Rabs shown in Fig. 4.17. Rab8 particles (puncta) and marker Rab particles were computationally segmented and each Rab8 particle was allocated to one of three categories depending on the percentage of the particle's pixels that were also part of a marker Rab particle: <1%: No overlap; 1-89%: Partial overlap; 90-100%: Full overlap. Error bars show standard deviation of the fraction of "No overlap" particles.

(B-D) Example frames from a live capture of tagRFP.Rab8 in a dorsal terminal branch of a mid third-instar larva anaesthetised with ether. The time lapse was cropped to highlight a dynamic Rab8-enriched structure. Expression of tagRFP.Rab8 was driven by *btl*-Gal4. Scale bars, 5µm.

(B) Example of a short tubulation event, whereby a protrusion (arrowhead) extended and retracted from the structure within 4s.

(C) Examples of a long tubulation event, whereby a protrusion (arrowheads) extended and retracted from the structure over a span of 25.

(D) Example of a fusion event whereby Rab8 from the structure contacted an area of Rab8 enrichment at the apical plasma membrane (arrowheads) for approximately 10s.

4.3.3 The interaction between Rab8 and Stratum is non-canonical in TCs

Recent reports have identified the putative guanine exchange factor Stratum (Strat) as an interaction partner of Rab8 in *Drosophila*. Both in the follicular epithelium of egg chambers (Devergne et al., 2017) and in sensory organ precursor cells (Bellec et al., 2018), Rab8 and Strat cooperate to ensure the proper sorting of basal-directed cargoes. This was shown respectively for the cargoes Collagen or Sanpodo, a factor involved in Notch trafficking. In these cells, loss of Rab8 or Strat resulted in mis-sorting of these cargoes to the apical domain in addition to their delivery to the basal domain. Both the subcellular localisation on endosomal recycling compartments and the apical-membrane directed dynamics of Rab8 structures in TCs suggest a role in polarised trafficking for Rab8, potentially related to sorting apical and basal cargoes. I therefore explored whether the interaction with Strat is conserved in TCs.

To test whether Strat is involved in TC morphogenesis, I induced TCs to express an RNAi transgene targeting *strat* mRNA (Strat-IR) in all tracheal cells driven by *btl*-Gal4. This construct was previously validated in the above cited studies. TCs expressing Strat-IR developed an abnormal "hairy" tube morphology (Fig. 4.20B) strikingly similar to that of Rab8-IR (Fig. 4.20C). This suggested that the function of Strat was related to that of Rab8. To test whether the two interact on a genetic basis with respect to tube morphogenesis, I generated larvae that co-express Strat-IR and Rab8-IR. TCs in these animals showed the same tube morphology as found with either of the two constructs alone (Fig. 4.20D). The defects appeared to be more severe, i.e. a larger section of the tube had additional tubules around it, and was fully penetrant (Fig. 4.20G). The similarity of the individual and combined knockdown phenotypes indicates that Rab8 and Strat act cooperatively with respect to tube morphogenesis. The potentially additive effect could indicate either that Rab8 and Strat act in parallel pathways, or that the two RNAi constructs do not achieve full loss-of-function, and the combined knockdown therefore achieves a higher efficiency.

Strat is predicted to be a guanine exchange factor of Rab8, i.e. an activator. This would place it the same pathway as Rab8, and upstream of it. It would also imply that the abnormal phenotype in TCs expressing Strat-IR could be due to a lack of Rab8 activation. If Strat is indeed required to activate Rab8, simply overexpressing Rab8 might not rescue the defects associated with Strat-IR, because the excess Rab8 would still remain inactive in absence of Strat. However, co-expressing a constitutively-active mutant of Rab8 should reduce the defects caused by the lack of Strat. I therefore tested whether co-expressing a putative constitutively-active mutant of Rab8 (Rab8CA) with Strat-IR could rescue the tube defect. This Rab8 bears a Q67L mutation in the conserved GTPase active site, which is predicted to make it unable to hydrolyse GTP and thereby deactivate itself. I also performed the same experiment with a wildtype form of Rab8 (Rab8WT). Almost all observed TCs co-expressing both Strat-IR and either Rab8WT (Fig. 4.20E) or Rab8CA (Fig. 4.20F) had a normal phenotype (Fig. 4.20G), indicating near complete rescue of the defective tube morphology associated with Strat-IR expression.

These results show that Strat indeed acts upstream of Rab8 in TC tube morphogenesis. The high efficiency of the rescue by Rab8 further suggests that activating Rab8 is the only function performed by Strat in TCs. However, similar to sensory organ precursor cells (Bellec et al., 2018), both a wildtype and a constitutively-active Rab8 protein were able to rescue the defects associated with Strat. This contradicts the canonical role of Strat as an activator of Rab8 and suggests that instead, Strat is required by TCs to produce or maintain a sufficient amount of Rab8 protein. Despite this, the interaction with Strat suggests that also in TCs, Rab8 functions in polarised trafficking.

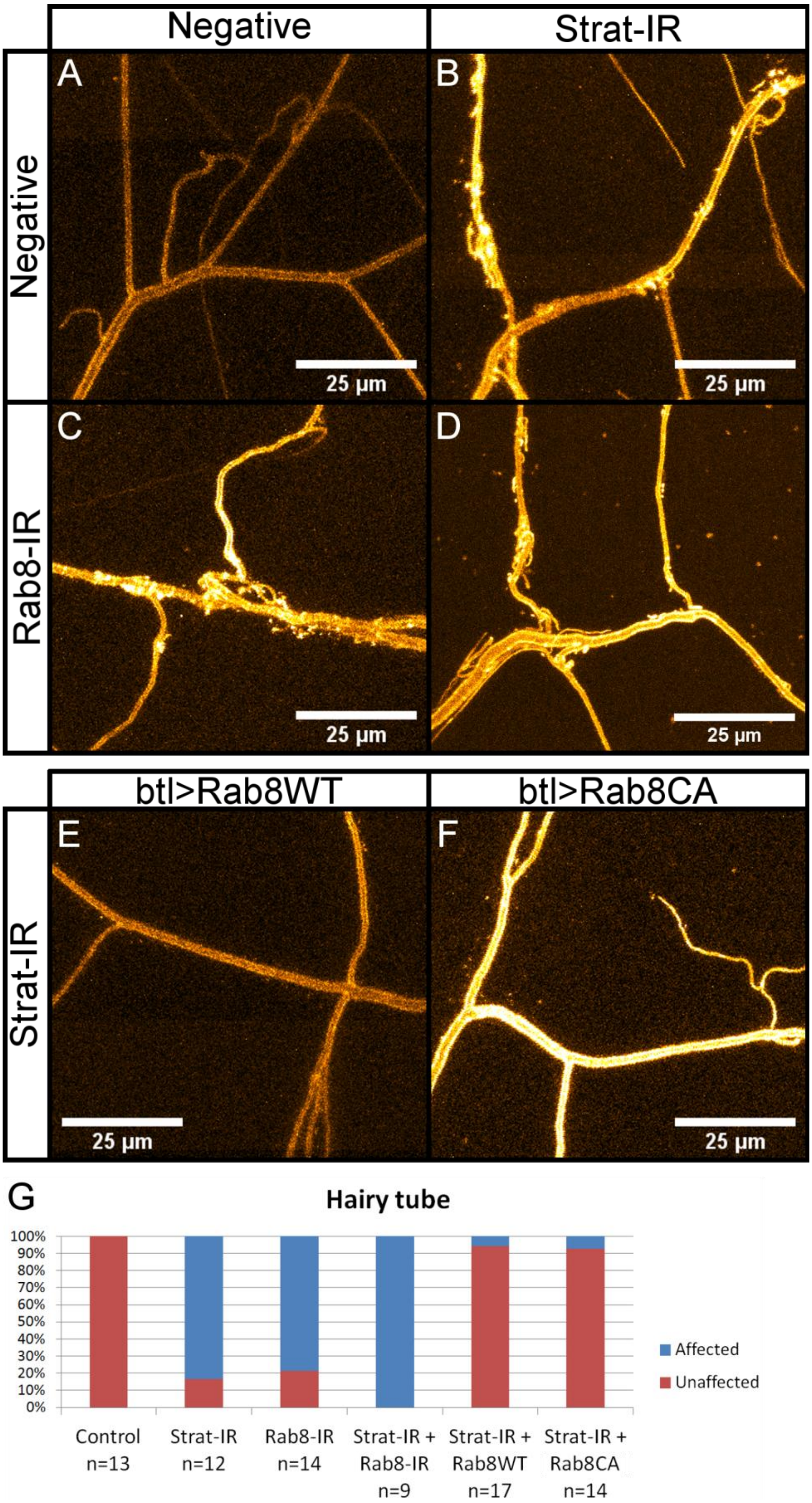
Negative
Strat-IR
Negative
A
25 µm
B
25 µm
Rab8-IR
C
25 µm
D
25 µm
btl>Rab8WT
btl>Rab8CA
Strat-IR
E
25 µm
F
25 µm
G
Hairy tube
100%
90%
80%
70%
60%
50%
40%
30%
20%
10%
0%
Control n=13
Strat-IR n=12
Rab8-IR n=14
Strat-IR + Rab8-IR n=9
Strat-IR + Rab8WT n=17
Strat-IR + Rab8CA n=14
Affected
Unaffected

Figure 4.20: Epistasis of Strat and Rab8 in subcellular tube morphogenesis
The genetic interaction between Strat and Rab8 with respect to the morphology of the terminal cell tube was tested using RNAi constructs against *strat* and *rab8*. Animals expressing Rab8-IR were siblings of the respective counterpart not expressing it and were identified by the absence of a marked balancer chromosome.
(A-D) Z-projected optical stacks showing apical extracellular matrix autofluorescence of dorsal terminal cells in heat-fixed third-instar larvae.
(A) Terminal cell in a larva expressing DsRed in all tracheal cells. Sibling of the larva in (C).
(B) Terminal cell in a larva expressing DsRed and Strat-IR in all tracheal cells, showing the "Hairy tube" phenotype previously associated with Rab8 loss-of-function. Sibling of the larva in (D).
(C) Terminal cell in a larva expressing DsRed and Rab8-IR in all tracheal cells. The tube is enveloped by a multitude of smaller tubules ("Hairy tube").
(D) Terminal cell in a larva expressing DsRed, Strat-IR and Rab8-IR, showing the same defect as the cells in (B) and (C).
(E) Penetrance of the phenotypes shown in (A-D), showing the percentage of observed terminal cells that had the "Hairy tube" defect anywhere along their tube network.

4.3.4 A mutant Rab8 interferes with apical trafficking

The most direct approach to explore a potential role of Rab8 in polarised trafficking is to identify a cargo protein which requires Rab8 to reach its normal target membrane. I therefore sought to identify proteins which TCs traffic towards the basal and respectively the apical membrane to test whether any of them are mis-distributed in TCs with perturbed Rab8 function.

For epithelial cells, the prime candidates as basally secreted proteins are components of the basement membrane, such as Viking (Vkg), a subunit of Collagen IV, Perlecan and Laminins. I obtained *Drosophila* lines with fosmid insertions that express GFP-tagged versions of these proteins under their normal genomic regulatory sequences. However, combining these constructs with tracheal expression of Rab8-IR had no effect on the GFP-tagged proteins. It is known that tracheal cells do not express Collagen themselves (Ríos-Barrera et al., 2017). Rather, the basement membrane of the tracheal system contains Collagen secreted by the fat body (Pastor-Pareja and Xu, 2011). It is therefore likely that the other proteins I tested, Perlecan, Laminin A and Laminin B, are likewise not expressed by TCs and consequently not subject to Rab8 trafficking. As a workaround, I attempted instead to induce expression of Vkg transgenically, as it might still be secreted basally even if TCs do not normally express it. However, GFP-Vkg driven by *btl*-Gal4 was retained in cytoplasmic aggregates. I was therefore not able to test any effect of Rab8 perturbation on basal-directed trafficking.

To study apical-directed trafficking, I used an endogenously GFP-tagged variant of the apical polarity determinant Crumbs (Crb). This transmembrane protein is enriched in the apical membrane in TCs (Fig. 4.21A). I tested whether expression of Rab8-IR modified the distribution of Crb-GFP. This was not the case since Crb-GFP remained enriched at the tube in all observed TCs (Fig. 4.21B). As an alternative method of perturbing Rab8 function, I tested whether inducing expression of Rab8CA could influence Crb trafficking. I used a *Drosophila* line generated in our lab by S.

Sigurbjörnsdottir with an insertion of UAS-inducible RFP-tagged Rab8CA. When driven by *btl*-Gal4, this transgene modified the distribution of Crb-GFP. The tube enrichment was lost or reduced, but again only in some TCs. However, all TCs expressing Rab8CA also formed many cytoplasmic aggregates of GFP (Fig. 4.21C). Some of these aggregates coincided with RFP.Rab8CA structures, while others seemed to actively exclude RFP.Rab8CA.

The Rab8CA mutant is not sufficiently characterised to make hypotheses about the mechanism by which it disrupts Crb-GFP distribution. Despite this, these observations demonstrate that Rab8 in TCs is capable of interfering with the trafficking of polarised cargoes. They are consistent with a Rab8 function similar to that found in the follicular epithelium, where Rab8 prevents the apical delivery of basal-directed cargoes. The retention of Crb-GFP in cytoplasmic aggregates would in this case be interpreted as an inhibition of apical-directed trafficking due to the excessive activity of Rab8CA.

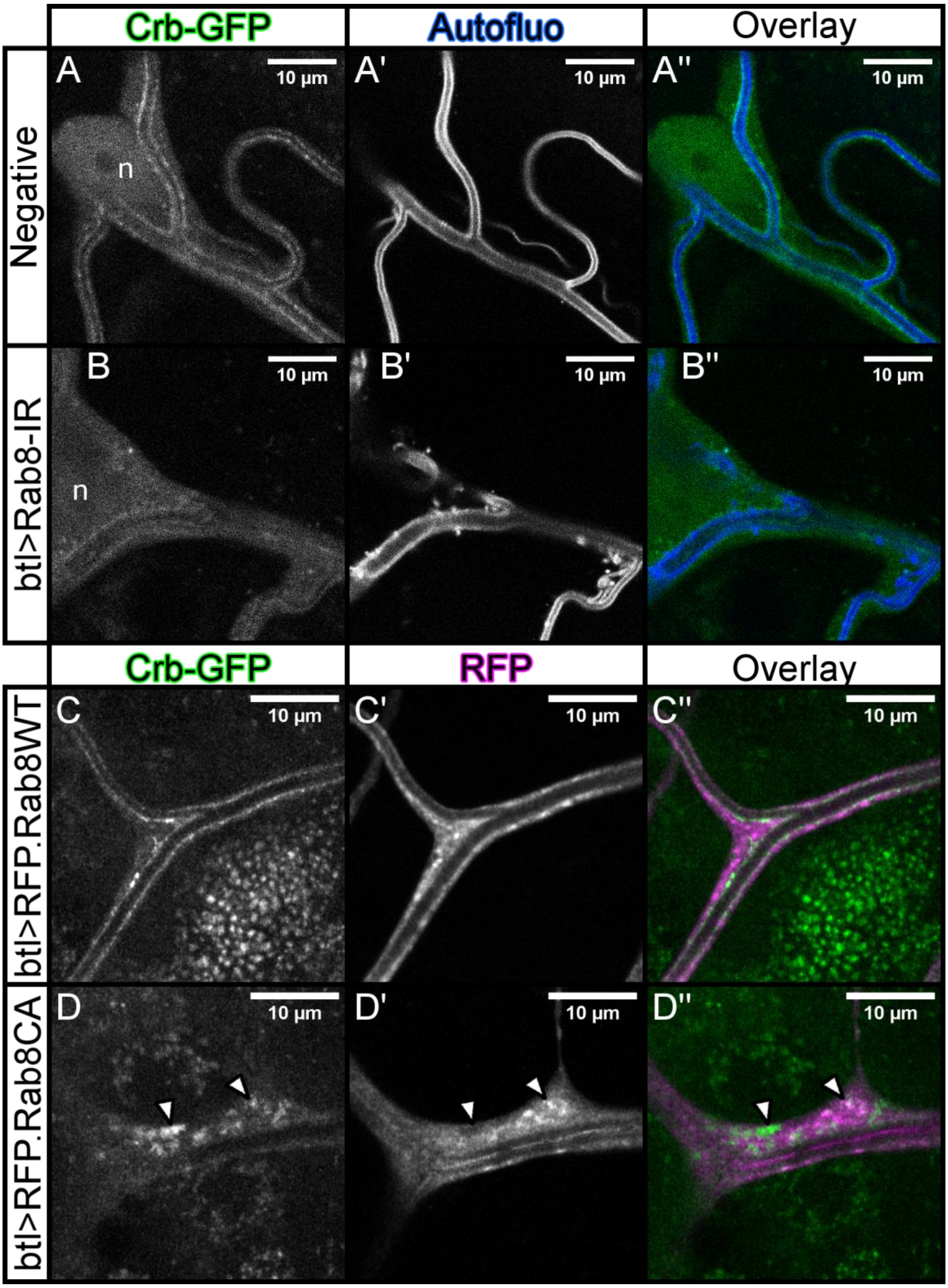

Figure 4.21: Effect of interference with Rab8 function on the localisation of Crb
A *Drosophila* line with endogenously GFP-tagged Crb (Crb-GFP) was used to test whether perturbing Rab8 affects apical-directed protein trafficking. All images show dorsal terminal cells in larvae with Crb-GFP. (A) and (B) are 1µm thick optical sections acquired in anaesthetised live larvae. (C) and (D) are 200nm sections acquired in heat-fixed larvae. n, nucleus. Scale bars, 10µm.

(A) Crb-GFP is enriched in the apical membrane in control terminal cells. Sibling of the larva in (B), distinguished by the presence of a marked balancer. (A) GFP channel, (A') 405nm channel, showing autofluorescence from apical extracellular matrix, (A'') overlay of the two channels.
(B) Sample from a larva expressing Rab8-IR in all tracheal cells, driven by *btl*-Gal4. Crb-GFP is enriched at the apical membrane as in controls. The apparent lower intensity of the signal may be an imaging artifact and was not consistent. Sibling of the larva in (A), distinguished by the absence of a marked balancer."Hairy tube" phenotype is visible on the bottom right.
(C) Sample from a larva expressing a wildtype Rab8 fused to tagRFP (RFP.Rab8WT) in all tracheal cells, driven by *btl*-Gal4. (C) GFP channel, (C') RFP channel, (C'') overlay of the two channels.
(D) Sample from a larva expressing a putative constitutively-active mutant of Rab8 fused to tagRFP (RFP.Rab8CA) in all tracheal cells, driven by *btl*-Gal4. Crb-GFP formed intracellular aggregates in all observed cells of this genotype. Crb-GFP was not enriched at the tube in the displayed cell, but this was not the case in others. The thin line of RFP signal centred within the tube is an imaging artifact. Arrowheads, Crb-GFP aggregates, one excluding RFP.Rab8CA (left) and one colocalising with RFP.Rab8CA (right).

5. Discussion

The work presented here explored the role of Rab GTPases in the morphogenesis of the terminal cells (TCs) of the tracheal system in *Drosophila melanogaster*. The central aim of my work was to conduct a loss-of-function screen across all Rabs in a manner that provides high confidence in the relevance of the identified Rabs to TC morphogenesis. This led to a three-part structure of my work. The first part was a quantitative phenomic analysis of TC morphologies under different conditions, which established the ground work for systematic study of TC phenotypes and thereby enabled the appropriate interpretation of the results of the screen. The second step was the screen itself, based on the indirect knockdown of endogenously tagged Rabs, and the validation of its results. The third part was the investigation of the function of Rab8 in TC morphogenesis, a candidate identified in the screen as potentially unique among Rabs.

5.1 Morphology of the subcellular tube in terminal cells

5.1.1 Current standards of TC phenotype analysis

The morphology of the subcellular tube in larval TCs has received little attention in the past. To date, less than 30 articles on the subject have been published, and discussions about the interpretation of mutant TC phenotypes have been informal. There is general awareness that defects can manifest variably between branches within the same cell, and that morphological features that could be considered abnormal can be observed in wild type TCs. However, these have not been studied and reported systematically. Past reports have instead taken the approach of obscuring these details by using implicit definitions of what constitutes a defect. Descriptions of mutant phenotypes did not consider the cell's entire morphology, but rather focussed on one particular morphological feature that was presented as the characteristic defect resulting from the candidate gene's loss-of-function. A common paradigm of reverse genetics, where similar phenotypes are interpreted to imply similar functions, was then used to group genes whose mutant phenotypes included the chosen feature. The literature context of the genes known usually from mammalian cells was then applied to construct a molecular pathway and infer its function in TCs. In cases where phenotypes were quantified, this was limited to determining the cell-wise penetrance, i.e. the percentage of mutant TCs that manifest the feature of interest on at least one branch.

Decades of genetics have shown that the interpretation of "similar phenotype, similar function" is generally viable, and its use has been elemental in the study of developmental biology, particularly of *Drosophila*. However, this relies on an adequate distinction of normal and abnormal phenotypes, since otherwise phenotypes can erroneously be considered consequences of a particular gene's loss-of-function when in fact they are a cumulative consequence of unrelated factors. In this regard, my work contributes an important reference collection of morphological features that can appear in TCs without any specific genetic deficiency and must therefore be considered normal. Most mutant phenotypes reported in past studies, namely localised dilations of the tube (Schottenfeld-Roames et al., 2014), multiple parallel tubes within one branch (JayaNandanan et al., 2014; Levi et al., 2006; Nikolova and Metzstein, 2015), and disconnected pieces of tube (Rosa et al., 2018) indeed all present a quality that is never found in TCs without a specific deficiency. Yet, establishing that a phenotype is abnormal and specifically caused by a gene's loss-of-function is not sufficient to make inferences about the gene's function or its molecular pathway(s) of action. This is particularly important when the aim of a study is to characterise the interaction between genes using phenotypic defects. Depending on the outcome, epistasis experiments can provide valuable information about a genetic interaction, even when nothing further is known about the phenotype in question. These experiments were not done in most studies on TCs, and an association between genes was instead inferred arguing from the presence of similar defects in both mutants. This can still be permissible when the genes in question are sufficiently characterised in other biological systems and the conservation of their function has been demonstrated, or is reasonable to assume. However, our understanding of subcellular tube formation in general and TC morphogenesis specifically is rudimentary. Additionally, some proteins such as Crumbs, whose role in other epithelial cells is known, appear to function differently in TCs due to their unique structure (JayaNandanan et al., 2014; Jones and Metzstein, 2011; Schottenfeld-Roames et al., 2014). Currently, we do not have an overview of the cellular processes that contribute to subcellular tube morphogenesis in TCs, or how they relate to the various defects observed in the past. Phenotypes characterised by multiple tubes per branch or curled tubes at branch tips for example have been associated with molecular pathways that are commonly considered distinct, such as basal adhesion (Levi et al., 2006), apical actin dynamics (JayaNandanan et al., 2014), chemotactic signalling (Ukken et al., 2014), as well as membrane trafficking (Schottenfeld-Roames and Ghabrial, 2012).

5.1.2 Study rationale

The lack of specificity of phenotypes to particular molecular pathways was the primary concern of the phenomic study reported in the first Results subsection. This work presents the first comprehensive qualitative and quantitative description of TC phenotypes, taking into account the morphology of the entire cell, and attempting to compile a complete list of phenotypic features that could be considered abnormal. I contrasted TC phenotypes under four different loss-of-function conditions elicited by RNA interference (RNAi) and under two different temperature conditions, which modulates the expression level and therefore the efficiency of RNAi. The aim of this work was to identify an analytical method that could infer which molecular pathway a candidate gene should be associated with, based only on the loss-of-function phenotype as visualised by the autofluorescence of the TC lumen's apical extracellular matrix. I therefore selected three genes with known functions and previously described TC tube phenotypes as controls to test different approaches of analysis. Two of the genes, *rab5* and *syx7*, are known to physically interact during early endosome fusion in Drosophila eye discs (Morrison et al., 2008), and mutations in these genes have been shown to produce the same type of abnormality in TC tubes (Schottenfeld-Roames et al., 2014). For my analysis, I have therefore employed a model where rab5 and syx7 physically interact in TCs as they do in other biological systems. They are thus considered part of the same pathway, and a valid analytical method should associate them with each other, or group them together. The third gene, *talin*, is a well-characterised gene in other biological systems (Klapholz and Brown, 2017), and its function has not been associated with either *rab5* or *syx7* in TCs (Levi et al., 2006) or in other systems. It should therefore not interact with either of the two physically. *Talin* is thus part of a distinct pathway, and a valid analytical method should not associate it with either *rab5* or *syx7*. Finally, I included *rab8* as a candidate of unknown functions or associations with the control genes. Thus, conceptually, *rab5*, *syx7* and *talin* constituted a "training set" and *rab8* constituted the test case. The analysis then mainly addressed two questions: 1) What constitutes a "normal" and an "abnormal" phenotype? 2) How can TC phenotypes be analysed to associate candidate genes according to their molecular pathway of function?

To answer the first question, I included negative controls with no specific perturbation of any gene's function. I then screened both control TCs and TCs expressing RNAi transgenes against each gene of interest for tube morphologies that might be considered abnormal. This resulted in the formal definition of stereotypical branch and tube morphology (essentially "straight branch with straight tube"), and a list of non-stereotypical morphologies or features whose occurrences can be quantitated for each cell (see Results 4.1.3). Scoring the control samples revealed that 11 of 15 non-stereotypical features occured in control cells and must therefore be considered part of the natural variability of TC morphology. This does not mean that any morphology that fits the definition of one of these 11 categories should be disregarded when characterising new mutant phenotypes. The comparison between the frequencies of these 11 classes in control TCs and their RNAi-expressing counterparts showed that part of the profile of a loss-of-function phenotype can be an increased frequency per branch of features that also appear in controls. Indeed, the abnormalities of TCs expressing *talin*-RNAi were entirely contained in categories that also appear in control TCs, such as the Wavy Lumen, Curled Tip and Delayed Branching categories. The characteristic difference was that *talin*-RNAi cells manifested these features at almost every branch, while they were comparably rare in controls. In future work, should a mutant reveal only features that match the 11 features that are part of wild type variability, it can thus be recommended that the features should be quantified as defined here, in mutant and control TCs from cultures grown in parallel. The second question, how genetic associations can be inferred from TC phenotypes, was the main subject of the study and is discussed in the following sections.

5.1.3 Delineation of feature category definitions

Among the features that can appear in control TCs, the Curled Tip feature is of interest because it has previously been used as the defining feature of the *whacked* gene's mutant phenotype (Schottenfeld-Roames and Ghabrial, 2012). More specifically, the study focussed on particularly severe instances of Curled Tips that were never found in a similar severity in control TCs in my sample. When the observations are so clearly distinct, this is a valid definition of "abnormal". However, under other circumstances, Curled Tips also manifest in severities that are between what might be seen in a control TC and what has been reported for *whacked* mutant TCs. This was the case for all RNAi samples in my study. In the cited study, the feature was primarily used for analysing phenotype modification in TCs co-expressing different transgenic construct, for which it was a useful feature to observe. However, it is not useful in a general sense such that any gene whose mutant causes Curled Tips should be associated with *whacked*. To reach definitions that could be of general use, there were several options. For example, in the case of Curled Tips, the diameter of the curled-up tube bundle could be measured and analysed as a continuous variable, or subdivided into categories such as "small" and "large" Curled Tip according to certain size thresholds. I decided against such fine-grained feature categories because it seemed unlikely that different bundle sizes relate to meaningul biological properties. Regardless of bundle size, the common property was the tube "over-reaching" the end of the branch, which could relate to some type of deregulation or uncoupling of tube and branch growth. This aspect was therefore chosen as the definition of the Curled Tip category, and curl size was disregarded. Similar thought processes also underly the process of defining the other feature categories, with the aim of finding categories that should remain robust also for as of yet unobserved morphologies that studies of novel genes might reveal.

5.1.4 Interpretation of phenomic clusters

The aim of my analysis was to validate the collection of definitions of morphological features as a generally viable approach for describing loss-of-function phenotypes related to the subcellular tube of TCs. My hypothesis therefore was that the frequencies of all features reflected the molecular function in which a TC is deficient. If this was the case, it should be possible to identify discrete groups of cells with similar quantitative profiles, and these groups should correspond to the molecular pathways as described earlier. Identifying groups in a high-dimensional dataset such as this is not feasible manually and I therefore used clustering algorithms, a type of computational method used to classify data into coherent groups. If the feature definitions accurately capture TC phenotypes, performing cluster analysis on this dataset should effectively execute a grouping by phenotypic similarity. And, since phenotypic similarity is the criterion for associating one gene (or one mutant) with another, the grouping should reflect the association between *rab5* and *syx7*, as well as the lack of association between these two and *talin*.

Specifically, I tested two clustering algorithms. The first, K-means clustering, can be thought of as a subdivision of the sample space into K sectors, whereby the algorithm identifies an arrangement of the sector boundaries that minimises the distance of each data point from the centre of its sector/cluster. However, the algorithm does not determine what number of sectors is appropriate for the dataset. This property is central to gaining an understanding of a dataset using K-means. The algorithm was run using a range of values for K, and two numerical measures were used to evaluate the goodness of clustering for each K. The first was the within-sum-of-squares, which reflects the "tightness" of clustering, i.e. the dispersion of data points around their cluster's centroid. The second measure was the silhouette score, which reflects the distance between clusters. The best clustering in the sense of these two measures was obtained by subdividing the dataset into either 2 or 4 clusters, which suggests that there were up to four groups of cells with quantitatively similar phenotypes. Assessing which cells had been sorted into which clusters showed that in the case of 2 clusters, the algorithm had effectively divided the dataset into control and non-control cells. In the case of 4 clusters, the grouping was consistent with the grouping expected according to my hypothesis. This means that there was one group of primarily control cells, one group of primarily *talin*-RNAi expressing cells, and one group of *rab5*-RNAi and *syx7*-RNAi expressing cells. The fourth group consisted of *rab5*-RNAi and *rab8*-RNAi expressing cells, which suggests that *rab8* and *rab5* have shared aspects of function that are not shared with *syx7*.

The second algorithm was hierarchical clustering. Rather than subdividing the sample space into a defined number of sectors, this instead allocates each data point to its closest data point or already grouped cluster. Depending on the exact distribution of points in the sample space, this can reveal meaningful groups that would not be discovered by K-means. I used hierarchical clustering as a validating method for K-means, i.e. I tested whether similar groups of cells can be identified as those returned by K-means. This was indeed the case, since a modified distance cutoff produced four groups whose compositions were very similar to the four clusters segregated by the K-means algorithm, reinforcing that these groups reflect natural groupings in the dataset.

This demonstrates that the frequency of morphological features as defined here indeed provides a quantitative description of TC phenotype that accurately recapitulates the associations (or lack thereof) between known genes. Ideally, TC phenotypes should thus be described as done here, or in a similar manner, to ensure that the analysed measure of phenotype reflects the underlying genetics.

Limitations

One significant question that remains unanswered by these data is the level of detail to which these definitions of morphological features resolve genetic associations. The present choice of test genes represented only two molecular pathways, namely integrin-linked adhesion represented by *talin* and early endocytosis represented by *rab5* and syx7. However, the shared function that caused the phenotypic similarity between TCs expressing *rab5*-RNAi and *syx7*-RNAi, and their difference to *talin*-RNAi, could be on a higher level than their molecular pathway. For example, it is possible that TCs with a loss-of-function anywhere in their endomembrane system produce phenotypes that are quantitatively similar to those under *rab5*- or *syx7*-RNAi, since *talin* is not functionally related to any part of the endomembrane system according to current knowledge. Given that my later work suggests that Rab8 functions in endosomal trafficking, the grouping of TCs expressing *rab8*-RNAi with *rab5*-RNAi but not *syx7*-RNAi indicates that the feature categories used here resolve functional relatedness to a level that can distinguish at least different parts of endosomal system.

In addition, a difficulty for phenotypic analysis with RNAi is that it usually only effects an incomplete knockdown. I included two different temperature conditions (18°C and 29°C) to address this problem by establishing the phenotypic range resulting from different knockdown efficiencies. Indeed, some TCs expressing *rab5*- or *rab8*-RNAi at lower levels due to the lower temperature were categorised with control TCs, indicating a normal phenotype. One potential problem for future experiments using the same categories of features could be genes whose associated morphological features do not correlate equally with the knockdown efficiency. That is, if the frequency of some features is very sensitive to knockdown efficiency but the frequency of others is not. In such a case, two functionally related genes would not be grouped together if the knockdown efficiencies used for the comparison were different. However, modifying the level of knockdown by comparing different temperatures or co-expression of Dicer2 could potentially resolve such cases.

5.1.5 Possibility of non-phenomic analysis of TC morphology for functional inference

The primary aim of phenotypic analysis in reverse genetics is to create associations between new, unknown genes, and already characterised genes. Such associations are usually connotated with the expectation that genes that are associated with each other are part of a shared biological mechanism or molecular pathway. As described above, this assumption does not hold in TCs, where mutations in proteins from different pathways lead to similar morphological defects. Conversely, regarding the overall morphology of the TC, it appears loss-of-functions in the same pathway can also lead to different phenotypes. This was demonstrated by the preliminary experiment where I attempted to identify which gene's function a TC was lacking based on a subjective impression of its overall phenotype. I was clearly able to distinguish TCs expressing *rab5*-RNAi and *syx7*-RNAi, which should not be the case if both caused the same phenotype as a consequence of the relatedness of their functions. While my further analysis demonstrated that a phenomic description of TC phenotype can disentangle gene function despite similar morphological features, this is a time consuming process and in practice it would be preferable if any of the individual features were sufficient to analyse. The correlation and principal component analysis of my dataset showed that none of the features correlate with any other feature to such a degree that one type of feature could be safely ignored in future assessments. The frequency of each feature thus contains unique information, though unique does not necessarily imply useful for the purposes of interpreting TC phenotypes.

A question was thus whether any individual aspect of TC phenotype could be used to infer new associations of a candidate gene. This was not the case for branch number, "healthy fraction" (the fraction of branches with stereotypical morphology), and 10 of the 15 different types of morphological features, because their distributions in *talin*-RNAi could not be distinguished from either *rab5*-RNAi or *syx7*-RNAi. The other five categories of morphological features were specific to TCs expressing *rab5*-RNAi and *syx7*-RNAi, and were found neither in *talin*-RNAi nor the control sample. These five features (Disconnect, Cyst, Hairy Branch, Hairy Junction, Disrupted Tip) are therefore specific to shared aspects of the functions of *rab5* and *syx7*. It is unlikely that they are specific to the endocytotic pathway to which *rab5* and *syx7* belong, however, because TCs expressing *rab8*-RNAi presented the same features and *rab8* is not part of the endocytic pathway in other organisms. Hence, they must result from a higher-level aspect of function that *rab5*, *rab8* and *syx7* share. The presence of these features in an unknown gene's mutant phenotype thus would allow the inference of an association with *rab5*, *syx7* and *rab8*, but not with a specific molecular pathway. Similar reasoning applies also to the additional feature identified in the later work during the YRab-gfpIR screen, Asymmetric Autofluorescence. This feature was never found in controls, or any of the four RNAi-expressing samples analysed in the phenomic study. It was shared between a large group of *rab* genes, but not *rab8*. It is therefore already possible to determine that this feature is specifically related to a subset of *rab* functions. Given the involvement of *rabs* in membrane trafficking, this most likely constitutes a trafficking pathway within the endomembrane system as will be discussed further below. For perturbations such as *talin*-RNAi whose resulting phenotypes only show morphological features that also appear in controls, a quantification of the frequencies per branch and per cell is crucial. Such studies should make explicit the definitions for normal and abnormal morphologies that they use, and how the two are distinguished.

5.1.6 Modulation of normal TC morphogenesis by temperature

Quantifying the phenotype of TCs in control animals showed an effect of the 29°C temperature environment compared to 18°C culture that has not been described in the past. At 29°C, TCs had an increased number of branches per cell and also a higher fraction of branches with fully stereotypical morphology. This finding is interesting because so far it was only known that TC branch numbers increase depending on the larva's nutrition and the availability of oxygen. The former effect is mediated by insulin-like peptides secreted by nutrient-sensing neurons (Linneweber et al., 2014; Wong et al., 2014), and the latter is mediated by oxygen-sensing by the TC's target tissue and increased Bnl/Btl signalling (Centanin et al., 2008; Jarecki et al., 1999). Conceptualising how TCs could respond to increased temperature is challenging. An intuitive explanation could be a general increase of larval size, which would be expected to cause a larger number of branches because the size of each individual branch remains constant. However, larval size decreases as the culture temperature increases (Ghosh et al., 2013). TCs therefore grow a larger number of branches despite a smaller size of the target tissue. Similarly, the difference cannot be explained by a systemic modulation of insulin levels in response to the warm environment. At colder temperatures, a population of cold-sensing neurons stimulates insulin signalling (Li and Gong, 2015). Conversely, TCs should receive lower general levels of insulin signal at the higher culture temperature, and therefore should grow fewer branches if their branch number was subject to this mechanism. Another potential explanation could be the decreased solubility of oxygen at higher temperatures, and an effectively hypoxic behaviour of tissues as a consequence (Frazier et al., 2001). This is contradicted by the subcellular tube phenotype of control TCs at 29°C. Hypoxic conditions are associated with tortuous tubes, similar to the Wavy Lumen feature in the present study (Jarecki et al., 1999). This feature was less frequent at 29°C, rather than more frequent as would be expected if the increase in TC branches was due to hypoxic signalling activity from the target tissue. There is thus currently no attractive explanation for this observation. One could venture that it is related to the higher efficiency of mobilising glycogen stores in warm-adapted larvae (Bochdanovits and De Jong, 2003).

5.2 Functions of Rab GTPases in tracheal morphogenesis

5.2.1 Indirect knockdown of tagged proteins

In the main part of my work, I conducted a knockdown screen on Rab GTPases. My approach was similar to the previously reported "*in vivo* GFP RNAi" (iGFPi) method (Pastor-Pareja and Xu, 2011), with the difference that the targeted genes were endogenously tagged with YFP instead of GFP, and I used a different Gal4 driver. I termed the method YRab-gfpIR in my work to reflect this. The principle of this approach was demonstrated along with the original publication of the YRab lines (Dunst et al., 2015). Although the ability of GFP-RNAi constructs to knock down YFP has not been formally documented, it is known that antibodies specific for GFP also label YFP (Yu and McMahon, 2006). This is not the case for the respective "enhanced" versions of the fluorescent proteins (EGFP). The RNAi constructs tested in my work were specific to EGFP and EYFP, and they did not affect a classic GFP (data not shown). However, the YRab knock-ins were also generated with the EYFP variant (Dunst et al., 2015). The nanobody constructs effected a partial knockdown both against classic GFP (data not shown) and against YRabs as tested here.

A major concern in the use of RNAi constructs has been false discovery. Both the risk of false positives for example due to off-targets (Echeverri et al., 2006; Green et al., 2014; Mohr et al., 2014; Sigoillot and King, 2011), and false negatives (Booker et al., 2011) have been discussed in depth for different model systems and RNAi techniques. False discovery rates for different RNAi libraries have been estimated between 1 and 30% (Perrimon and Mathey-Prevot, 2007). Standard guidelines for RNAi experiments have been established (Sharma and Rao, 2009; Sigoillot and King, 2011), with a consensus that experiments using RNAi must be validated. A proposed definitive validation is the rescue of an RNAi-induced phenotype by co-expressing an RNAi-resistant variant of the transcript, though this comes with its own complications due to the non-physiological expression of the rescue transgene (Mohr et al., 2014). Alternatively, mutant analyses can be used to confirm the result, although still many genes remain where no mutants are available. In such cases, new mutants can be generated with relative ease now using CRISPR or P-element excision, but both then require first the validation of the new mutant. In contrast, the indirect knockdown approach permits a simple control experiment to exclude the possibility of false-positives. By expressing the RNAi construct in a genetic background where no gene is endogenously tagged, it is possible to test whether expressing the tag-knockdown itself elicits unspecific defects. The main drawback of this method is the prevalence of false negatives as demonstrated by my follow-up experiments to the knockdown screen, which revealed several additional Rabs to be involved in TC morphogenesis.

5.2.2 Expression pattern of btl*-Gal4*

When interpreting the results of my knockdown screen, an important aspect is the expression pattern of the Gal4 driver inducing the UAS-RNAi transgene and therefore the selection of cells in which the Rab loss-of-function is elicited. I used the well-established *btl*-Gal4 construct (Shiga et al., 1996), which is popular primarily to induce expression of transgenes in the tracheal system. Some specific details about the expression pattern of *btl*-Gal4 have not been formally reported, but they are also unlikely to bear significance for my work. Specifically, *btl*-Gal4 is also active in many epidermal cells in the head region, as well as some individual epidermal cells throughout the rest of the body (data not shown). There are also a small number of tracheal cells that were never found expressing a UAS-DsRed transgene under *btl*-Gal4, and therefore should also not express the GFP-RNAi construct. Two of these cells were located in the anterior anastomosis between the two dorsal trunks, and a small group of cells was found in each of the adult precursor pockets located on the branching point of the lateral branch from the dorsal trunk in the second and third tracheal metamere. Since none of these cells at any point in embryonic or larval development interact with the cells of the dorsal branches that I studied, the presence of these cells should be of little concern. The variability of phenotypes resulting from Gal4-driven RNAi has in the past been attributed to a variability of Gal4 expression itself between cells of the same type (e.g. Swaminathan and Pile, 2010). This hypothesis has not been tested experimentally, however.

The second aspect next to the spatial expression pattern are the dynamics of GFP-RNAi expression induced by Gal4 across time. The onset of *btl*-Gal4 activity has not been precisely determined, but fluorescent proteins driven by this Gal4 were found as early as the fate specification of tracheal cells from the ectoderm (data not shown). It can therefore be assumed that tracheal development is affected in animals expressing YRab-gfpIR under *btl*-Gal4 as soon as the cells adopt the tracheal fate. Similarly, the dynamics of *btl*-Gal4 expression across time have not been studied, and it is possible that neither the amount of Gal4 protein nor the amount of RNAi transgene expression remain stable throughout development. The mRNA of the *btl* gene itself has a large expression peak during mid-embryogenesis, coinciding with the onset of tracheal pit invagination (Brown et al., 2014). Its expression then declines rapidly until stage 16 of embryogenesis, when the primary and secondary structures of the tracheal system have concluded development, and then remains low but detectable until hatching and throughout larval life. These dynamics were obtained for the animal as a whole and the expression of *btl* specifically by tracheal cells has not been determined at such time resolution. Salivary gland cells begin expressing only around stage 13 (Shishido et al., 1993), long after the *btl* expression peak, suggesting that salivary glands do not significantly influence *btl* expression dynamics in the embryo overall. However, even if one assumes that *btl*-Gal4 follows the same expression pattern as the *btl* gene itself across time, the resulting efficiency of Gal4-driven RNAi depends on several additional factors. These include the stability of *gal4* mRNA and Gal4 protein, as well as the persistence of RNAi effected by the double-stranded RNA product of GFP-IR-I. In one quantitative analysis in zebrafish, *gal4* mRNA was found to have very low stability, while the protein could still be detected around 13h after a short induction of its expression (Scheer and Campos-Ortega, 1999). The endpoint question of the resulting RNAi efficiency across time remains to be determined. If indeed RNAi efficiency traces the expression of *btl*, the peak during early and mid tracheogenesis could be part of the reason why in my screen many more Rabs were associated with defects of dorsal branch anatomy than with TC morphology. Phenotypes of dorsal branch anatomy should be consequences of defects during the embryonic process of tip cell specification, which occurs around the stages where *btl* expression peaks. TC morphogenesis on the other hand takes place during the larval stages, with around 50% of branches growing only during the third larval stage (JayaNandanan et al., 2014). The low discovery of TC defects associated with Rabs could therefore be in part due to low RNAi efficiency from the end of embryogenesis onward, stemming from a lower induction of *btl*-Gal4 expression.

5.2.3 Lack of correlation between Rab expression and knockdown phenotype

Regardless of the efficiency of YRab-gfpIR across space and time, its expression should be comparable in all YRab-gfpIR experiments. Therefore, all YRabs in my screen were subject to the same perturbation, and the observed results are quantitatively comparable for the purpose of understanding the relevance of Rabs to TC morphogenesis. However, the different YRabs themselves were expressed at different levels by TCs. The relationship between RNAi expression, tagged gene expression and the resulting knockdown efficiency, i.e. percentage reduction of tagged gene product, is not known and could not be determined from my experiments because even with the most detectable YRab (YRab1), YRab-gfpIR reduced the protein to undetectable levels. Intuitively, one could expect that the same level of RNAi expression would result in a higher knockdown efficiency in case of a YRab with very low endogenous expression. This is contradicted by a comparison for example of YRab-gfpIR for Rab1, Rab6 and Rab11, all of which are highly expressed by TCs. The defects caused by the indirect knockdown of YRab6 resulted in one of the most penetrant and severe phenotypes in the screen, while neither YRab1 nor YRab11 were associated with any defects at all. Conversely, the expression of Rab8 is much lower than any of these three, and yet the indirect knockdown of YRab8 resulted in the second-most penetrant phenotype in the screen. This indicates that the present data cannot support any argument regarding the quantitative connections between Gal4 expressivity, RNAi efficiency and phenotype severity. The reason for this is probably the unique functions of the different Rabs, and the resulting differences in the knockdown efficiency that would be required to elicit any defects in morphogenesis. Consequently, there is also no quantitative basis to estimate which of the negatives returned by the screen may be false negatives. Reasoning from the notion that cells express proteins they require, one could recommend Rab40, Rab39, as well as Rab26 and Rab32 as candidates for further study.

5.2.4 Involvement of Rabs in dorsal branch morphogenesis

The YRab-gfpIR screen returned a substantial number of Rabs as required for proper morphogenesis of the dorsal branch (DB). Among these are as of yet uncharacterised genes such as RabX5 and Rab19, but also well-known members of the family such as Rab7 and Rab11. Compared to TC morphogenesis, the developmental processes that might underly the anatomical defects observed here are substantially better understood. It is therefore possible to suggest causative mechanisms, all of which take place during embryogenesis. Given that Rabs are involved in membrane trafficking, the primary suspect is in most cases the trafficking of signal receptors involved in cell fate specification, such as Btl (FGF signalling), Notch, Thick Veins (DPP signalling) or Frizzled (WNT signalling).

The most prevalent abnormality was an increased number of TCs. There are three steps in DB morphogenesis during which the causative defect could occur; firstly the specification from tracheal pit cells to DB cells, secondly the selection of tip cells from the DB group and thirdly the fate refinement between the two tip cells into terminal and fusion cell (Hayashi and Kondo, 2018). I never observed more than 5 TCs on an individual DB, so while it is possible that defects occurred at the first stage, none of my observations required this. The second step, tip cell selection, normally results in two tip cells that actively migrate dorsally and pull the remaining DB cells along. Therefore, in cases where a single DB had more than two TCs, there must be a defect in this step, resulting in an excess specification of tip cells. This applies primarily to Rab19, where individual DBs often carried three or more TCs. If a defect only occurred in the last step where tip cells reciprocally assign the terminal and fusion cell fate, the result would be two TCs and a missing fusion cell. The Additional TC would therefore be accompanied by an Unfused DB. This was likely the case in knockdown of Rab7, Rab19 and Rab32. These were also the only Rabs that had increased frequencies of Misguided TCs, and all three also presented frequent Unfused DBs. All of these abnormalities could result from the same defect in tip cell specification - if both tip cells become TCs, the excess TC is more likely to mismigrate (Kato et al., 2004). The configuration of DBs that had a Misguided TC were consistent with this notion. Usually, the Misguided TC was simultaneously an Additional TC, and the DB was unfused. In previous work, this constellation was induced by inhibiting Wingless signalling (Kato et al., 2004), suggesting that Rab7, Rab19 and Rab32 may be important for trafficking Wingless receptors. Alternatively, excess activity of Btl could also specify additional TCs at the expense of fusion cells (Ghabrial and Krasnow, 2006; Lebreton and Casanova, 2016; Sutherland et al., 1996). Several Rab knockdowns (Rab4, Rab11, Rab14, Rab23, Rab26) only caused Additional TCs, and the penetrance was quite mild compared to Rab7 or Rab19. In these cases, most likely the fine-tuning of tip cell selection is disturbed and one or two additional cells become tip cells. This could reflect lowered Notch signalling, perhaps resulting from impaired secretion of Delta as has previously been associated with a lack of Rab11 in Notch-mediated lateral inhibition (Charng et al., 2014). Subsequently, Wingless signalling would select one fusion cell in these cases, and the remaining tip cells become TCs by default.

The Unfused DB abnormality could result from an absent fusion cell, but also any defect in the fusion process itself would cause this. My observations of maternal contribution in Rab19 and Rab7 provide suggestions as to the two mechanism's relative contributions. In Rab19 knockdown, the number of Additional TCs but not the number of Unfused DBs was affected by maternal contribution. Unfused DBs in Rab19 knockdown are therefore likely due primarily to fate misspecification. In contrast, in Rab7 knockdown the number of Additional TCs was independent of maternal contribution, but the number of Unfused DBs was affected by it. Rab7 is already known to be involved in the fusion process itself (Caviglia et al., 2016), and the dependence of the process on maternal product in my experiment suggests that the fusion process is one of the main roles of Rab7 in the DB. However, the presence of all five types of DB abnormalities in Rab7 knockdown indicates that Rab7 has several functions besides its role in delivering secretory lysosomes during dorsal fusion.

Missing TCs were overall very rare, but they were the only abnormality for both RabX4 and RabX5 knockdown. An absence of the TC could arise from excessive Notch signalling during tip cell specification, resulting in only a single tip cell that then becomes a fusion cell due to Wg signalling. However, Notch overactivity also represses the fusion cell fate (Araujo and Casanova, 2011; Ikeya and Hayashi, 1999), and neither of the two Rabs had an increased frequency of Unfused DBs. Likewise, a reduction in Btl signalling could reduce the number of TCs, but should result in additional defects related to a pan-tracheal inhibition of FGF-induced chemotaxis. A phenotype characterised selectively by a loss of TCs is not congruent with any currently known membrane-associated mechanism during DB morphogenesis and has not been reported previously.

Rab27, Rab39 and Rab40 knockdowns shared the prevalence of Unfused DBs without concomittant increases in Additional TCs. This selectivity is a likely indicator of a defect in the fusion process rather than fate specification. Rab39 is already known to be involved in secretion into the newly forming fused lumen during this process (Caviglia et al., 2016). Rab27 likewise is part of known secretory pathways for example in immune cells (Fukuda, 2013). Indeed, one of its effectors regulating lysosome secretion in haematopoietic cells (Neeft et al., 2005) and platelets (Shirakawa et al., 2004) is Munc-13-4, the homologue of Staccato, which was identified along with Rab39 on secretory lysosomes in tracheal fusion cells (Caviglia et al., 2016). Rab27 is therefore a highly likely candidate for contributing to fusion along with Rab39. Rab40 also had an increased frequency of Missing TCs and therefore probably participates in other processes besides fusion.

Finally, the abnormality Misfused DB most likely involves a migratory defect, in which the prospective fusion cell transgresses the segment boundary. This requires breaking out of the migration grooves provided by the underlying muscle precursors (Franch-Marro and Casanova, 2000) and suggests an insensitivity to the guidance probably provided by the epidermal cells along which tracheal tip cells migrate (Kato et al., 2004; Le Droguen et al., 2015). The most intuitive explanation is that the respective Rabs (Rab7, Rab19, Rab27, Rab39, Rab40) are involved in trafficking a membrane-bound signalling molecule whose function involves direct cell-to-cell contact, such as integrins. However, which receptors mediate the contact between the DB and muscle, respectively epidermis, is not known. All Rabs that were associated with Misfused DBs also had a larger number of Unfused DBs, an expected relationship since any mismigrated DB is likely to not meet its stereotypical contralateral partner. However, there were many cases (50% of all Misfused DBs in controls) where a misfusion occurred between two DBs on the same side of the dorsal midline, but one or both DBs still also met their contralateral partners and established fusions with them. I did not test whether such cases involved excess fusion cells, or whether individual fusion cells are competent to perform multiple fusions. However, in these cases, only rarely were the misfused DBs lacking their TC. To obtain excess fusion cells, there would thus first need to be an excess tip cell, and this should also make Additional TCs more likely to occur. For Rab7 and Rab19, Additional TCs were also frequent. However, Rab27, Rab39 and Rab40 were not associated with excess TCs. I therefore consider it more likely that at least in these three cases, individual fusion cells established multiple anastomoses with different partners; a previously unknown competence.

5.3 Rab-mediated membrane trafficking in terminal cells

5.3.1 An apical secretion pathway from ER to secretory endosomes

The YRab-gfpIR screen showed that Rab2, Rab6, Rab8 and Rab10 are required for proper TC tube morphogenesis and interfering with the expression of these Rabs causes defects in its formation. Out of these four, Rab2, Rab6 and Rab10 were associated with similar types of defects in the organisation of the apical extracellular matrix (aECM) in the lumen of the subcellular tube. The defects associated with Rab8 were markedly different and did not involve an abnormality of the aECM. Instead, the control of growth and branching of the tube appeared defective since the main tube within some branches was enveloped by additional small tubules. By far the most penetrant phenotypes were those associated with Rab6 and Rab8, followed by Rab2 and, with very low penetrance, Rab10.

To confirm my suspicion that more Rabs were important for TC morphogenesis than suggested by the screen, I performed mutant analyses for the most highly expressed Rabs, Rab1, Rab7 and Rab11, using the method known as Mosaic Analysis with a Repressible Cell Marker (Lee and Luo, 2001) to generate homozygous *rab* mutant TCs within heterozygous mutant animals. This revealed severe defects associated with all three mutants, although TCs mutant for *rab7* and *rab11* showed considerable phenotypic variability ranging from almost normal phenotypes to entirely degenerate. There are potential confounding factors in this approach that could contribute to the observed defects and phenotypic variability. Firstly, TCs may not be fully deficient for a *rab* even using mutants. Besides the possibility of maternal contribution, in MARCM cells can additionally inherit gene products from their progenitor cell prior to recombination of the mutant chromosome with the homologous arm carrying a wildtype allele. It is in principle impossible to guarantee the absence of any protein, and some of the variability in mutant phenotypes could stem from inherited gene products. To the extent that this was the case, the observed defects would have been less severe than in a TC fully deficient in the *rab*. However, it is also possible that some TCs manifested more severe defects than caused by the *rab* loss-of-function due to additional unspecific deficiencies. Firstly, the presence of transgenic insertions in the genome commonly impedes survival of animals regardless of the type of inserted sequence. MARCM animals carry several transgenic insertions related to the method, including a construct for expression of Flippase as well as constructs containing its recognition targets (FRT), *btl*-Gal4, the Gal4-repressor Gal80, and UAS-GFP. These unspecific transgenic burdens could exacerbate stress caused by the *rab* mutation and further impede TC morphogenesis. Secondly, the mutant chromosome may carry additional deleterious mutations elsewhere on the arm that is exchanged to generate homozygous mutant clones. All three rab mutant alleles used here were either P-element insertions (*rab1*^{S147213} and *rab11*^{j2D1}) or generated by imprecise excision of a P-element (*rab7*^{d1}). This eliminates at least the common issue of additional lesions associated with chemically induced mutations, but instead adds the possibility of the insertion, respectively deletion, disrupting regulatory sequences of other genes in addition to the *rab* gene located at the insertion site. Furthermore, both *rab1*^{S147213} and *rab11*^{j2D1} are insertions generated in 1997 (Deák et al., 1997), and *rab7*^{d1} was derived from an insertion generated in the same project (Hegedűs et al., 2016). The chromosomes have therefore undergone many generations of stock maintenance over a balancer, which causes accumulation of viability-reducing mutations over time (Keightley, 1996). These could at the same time non-specifically increase the severity of *rab* mutant phenotypes. Further experiments using specific RNAi constructs or other mutant alleles could corroborate the phenotypes observed for the mutants tested here.

The MARCM experiments showed that YRab-gfpIR induces a weaker loss-of-function than a null mutation in the same gene. My alternative hypothesis for false negatives in the YRab-gfpIR screen was functional redundancy between Rabs. This was mainly inspired by a suggestion from a collaborator that Rab11 and Rab35 may need to be eliminated in combination to elicit a loss-of-function phenotype, which was in turn based on their experiments in accessory glands (M. Brankatschk, personal communication). I selected three Rabs which might interact with Rab11 and tested a combined YRab-gfpIR against each pair. Rab4 was selected because like Rab11, it is associated with endosomal recycling (Mizuno-Yamasaki et al., 2012). Rab35 was selected primarily on the above-mentioned personal recommendation. Rab10 was selected because a previous study suggested that Rab10 and Rab11 function redundantly in TCs (Jones et al., 2014). The preceding MARCM experiments for *rab11* associated a loss of *rab11* with the same aECM defect as seen during the YRab-gfpIR screen for Rab2, Rab6 and Rab10. TCs in YRab11-gfpIR larvae never had this defect, but it manifested in a small subset of TCs in combined YRab-gfpIR against Rab4 and Rab11, as well as Rab11 and Rab35. This suggests that in the single YRab11-gfpIR, either a residual amount of Rab11 protein can provide sufficient function to maintain a normal phenotype, or other genes that can compensate for its loss are upregulated. However, when additionally interfering with Rab4 or Rab35, some TCs are not able to form a proper aECM, indicating a genetic interaction between Rab11 and Rab4, respectively Rab35. Since YRab-gfpIR presents only a partial knockdown and the phenotype was synergistic, the nature of this interaction cannot be inferred from these experiments alone but will be further discussed below. The presence of the same type of defect in YRab-gfpIR against Rab10 suggests that a partial Rab10 loss-of-function is sufficient to cause this defect, albeit very infrequently. The defect's absence in the combined experiment targeting YRab10 and YRab11 therefore indicates that additionally interfering with Rab11 allows aECM formation to proceed properly. While again the exact relationship between Rab10 and Rab11 cannot be inferred from this, the results stand in contradiction to the previous suggestion that the two function redundantly. In this case, one would have expected an additive phenotype in the combined knockdown. This discrepancy is most likely due to the method used in the cited study, namely the Gal4-induced expression of putative constitutively inactive Rab mutants. These variants bear a mutation in a conserved residue of the GTP-binding pocket (Zhang et al., 2007) and are commonly referred to as dominant-negative. This nomenclature may be misleading, because only for few of the mutants a dominant-negative mode of action has been demonstrated. For most, including Rab10 and Rab11, it can currently only be assumed that the mutant variants are indeed GTP-binding defective, that they are inactive as a consequence, and that they compete with their wildtype counterpart when transgenically overexpressed in a way that is equivalent to a loss-of-function. The experiments conducted here suggest that this is not the case for Rab10 and Rab11 since the additive phenotype observed using these mutants diverged from the rescue of the Rab10 phenotype that I observed in a combined indirect knockdown.

Taking results from both the YRab-gfpIR screen and the follow-up experiments together, the aECM defect that I named "asymmetric autofluorescence" is associated with Rabs throughout the endomembrane system. Rab1 and Rab2 are associated with the transition from endoplasmatic reticulum to Golgi (Stenmark, 2009). Rab6 is associated with trans-Golgi compartments and post-Golgi vesicles. Rab11 is associated with recycling endosomes and involved in polarised trafficking of secreted cargos from Golgi. Rab10, Rab4 and Rab35 are associated with the transport of endosomes to the plasma membrane. Rab7 is canonically associated with the maturation from early endosomes to late endosomes and lysosomes, but has recently been shown to also coordinate a new type of secretory lysosome in tracheal fusion cells (Caviglia et al., 2016). All of these Rabs are associated with anterograde trafficking, i.e. secretion. The best explanation for the similar phenotypic manifestation of their loss-of-function is therefore a shared cargo that passes through membrane compartments governed by the respective Rabs along its secretion route. This is also consistent with the reduced penetrance of the defect with endosomal Rabs, which suggests that this cargo is trafficked through multiple endosomal routes post-Golgi. To identify what the cargo might be, the nature of the defect can provide directions. The appearance of the autofluorescence in these TCs suggests a disorganisation of the aECM. Promising genes to test would therefore be membrane-bound or secreted structural proteins.

5.3.2 A Rab8-mediated endosomal trafficking route related to tube morphogenesis

My original interest had been in the determination of subcellular tube branching and the regulation of its growth. Following the screen, I therefore focussed my efforts on the only candidate that produced a highly penetrant defect related to these mechanisms, Rab8. This Rab has been associated with *de novo* apicobasal polarisation and lumen formation in 3D cell culture (Bryant et al., 2010), some cases of microvillous inclusion disease, whereby mammalian intestinal cells retain large vacuoles of maturely shaped apical membrane in the cytoplasm (Sato et al., 2007; Vogel et al., 2017), as well as recycling and secretory trafficking in cultured cells without apicobasal polarity (Grigoriev et al., 2011; Peränen, 2011; Shibata et al., 2016). Out of these known cases, the process with the highest similarity to subcellular tube formation in TCs is represented by 3D cultured canine kidney cells that also form a lumen (albeit multicellular) and enlarge their apical domains. However, the loss-of-function phenotype in TCs stands in direct contradiction to a conservation of Rab8 function between this epithelial cell type and TCs. Perturbation of Rab8 in cultured epithelia is associated with disruption of cell polarity (Henry and Sheff, 2008), and overexpressed Rab8 in 3D-cultured epithelia can rescue some mutations that cause a failure to enlarge the apical domain and expand a lumen (Chou et al., 2016). In TCs, the loss of Rab8 instead caused the formation of small tubules around the proper tube, some of which were also gas-filled. This should indicate a defect of the opposite kind, an excessive generation of apical membrane as well as excess lumen formation. None of the known functions of Rab8 in other cell types forms consistent parallels to such a phenotype, and I therefore characterised Rab8 in TCs under the assumption that its function in this cell type is unique.

I first explored the relationship between Rab8-mediated trafficking and the putative apical secretory route mediated by Rab1, 2, 6 and several endosomal Rabs as described above. To test their interaction, I performed an experiment similar to mutational epistasis using RNAi constructs against Rab6 and Rab8. Both constructs, when expressed individually, reproduced the phenotypes observed with indirect YRab-gfpIR knockdown for YRab6 and YRab8. TCs co-expressing both RNAi constructs showed an almost complete suppression of the phenotype associated with Rab8, and had phenotypes similar to TCs with only Rab6 knockdown. There are two constellations of the interaction between Rab6 and Rab8 that would be consistent with this. First, the function of Rab8 could be to inhibit Rab6 activity. In this case, the *rab8*-RNAi phenotype is the result of excess Rab6 activity, and the *rab6*-RNAi phenotype is the result of a lack of Rab6 activity. Consequently, in the combined knockdown, the phenotype that manifests is that of a lack of Rab6 activity. This would require that Rab8 performs no function besides inhibiting Rab6, since otherwise the additional functions of Rab8 should be reflected in the *rab8*-RNAi phenotype and these components should still manifest in the combined knockdown. The second possibility is that Rab6 is required for the function of Rab8. In this case, the *rab8*-RNAi phenotype represents a lack of Rab8, and the *rab6*-RNAi phenotype represents a lack of both Rab6 activity and Rab8 activity because the latter depends on the former. Therefore, the combined knockdown is identical to the single *rab6*-RNAi. I consider it more likely that the second possibility is the case. The role of Rab6 in maintaining a functioning Golgi apparatus and secretion is conserved, and Rab8 localised primarily to endosomes, but also to a lesser extent to Golgi membranes labelled by Rab6. The respective phenotypes could thus be interpreted as follows: with *rab6*-RNAi, the Golgi apparatus and consequently most secretion is defective, and with *rab8*-RNAi, an unknown endosomal trafficking route that transports cargo originating from the Golgi is defective. In the combined knockdown, secretion overall would still be malfunctioning and therefore the deficiency in an endosomal route downstream of Golgi-dependent secretion does not cause additional morphological defects.

What precisely might the function of this Rab8-mediated trafficking route be? I was not able to definitively answer this question, and part of this is that Rab8 might fulfill more than one function. However, my results suggest a model that is consistent with known functions of human Rab8A and unifies its subcellular localisation, the dynamic behaviour observed of Rab8-labelled structures, as well as the TC phenotype associated with its knockdown. The interpretation described above of the epistasis between *rab6* and *rab8* suggests that membrane compartments governed by Rab8 receive material from Rab6 compartments, which are most likely the *trans*-Golgi network itself or vesicles derived from it. This suggests that Rab8 operates on secretory cargo, but does not simply forward the same putative apically secreted product(s) whose absence is responsible for the aECM defects in *rab6*-RNAi. Rab8 primarily localised to endosomal recycling compartments marked by Rab11, as well as to a lesser extent Golgi membranes. This suggests that the secretory pathway that Rab8 operates on is recycling-endosome-dependent secretion, a prominent secretory pathway in many cell types (Stenmark, 2009). Mammalian Rab8A has indeed been associated with the sorting of basal-directed cargoes at the recycling endosome in cultured canine kidney cells (Henry and Sheff, 2008). My experiments also show that Rab8 cooperates with Stratum (Strat) in TCs. The Rab8/Strat complex has previously been shown to prevent the apical secretion of basal-directed secretion products in *Drosophila*, specifically Collagen in cells of the follicular epithelium (Devergne et al., 2017) and a trafficking partner of Notch, Sanpodo, in sensory organ precursor cells (Bellec et al., 2018). In the latter case, Strat was also required for exporting Notch and Delta from the *trans*-Golgi network.

Bearing this literature context in mind, the function of the dynamic behaviour of Rab8-labelled structures that I observed can be connotated, although their identity remains unclear without further experiments. Their tubulating behaviour could be similar to the tubulation of Golgi membranes (Cluett et al., 1993) or could represent the formation of tubular recycling endosomes (Delevoye et al., 2014). However, their dynamic behaviour showed interactions selectively with the apical membrane, which could be a mechanism of apical delivery of secretory cargoes. In the context described above, the function of Rab8 on such compartments could thus be the retention of basally-destined cargoes during such apical interactions. To test this hypothesis, I perturbed Rab8 function and observed its effect on the localisation of an endogenously GFP-tagged Crumbs protein (Crb-GFP). Rab8 knockdown did not impede the apical delivery of Crb-GFP. In contrast, expressing a putative constitutively-active Rab8 mutant caused Crb-GFP to accummulate in cytoplasmic aggregates in addition to its apical enrichment, and in some TCs Crb-GFP was no longer apically enriched. Rab8 is thus not required to deliver Crb-GFP to the apical membrane, but its active form is capable of retaining Crb-GFP in the cytoplasm. These observations are consistent with a model where Rab8 functions at Golgi and endosomal membranes that interact with the apical membrane to prevent the apical secretion of basally-destined cargoes. The excess tubules that characterise Rab8 knockdown could thus be related to the erroneous apical secretion of some factor that induces branching of the apical membrane.

6. Conclusions and Perspective

The present thesis constitutes a comprehensive analysis of Rab-mediated membrane trafficking in the terminal cells (TCs) of the tracheal system in *Drosophila melanogaster*. In this work, I focussed on the subcellular tube that hollows the branches formed by TCs, partially because all known mechanisms related to membrane trafficking primarily impact the tube and only as a secondary consequence can impede the formation of branches (Best, 2018). Interpreting abnormal phenotypes elicited by genetic perturbations has been challenging in the past, because in many cases individual TCs form some branches with normal tube morphology, and others with abnormalities. In addition, phenotypic studies require definitions of normal and abnormal morphology that reflect meaningful biological processes, such as a pathway of molecular interactions. While in many tissues a sufficient definition can be reached intuitively, a systematic phenomic study was required to understand which morphological features are associated with different molecular functions in TCs. My work thus provides a valuable reference of TC phenotypes that should be considered normal, enriches our understanding of abnormal morphologies, and allows future work on the subcellular tube to proceed with clearer directions.

The main part of my thesis comprises a family-wide knockdown screen of Rab GTPases, executed using an indirect approach that has proven in recent studies to provide substantial benefits over specific RNAi with constructs targeting each screened gene's mRNA. By instead targeting the sequence of a knocked-in tag, false positives can reliably be eliminated, and positive hits can be interpreted with confidence. This approach, combined with supplementary mutant and double knockdown experiments, revealed a secretory pathway in TCs that spans from the endoplasmatic reticulum through Golgi to endosomes and requires, to different extents, the Rabs 1, 2, 4, 6, 7, 10, 11 and 35. It further implicated several other Rabs not in TC morphogenesis but in the formation of the dorsal branch. Of particular interest could be Rab19 and RabX5, neither of which have been characterised in any biological system. In this screen, they were the Rabs with the most penetrant dorsal branch phenotypes.

Lastly, I characterised the function of Rab8 in TCs, since this was the only Rab whose phenotype in the knockdown screen suggested a role in subcellular tube shaping and branching. By conducting an RNAi-based epistasis experiment, I was able to show that Rab8 functions downstream of the Golgi apparatus and therefore most likely traffics Golgi-derived cargoes. Its subcellular localisation and the dynamics of Rab8-enriched structures in the cytoplasm were consistent with this hypothesis, revealing a primarily recycling endosomal localisation, partial Golgi association, and a preference for enriching at the apical membrane or on structures that interact with it. Further to this, I found a conserved interaction with Stratum, a putative Rab chaperone or activator, which suggested a role in the sorting of polarity-specific secretory cargoes. The ability of a constitutively-active Rab8 mutant to interfere with the apical delivery of Crumbs was consistent with this hypothesis. Altogether, these suggested a function as seen in other epithelia, that Rab8 in TCs accompanies secretory cargo from the *trans*-Golgi network, through recycling endosomes and to the apical membrane, ensuring that basal-directed cargoes are retained and not secreted apically. The excessive growth of tubules that characterises a loss of Rab8 is thus presumably caused by the erroneous apical secretion of an unknown factor. It will be interesting in the future to identify which factor is capable of inducing this reshaping of the apical membrane.

7. References

Affolter, M., Caussinus, E., 2008. Tracheal branching morphogenesis in Drosophila: new insights into cell behaviour and organ architecture. Development 135, 2055–2064. https://doi.org/10.1242/dev.014498

Aivazian, D., Serrano, R.L., Pfeffer, S., 2006. TIP47 is a key effector for Rab9 localization. J. Cell Biol. 173, 917–926. https://doi.org/10.1083/jcb.200510010

Alberts, B., Johnson, A., Lewis, J., Raff, M., Roberts, K., Walter, P., 2002. Molecular Biology of the Cell, 4th ed. ed. New York.

Aldaz, S., Escudero, L.M., 2010. Imaginal discs. Curr. Biol. R429–R431.

Araujo, S.J., Casanova, J., 2011. Sequoia establishes tip-cell number in Drosophila trachea by regulating FGF levels. J. Cell Sci. 124, 2335–2340. https://doi.org/10.1242/jcs.085613

Baer, M.M., Bilstein, A., Leptin, M., 2007. A clonal genetic screen for mutants causing defects in larval tracheal morphogenesis in Drosophila. Genetics 176, 2279–91. https://doi.org/10.1534/genetics.107.074088

Bakker, J., Spits, M., Neefjes, J., Berlin, I., 2017. The EGFR odyssey – from activation to destruction in space and time. J. Cell Sci. 130, 4087–4096. https://doi.org/10.1242/jcs.209197

Bates, M., Martinez-Arias, A., 1993. The Development of Drosophila melanogaster. Cold Spring Harbor Laboratory, New York.

Bellec, K., Gicquel, I., Le Borgne, R., 2018. Stratum recruits Rab8 at Golgi exit sites to regulate the basolateral sorting of Notch and Sanpodo. Development 145, dev163469. https://doi.org/10.1242/dev.163469

Best, B.T., 2018. Single-cell branching morphogenesis in the Drosophila trachea. Dev. Biol. In press. https://doi.org/10.1016/j.ydbio.2018.12.001

Bochdanovits, Z., De Jong, G., 2003. Temperature dependent larval resource allocation shaping adult body size in Drosophila melanogaster. J. Evol. Biol. 16, 1159–67.

Booker, M., Samsonova, A.A., Kwon, Y., Flockhart, I., Mohr, S.E., Perrimon, N., 2011. False negative rates in Drosophila cell-based RNAi screens: a case study. BMC Genomics 12, 50. https://doi.org/10.1186/1471-2164-12-50

Bravo-Cordero, J.J., Cordani, M., Soriano, S.F., Díez, B., Muñoz-Agudo, C., Casanova-Acebes, M., Boullosa, C., Guadamillas, M.C., Ezkurdia, I., González-Pisano, D., del Pozo, M.A., Montoya, M.C., 2016. A novel high-content analysis tool reveals Rab8-driven cytoskeletal reorganization through Rho GTPases, calpain and MT1-MMP. J. Cell Sci. 129, 1734–1749. https://doi.org/10.1242/jcs.174920

Brown, J.B., Boley, N., Eisman, R., May, G.E., Stoiber, M.H., Duff, M.O., Booth, B.W., Wen, J., Park, S., Suzuki, A.M., Wan, K.H., Yu, C., Zhang, D., Carlson, J.W., Cherbas, L., Eads, B.D., Miller, D., Mockaitis, K., Roberts, J., Davis, C.A., Frise, E., Hammonds, A.S., Olson, S., Shenker, S., Sturgill, D., Samsonova, A.A., Weiszmann, R., Robinson, G., Hernandez, J., Andrews, J., Bickel, P.J., Carninci, P., Cherbas, P., Gingeras, T.R., Hoskins, R.A., Kaufman, T.C., Lai, E.C., Oliver, B., Perrimon, N., Graveley, B.R., Celniker, S.E., 2014. Diversity and dynamics of the Drosophila transcriptome. Nature 512, 393–399. https://doi.org/10.1038/nature12962

Brown, S., Hu, N., Hombria, J.C., 2001. Identification of the first invertebrate interleukin JAK/STAT receptor, the Drosophila gene domeless. Curr. Biol. 11, 1700–1705.

Bryant, D.M., Datta, A., Rodríguez-Fraticelli, A.E., Peränen, J., Martín-Belmonte, F., Mostov, K.E., 2010. A molecular network for de novo generation of the apical surface and lumen. Nat. Cell Biol. 12, 1035–45. https://doi.org/10.1038/ncb2106

Cabernard, C., Neumann, M., Affolter, M., 2004. Cellular and molecular mechanisms involved in branching morphogenesis of the Drosophila tracheal system. J. Appl. Physiol. 97, 2347–2353. https://doi.org/10.1152/japplphysiol.00435.2004

Campa, C.C., Hirsch, E., 2017. Rab11 and phosphoinositides: A synergy of signal transducers in the control of vesicular trafficking. Adv. Biol. Regul. 63, 132–139. https://doi.org/10.1016/j.jbior.2016.09.002

Caussinus, E., Colombelli, J., Affolter, M., 2008. Tip-cell migration controls stalk-cell intercalation during Drosophila tracheal tube elongation. Curr. Biol. 18, 1727–34. https://doi.org/10.1016/j.cub.2008.10.062

Caussinus, E., Kanca, O., Affolter, M., 2012. Fluorescent fusion protein knockout mediated by anti-GFP nanobody. Nat. Struct. Mol. Biol. 19, 117–121. https://doi.org/10.1038/nsmb.2180

Caviglia, S., Brankatschk, M., Fischer, E.J., Eaton, S., Luschnig, S., 2016. Staccato/Unc-13-4 controls secretory lysosome-mediated lumen fusion during epithelial tube anastomosis. Nat. Cell Biol. 18, 727–39. https://doi.org/10.1038/ncb3374

Centanin, L., Dekanty, A., Romero, N., Irisarri, M., Gorr, T.A., Wappner, P., 2008. Cell autonomy of HIF effects in Drosophila: tracheal cells sense hypoxia and induce terminal branch sprouting. Dev. Cell 14, 547–58. https://doi.org/10.1016/j.devcel.2008.01.020

Charng, W.-L., Yamamoto, S., Jaiswal, M., Bayat, V., Xiong, B., Zhang, K., Sandoval, H., David, G., Gibbs, S., Lu, H.-C., Chen, K., Giagtzoglou, N., Bellen, H.J., 2014. Drosophila Tempura, a Novel Protein Prenyltransferase α Subunit, Regulates Notch Signaling Via Rab1 and Rab11. PLoS Biol. 12, e1001777. https://doi.org/10.1371/journal.pbio.1001777

Chen, C.K., Kühnlein, R.P., Eulenberg, K.G., Vincent, S., Affolter, M., Schuh, R., 1998. The transcription factors KNIRPS and KNIRPS RELATED control cell migration and branch morphogenesis during Drosophila tracheal development. Development 125, 4959–68.

Chen, J., Call, G.B., Beyer, E., Bui, C., Cespedes, A., Chan, A., Chan, J., Chan, S., Chhabra, A., Dang, P., Deravanesian, A., Hermogeno, B., Jen, J., Kim, E., Lee, E., Lewis, G., Marshall, J., Regalia, K., Shadpour, F., Shemmassian, A., Spivey, K., Wells, M., Wu, J., Yamauchi, Y., Yavari, A., Abrams, A., Abramson, A., Amado, L., Anderson, J., Bashour, K., Bibikova, E., Bookatz, A., Brewer, S., Buu, N., Calvillo, S., Cao, J., Chang, A., Chang, D., Chang, Y., Chen, Y., Choi, J., Chou, J., Datta, S., Davarifar, A., Desai, P., Fabrikant, J., Farnad, S., Fu, K., Garcia, E., Garrone, N., Gasparyan, S., Gayda, P., Goffstein, C., Gonzalez, C., Guirguis, M., Hassid, R., Hong, A., Hong, J., Hovestreydt, L., Hu, C., Jamshidian, F., Kahen, K., Kao, L., Kelley, M., Kho, T., Kim, S., Kim, Y., Kirkpatrick, B., Kohan, E., Kwak, R., Langenbacher, A., Laxamana, S., Lee, C., Lee, J., Lee, S.-Y., Lee, T.H.S., Lee, T., Lezcano, S., Lin, H., Lin, P., Luu, J., Luu, T., Marrs, W., Marsh, E., Min, S., Minasian, T., Misra, A., Morimoto, M., Moshfegh, Y., Murray, J., Nguyen, C., Nguyen, K., Nodado, E., O'Donahue, A., Onugha, N., Orjiakor, N., Padhiar, B., Pavel-Dinu, M., Pavlenko, A., Paz, E., Phaklides, S., Pham, L., Poulose, P., Powell, R., Pusic, A., Ramola, D., Ribbens, M., Rifai, B., Rosselli, D., Saakyan, M., Saarikoski, P., Segura, M., Singh, R., Singh, V., Skinner, E., Solomin, D., Soneji, K., Stageberg, E., Stavchanskiy, M., Tekchandani, L., Thai, L., Thiyanaratnam, J., Tong, M., Toor, A., Tovar, S., Trangsrud, K., Tsang, W.-Y., Uemura, M., Unkovic, M., Vollmer, E., Weiss, E., Wood, D., Wu, S., Wu, W., Xu, Q., Yackle, K., Yarosh, W., Yee, L., Yen, G., Alkin, G., Go, S., Huff, D.M., Minye, H., Paul, E., Villarasa, N., Milchanowski, A., Banerjee, U., 2005. Discovery-Based Science Education: Functional Genomic Dissection in Drosophila by Undergraduate Researchers. PLoS Biol. 3, e59. https://doi.org/10.1371/journal.pbio.0030059

Chihara, T., Hayashi, S., 2000. Control of tracheal tubulogenesis by Wingless signaling. Development 127, 4433–42.

Chou, S.-Y., Hsu, K.-S., Otsu, W., Hsu, Y.-C., Luo, Y.-C., Yeh, C., Shehab, S.S., Chen, J., Shieh, V., He, G., Marean, M.B., Felsen, D., Ding, A., Poppas, D.P., Chuang, J.-Z., Sung, C.-H., 2016. CLIC4 regulates apical exocytosis and renal tube luminogenesis through retromer- and actin-mediated endocytic trafficking. Nat. Commun. 7, 10412. https://doi.org/10.1038/ncomms10412

Cluett, E.B., Wood, S.A., Banta, M., Brown, W.J., 1993. Tubulation of Golgi membranes in vivo and in vitro in the absence of brefeldin A. J. Cell Biol. 120, 15–24.

Coen, B.A., Jennrich, R.I., 2005. Gradient Projection Algorithms and Software for Arbitrary Rotation Criteria in Factor Analysis. Educ. Psychol. Meas. 65, 676–696. https://doi.org/10.1177/0013164404272507

Court, H., Ahearn, I.M., Amoyel, M., Bach, E.A., Philips, M.R., 2017. Regulation of NOTCH signaling by RAB7 and RAB8 requires carboxyl methylation by ICMT. J. Cell Biol. 216, 4165–4182. https://doi.org/10.1083/jcb.201701053

Deák, P., Omar, M.M., Saunders, R.D., Pál, M., Komonyi, O., Szidonya, J., Maróy, P., Zhang, Y., Ashburner, M., Benos, P., Savakis, C., Siden-Kiamos, I., Louis, C., Bolshakov, V.N., Kafatos, F.C., Madueno, E., Modolell, J., Glover, D.M., 1997. P-element insertion alleles of essential genes on the third chromosome of Drosophila melanogaster: correlation of physical and cytogenetic maps in chromosomal region 86E-87F. Genetics 147, 1697–722.

Del Signore, S.J., Biber, S.A., Lehmann, K.S., Heimler, S.R., Rosenfeld, B.H., Eskin, T.L., Sweeney, S.T., Rodal, A.A., 2017. dOCRL maintains immune cell quiescence by regulating endosomal traffic. PLOS Genet. 13, e1007052. https://doi.org/10.1371/journal.pgen.1007052

Delevoye, C., Miserey-Lenkei, S., Montagnac, G., Gilles-Marsens, F., Paul-Gilloteaux, P., Giordano, F., Waharte, F., Marks, M.S., Goud, B., Raposo, G., 2014.

Recycling Endosome Tubule Morphogenesis from Sorting Endosomes Requires the Kinesin Motor KIF13A. Cell Rep. 6, 445–454. https://doi.org/10.1016/j.celrep.2014.01.002

Devergne, O., Sun, G.H., Schüpbach, T., 2017. Stratum, a Homolog of the Human GEF Mss4, Partnered with Rab8, Controls the Basal Restriction of Basement Membrane Proteins in Epithelial Cells. Cell Rep. 18, 1831–1839. https://doi.org/10.1016/j.celrep.2017.02.002

Dong, B., Kakihara, K., Otani, T., Wada, H., Hayashi, S., 2013. Rab9 and retromer regulate retrograde trafficking of luminal protein required for epithelial tube length control. Nat. Commun. 4, 1358. https://doi.org/10.1038/ncomms2347

Du, L., Zhou, A., Patel, A., Rao, M., Anderson, K., Roy, S., 2017. Unique patterns of organization and migration of FGF-expressing cells during Drosophila morphogenesis. Dev. Biol. 427, 35–48. https://doi.org/10.1016/j.ydbio.2017.05.009

Dunst, S., Kazimiers, T., von Zadow, F., Jambor, H., Sagner, A., Brankatschk, B., Mahmoud, A., Spannl, S., Tomancak, P., Eaton, S., Brankatschk, M., 2015. Endogenously Tagged Rab Proteins: A Resource to Study Membrane Trafficking in Drosophila. Dev. Cell 33, 351–365. https://doi.org/10.1016/j.devcel.2015.03.022

Echeverri, C.J., Beachy, P.A., Baum, B., Boutros, M., Buchholz, F., Chanda, S.K., Downward, J., Ellenberg, J., Fraser, A.G., Hacohen, N., Hahn, W.C., Jackson, A.L., Kiger, A., Linsley, P.S., Lum, L., Ma, Y., Mathey-Prévôt, B., Root, D.E., Sabatini, D.M., Taipale, J., Perrimon, N., Bernards, R., 2006. Minimizing the risk of reporting false positives in large-scale RNAi screens. Nat. Methods 3, 777–779. https://doi.org/10.1038/nmeth1006-777

Franch-Marro, X., Casanova, J., 2002. spalt-induced specification of distinct dorsal and ventral domains is required for Drosophila tracheal patterning. Dev. Biol. 250, 374–382.

Franch-Marro, X., Casanova, J., 2000. The alternative migratory pathways of the Drosophila tracheal cells are associated with distinct subsets of mesodermal cells. Dev. Biol. 227, 80–90. https://doi.org/10.1006/dbio.2000.9890

Frazier, M.R., Woods, H.A., Harrison, J.F., 2001. Interactive Effects of Rearing Temperature and Oxygen on the Development of Drosophila melanogaster. Physiol. Biochem. Zool. 74, 641–650. https://doi.org/10.1086/322172

Fukuda, M., 2013. Rab27 Effectors, Pleiotropic Regulators in Secretory Pathways. Traffic 14, 949–963. https://doi.org/10.1111/tra.12083

Furbank, R.T., Tester, M., 2011. Phenomics – technologies to relieve the phenotyping bottleneck. Trends Plant Sci. 16, 635–644. https://doi.org/10.1016/j.tplants.2011.09.005

Gervais, L., Casanova, J., 2010. In vivo coupling of cell elongation and lumen formation in a single cell. Curr. Biol. 20, 359–66. https://doi.org/10.1016/j.cub.2009.12.043

Gervais, L., Lebreton, G., Casanova, J., 2012. The making of a fusion branch in the Drosophila trachea. Dev. Biol. 362, 187–193. https://doi.org/10.1016/j.ydbio.2011.11.018

Ghabrial, A., Luschnig, S., Metzstein, M.M., Krasnow, M.A., 2003. Branching morphogenesis of the Drosophila tracheal system. Annu. Rev. Cell Dev. Biol. 19, 623–47. https://doi.org/10.1146/annurev.cellbio.19.031403.160043

Ghabrial, A.S., Krasnow, M.A., 2006. Social interactions among epithelial cells during tracheal branching morphogenesis. Nature 441, 746–9. https://doi.org/10.1038/nature04829

Ghosh, S.M., Testa, N.D., Shingleton, A.W., 2013. Temperature-size rule is mediated by thermal plasticity of critical size in Drosophila melanogaster. Proc. R. Soc. B Biol. Sci. 280, 20130174–20130174. https://doi.org/10.1098/rspb.2013.0174

Glasheen, B.M., Robbins, R.M.R.M., Piette, C., Beitel, G.J., Page-McCaw, A., 2010. A matrix metalloproteinase mediates airway remodeling in Drosophila. Dev. Biol. 344, 772–783. https://doi.org/10.1016/j.ydbio.2010.05.504

Glazer, L., Shilo, B.Z., 1991. The Drosophila FGF-R homolog is expressed in the embryonic tracheal system and appears to be required for directed tracheal cell extension. Genes Dev. 5, 697–705.

Gorr, T.A., Gassmann, M., Wappner, P., 2006. Sensing and responding to hypoxia via HIF in model invertebrates. J. Insect Physiol. 52, 349–64. https://doi.org/10.1016/j.jinsphys.2006.01.002

Gould, J., 2016. Morpheus: Versatile matrix visualization and analysis software [WWW Document]. URL https://software.broadinstitute.org/morpheus/ (accessed 9.1.18).

Gramates, L.S., Marygold, S.J., Santos, G. Dos, Urbano, J.-M., Antonazzo, G., Matthews, B.B., Rey, A.J., Tabone, C.J., Crosby, M.A., Emmert, D.B., Falls, K., Goodman, J.L., Hu, Y., Ponting, L., Schroeder, A.J., Strelets, V.B., Thurmond, J., Zhou, P., the FlyBase Consortium, 2017. FlyBase at 25: looking to the future. Nucleic Acids Res. 45, D663–D671. https://doi.org/10.1093/nar/gkw1016

Green, E.W., Fedele, G., Giorgini, F., Kyriacou, C.P., 2014. A Drosophila RNAi collection is subject to dominant phenotypic effects. Nat. Methods 11, 222–223. https://doi.org/10.1038/nmeth.2856

Grigoriev, I., Yu, K.L., Martinez-Sanchez, E., Serra-Marques, A., Smal, I., Meijering, E., Demmers, J., Peränen, J., Pasterkamp, R.J., van der Sluijs, P., Hoogenraad, C.C., Akhmanova, A., 2011. Rab6, Rab8, and MICAL3 Cooperate in Controlling Docking and Fusion of Exocytotic Carriers. Curr. Biol. 21, 967–974. https://doi.org/10.1016/J.CUB.2011.04.030

Guha, A., Lin, L., Kornberg, T.B., 2008. Organ renewal and cell divisions by differentiated cells in Drosophila. Proc. Natl. Acad. Sci. U. S. A. 105, 10832–10836. https://doi.org/10.1073/pnas.0805111105

Guillemin, K., Williams, T., Krasnow, M.A., 2001. A nuclear lamin is required for cytoplasmic organization and egg polarity in Drosophila. Nat. Cell Biol. 3, 848–51. https://doi.org/10.1038/ncb0901-848

Gulbranson, D.R., Davis, E.M., Demmitt, B.A., Ouyang, Y., Ye, Y., Yu, H., Shen, J., 2017. RABIF/MSS4 is a Rab-stabilizing holdase chaperone required for GLUT4 exocytosis. Proc. Natl. Acad. Sci. 114, E8224–E8233. https://doi.org/10.1073/pnas.1712176114

Hartenstein, V., 1993. Atlas of Drosophila. Cold Spring Harbor Laboratory, New York.

Hayashi, S., Kondo, T., 2018. Development and Function of the Drosophila Tracheal System. Genetics 209, 367–380. https://doi.org/10.1534/genetics.117.300167

Hegedűs, K., Takáts, S., Boda, A., Jipa, A., Nagy, P., Varga, K., Kovács, A.L., Juhász, G., 2016. The Ccz1-Mon1-Rab7 module and Rab5 control distinct steps of autophagy. Mol. Biol. Cell 27, 3132–3142. https://doi.org/10.1091/mbc.E16-03-0205

Henry, L., Sheff, D.R., 2008. Rab8 regulates basolateral secretory, but not recycling, traffic at the recycling endosome. Mol. Biol. Cell 19, 2059–68. https://doi.org/10.1091/mbc.E07-09-0902

Hirosaki, K., Yamashita, T., Jin, H.-Y., Jimbow, K., Wada, I., 2002. Tyrosinase and Tyrosinase-Related Protein 1 Require Rab7 for Their Intracellular Transport. J. Invest. Dermatol. 119, 475–480. https://doi.org/10.1046/j.1523-1747.2002.01832.x

Ho, J., Tumkaya, T., Aryal, S., Choi, H., Claridge-Chang, A., 2018. Moving beyond P values: Everyday data analysis with estimation plots. bioRxiv 377978. https://doi.org/10.1101/377978

Holly, R.M., Mavor, L.M., Zuo, Z., Blankenship, J.T., 2015. A rapid, membrane-dependent pathway directs furrow formation through RalA in the early Drosophila embryo. Development 142, 2316–28. https://doi.org/10.1242/dev.120998

Horowitz, A., Simons, M., 2008. Branching morphogenesis. Circ. Res. 103, 784–795. https://doi.org/10.1161/CIRCRESAHA.108.181818

Huang, J., Zhou, W., Dong, W., Watson, A.M., Hong, Y., 2009. Directed, efficient, and versatile modifications of the Drosophila genome by genomic engineering. Proc. Natl. Acad. Sci. 106, 8284–8289. https://doi.org/10.1073/pnas.0900641106

Hutagalung, A.H., Novick, P.J., 2011. Role of Rab GTPases in Membrane Traffic and Cell Physiology. Physiol. Rev. 91, 119–149. https://doi.org/10.1152/physrev.00059.2009

Hyun, S., 2018. Body size regulation by maturation steroid hormones: a Drosophila perspective. Front. Zool. 15, 44. https://doi.org/10.1186/s12983-018-0290-9

Ikeya, T., Hayashi, S., 1999. Interplay of Notch and FGF signaling restricts cell fate and MAPK activation in the Drosophila trachea. Development 126, 4455–63.

Imam, F., Sutherland, D., Huang, W., Krasnow, M.A., 1999. stumps, a Drosophila gene required for fibroblast growth factor (FGF)-directed migrations of tracheal and mesodermal cells. Genetics 152, 307–18.

Isaac, D.D., Andrew, D.J., 1996. Tubulogenesis in Drosophila: a requirement for the trachealess gene product. Genes Dev. 10, 103–17.

Itzen, A., Pylypenko, O., Goody, R.S., Alexandrov, K., Rak, A., 2006. Nucleotide exchange via local protein unfolding—structure of Rab8 in complex with MSS4. EMBO J. 25, 1445–1455. https://doi.org/10.1038/sj.emboj.7601044

Iwanami, N., Nakamura, Y., Satoh, T., Liu, Z., Satoh, A.K., 2016. Rab6 Is Required for Multiple Apical Transport Pathways but Not the Basolateral Transport Pathway in

Drosophila Photoreceptors. PLOS Genet. 12, e1005828. https://doi.org/10.1371/journal.pgen.1005828

Jacomin, A.-C., Fauvarque, M.-O., Taillebourg, E., 2016. A functional endosomal pathway is necessary for lysosome biogenesis in Drosophila. BMC Cell Biol. 17, 36. https://doi.org/10.1186/s12860-016-0115-7

Jarecki, J., Johnson, E., Krasnow, M.A., 1999. Oxygen regulation of airway branching in Drosophila is mediated by branchless FGF. Cell 99, 211–220. https://doi.org/10.1016/S0092-8674(00)81652-9

JayaNandanan, N., Mathew, R., Leptin, M., 2014. Guidance of subcellular tubulogenesis by actin under the control of a synaptotagmin-like protein and Moesin. Nat. Commun. 5, 3036. https://doi.org/10.1038/ncomms4036

Jones, T.A., Metzstein, M.M., 2011. A novel function for the PAR complex in subcellular morphogenesis of tracheal terminal cells in Drosophila melanogaster. Genetics 189, 153–64. https://doi.org/10.1534/genetics.111.130351

Jones, T.A., Nikolova, L.S., Schjelderup, A., Metzstein, M.M., 2014. Exocyst-mediated membrane trafficking is required for branch outgrowth in Drosophila tracheal terminal cells. Dev. Biol. 390, 41–50. https://doi.org/10.1016/j.ydbio.2014.02.021

Kakanj, P., Moussian, B., Grönke, S., Bustos, V., Eming, S.A., Partridge, L., Leptin, M., 2016. Insulin and TOR signal in parallel through FOXO and S6K to promote epithelial wound healing. Nat. Commun. 7, 12972. https://doi.org/10.1038/ncomms12972

Kassambara, A., 2018. R package “ggpubr”: ‘ggplot2’ Based Publication Ready Plots.

Kassambara, A., Mundt, F., 2017. R package “factoextra”: Extract and Visualize the Results of Multivariate Data Analyses.

Kato, K., Chihara, T., Hayashi, S., 2004. Hedgehog and Decapentaplegic instruct polarized growth of cell extensions in the Drosophila trachea. Development 131, 5253–61. https://doi.org/10.1242/dev.01404

Keightley, P.D., 1996. Nature of deleterious mutation load in Drosophila. Genetics 144, 1993–9.

Kerman, B.E., Cheshire, A.M., Myat, M.M., Andrew, D.J., 2008. Ribbon modulates apical membrane during tube elongation through Crumbs and Moesin. Dev. Biol. 320, 278–288. https://doi.org/10.1016/j.ydbio.2008.05.541

Klämbt, C., Glazer, L., Shilo, B.Z., 1992. breathless, a Drosophila FGF receptor homolog, is essential for migration of tracheal and specific midline glial cells. Genes Dev. 6, 1668–78.

Klapholz, B., Brown, N.H., 2017. Talin – the master of integrin adhesions. J. Cell Sci. 130, 2435–2446. https://doi.org/10.1242/jcs.190991

Kondo, T., Hayashi, S., 2013. Mitotic cell rounding accelerates epithelial invagination. Nature 494, 125–129. https://doi.org/10.1038/nature11792

Kotini, M.P., Mäe, M.A., Belting, H.-G., Betsholtz, C., Affolter, M., 2018. Sprouting and anastomosis in the Drosophila trachea and the vertebrate vasculature: Similarities and differences in cell behaviour. Vascul. Pharmacol. https://doi.org/10.1016/j.vph.2018.11.002

Kühnlein, R.P., Frommer, G., Friedrich, M., Gonzalez-Gaitan, M., Weber, A., Wagner-Bernholz, J.F., Gehring, W.J., Jäckle, H., Schuh, R., 1994. spalt encodes an evolutionarily conserved zinc finger protein of novel structure which provides homeotic gene function in the head and tail region of the Drosophila embryo. EMBO J. 13, 168–79.

Le Droguen, P.-M., Claret, S., Guichet, A., Brodu, V., 2015. Microtubule-dependent apical restriction of recycling endosomes sustains adherens junctions during morphogenesis of the Drosophila tracheal system. Development 142, 363–374. https://doi.org/10.1242/dev.113472

Lebreton, G., Casanova, J., 2016. Ligand-binding and constitutive FGF receptors in single Drosophila tracheal cells: Implications for the role of FGF in collective migration. Dev. Dyn. 245, 372–378. https://doi.org/10.1002/dvdy.24345

Lee, J., Ye, Y., 2018. The Roles of Endo-Lysosomes in Unconventional Protein Secretion. Cells 7, 198. https://doi.org/10.3390/cells7110198

Lee, T., Luo, L., 2001. Mosaic analysis with a repressible cell marker (MARCM) for Drosophila neural development. Trends Neurosci. 24, 251–4.

Levi, B.P., Ghabrial, A.S., Krasnow, M.A., 2006. Drosophila talin and integrin genes are required for maintenance of tracheal terminal branches and luminal organization. Development 133, 2383–93. https://doi.org/10.1242/dev.02404

Li, Q., Gong, Z., 2015. Cold-sensing regulates Drosophila growth through insulin-producing cells. Nat. Commun. 6, 10083. https://doi.org/10.1038/ncomms10083

Lin, C.-Y., Hovhannisyan, V., Wu, J.-T., Lin, C.-W., Chen, J.-H., Lin, S.-J., Dong, C.-Y., 2008. Label-free imaging of Drosophila larva by multiphoton autofluorescence and second harmonic generation microscopy. J. Biomed. Opt. 13, 50502. https://doi.org/10.1117/1.2981817

Linneweber, G.A., Jacobson, J., Busch, K.E., Hudry, B., Christov, C.P., Dormann, D., Yuan, M., Otani, T., Knust, E., de Bono, M., Miguel-Aliaga, I., 2014. Neuronal control of metabolism through nutrient-dependent modulation of tracheal branching. Cell 156, 69–83. https://doi.org/10.1016/j.cell.2013.12.008

Liu, S., Storrie, B., 2015. How Rab Proteins Determine Golgi Structure, in: International Review of Cell and Molecular Biology. pp. 1–22. https://doi.org/10.1016/bs.ircmb.2014.12.002

Llimargas, M., 2000. Wingless and its signalling pathway have common and separable functions during tracheal development. Development 127, 4407–17.

Llimargas, M., Casanova, J., 1999. EGF signalling regulates cell invagination as well as cell migration during formation of tracheal system in Drosophila. Dev. Genes Evol. 209, 174–9.

Lu, H., Bilder, D., 2005. Endocytic control of epithelial polarity and proliferation in Drosophila. Nat. Cell Biol. 7, 1232–1239. https://doi.org/10.1038/ncb1324

Ma, M., Cao, X., Dai, J., Pastor-Pareja, J.C., 2017. Basement Membrane Manipulation in Drosophila Wing Discs Affects Dpp Retention but Not Growth Mechanoregulation. Dev. Cell 42, 97–106.e4. https://doi.org/10.1016/j.devcel.2017.06.004

Makowski, D., 2018. The psycho Package: an Efficient and Publishing-Oriented Workflow for Psychological Science. J. Open Source Softw. 3, 470. https://doi.org/10.21105/joss.00470

Mavor, L.M., Miao, H., Zuo, Z., Holly, R.M., Xie, Y., Loerke, D., Blankenship, J.T., 2016. Rab8 directs furrow ingression and membrane addition during epithelial formation in Drosophila melanogaster. Development 143, 892–903. https://doi.org/10.1242/dev.128876

Mellouk, N., Enninga, J., 2016. Cytosolic Access of Intracellular Bacterial Pathogens: The Shigella Paradigm. Front. Cell. Infect. Microbiol. 6, 35. https://doi.org/10.3389/fcimb.2016.00035

Michelson, A.M., Gisselbrecht, S., Buff, E., Skeath, J.B., 1998. Heartbroken is a specific downstream mediator of FGF receptor signalling in Drosophila. Development 125, 4379–89.

Mizuno-Yamasaki, E., Rivera-Molina, F., Novick, P., 2012. GTPase Networks in Membrane Traffic. Annu. Rev. Biochem. 81, 637–659. https://doi.org/10.1146/annurev-biochem-052810-093700

Mohr, S.E., Smith, J.A., Shamu, C.E., Neumüller, R.A., Perrimon, N., 2014. RNAi screening comes of age: improved techniques and complementary approaches. Nat. Rev. Mol. Cell Biol. 15, 591–600. https://doi.org/10.1038/nrm3860

Morrison, H.A., Dionne, H., Rusten, T.E., Brech, A., Fisher, W.W., Pfeiffer, B.D., Celniker, S.E., Stenmark, H., Bilder, D., 2008. Regulation of Early Endosomal Entry by the Drosophila Tumor Suppressors Rabenosyn and Vps45. Mol. Biol. Cell 19, 4167–4176. https://doi.org/10.1091/mbc.e08-07-0716

Neeft, M., Wieffer, M., de Jong, A.S., Negroiu, G., Metz, C.H.G., van Loon, A., Griffith, J., Krijgsveld, J., Wulffraat, N., Koch, H., Heck, A.J.R., Brose, N., Kleijmeer, M., van der Sluijs, P., 2005. Munc13-4 Is an Effector of Rab27a and Controls Secretion of Lysosomes in Hematopoietic Cells. Mol. Biol. Cell 16, 731–741. https://doi.org/10.1091/mbc.e04-10-0923

Neto, H., Balmer, G., Gould, G., 2013. Exocyst proteins in cytokinesis. Commun. Integr. Biol. 6, e27635. https://doi.org/10.4161/cib.27635

Nikolova, L.S., Metzstein, M.M., 2015. Intracellular lumen formation in Drosophila proceeds via a novel subcellular compartment. Development 142, 3964–73. https://doi.org/10.1242/dev.127902

Norris, M., Lecavalier, L., 2010. Evaluating the Use of Exploratory Factor Analysis in Developmental Disability Psychological Research. J. Autism Dev. Disord. 40, 8–20. https://doi.org/10.1007/s10803-009-0816-2

Ohshiro, T., Emori, Y., Saigo, K., 2002. Ligand-dependent activation of breathless FGF receptor gene in Drosophila developing trachea. Mech. Dev. 114, 3–11.

Okenve-Ramos, P., Llimargas, M., 2014. Fascin links Btl/FGFR signalling to the actin cytoskeleton during Drosophila tracheal morphogenesis. Development 141, 929–39. https://doi.org/10.1242/dev.103218

Oshima, K., Takeda, M., Kuranaga, E., Ueda, R., Aigaki, T., Miura, M., Hayashi, S., 2006. IKK epsilon regulates F actin assembly and interacts with Drosophila IAP1 in cellular morphogenesis. Curr. Biol. 16, 1531–7. https://doi.org/10.1016/j.cub.2006.06.032

Pastor-Pareja, J.C., Xu, T., 2011. Shaping Cells and Organs in Drosophila by Opposing Roles of Fat Body-Secreted Collagen IV and Perlecan. Dev. Cell 21, 245–256. https://doi.org/10.1016/j.devcel.2011.06.026

Peränen, J., 2011. Rab8 GTPase as a regulator of cell shape. Cytoskeleton (Hoboken). 68, 527–39. https://doi.org/10.1002/cm.20529

Perrimon, N., Mathey-Prevot, B., 2007. Matter arising: off-targets and genome-scale RNAi screens in Drosophila. Fly (Austin). 1, 1–5.

Pfeffer, S.R., 2017. Rab GTPases: master regulators that establish the secretory and endocytic pathways. Mol. Biol. Cell 28, 712–715.

Pfeffer, S.R., 1994. Rab GTPases: master regulators of membrane trafficking. Curr. Opin. Cell Biol. 6, 522–6.

Preibisch, S., Saalfeld, S., Tomancak, P., 2009. Globally optimal stitching of tiled 3D microscopic image acquisitions. Bioinformatics 25, 1463–1465. https://doi.org/10.1093/bioinformatics/btp184

Prince, E., Kroeger, B., Gligorov, D., Wilson, C., Eaton, S., Karch, F., Brankatschk, M., Maeda, R.K., 2018. Rab-mediated trafficking in the secondary cells of *Drosophila* male accessory glands and its role in fecundity. Traffic. https://doi.org/10.1111/tra.12622

Reichman-Fried, M., Dickson, B., Hafen, E., Shilo, B.Z., 1994. Elucidation of the role of breathless, a Drosophila FGF receptor homolog, in tracheal cell migration. Genes Dev. 8, 428–39.

Revelle, W., 2018. R package “psych”: Procedures for Psychological, Psychometric, and Personality Research.

Ricolo, D., Deligiannaki, M., Casanova, J., Araújo, S.J., 2016. Centrosome Amplification Increases Single-Cell Branching in Post-mitotic Cells. Curr. Biol. 26, 2805–2813. https://doi.org/10.1016/j.cub.2016.08.020

Ríos-Barrera, L.D., Sigurbjörnsdóttir, S., Baer, M., Leptin, M., 2017. Dual function for Tango1 in secretion of bulky cargo and in ER-Golgi morphology. Proc. Natl. Acad. Sci. 114, E10389–E10398. https://doi.org/10.1073/pnas.1711408114

Rojas, R., van Vlijmen, T., Mardones, G.A., Prabhu, Y., Rojas, A.L., Mohammed, S., Heck, A.J.R., Raposo, G., van der Sluijs, P., Bonifacino, J.S., 2008. Regulation of retromer recruitment to endosomes by sequential action of Rab5 and Rab7. J. Cell Biol. 183, 513–526. https://doi.org/10.1083/jcb.200804048

Romero, N.M., Dekanty, A., Wappner, P., 2007. Cellular and developmental adaptations to hypoxia: a Drosophila perspective. Methods Enzymol. 435, 123–144. https://doi.org/10.1016/S0076-6879(07)35007-6

Rosa, J.B., Metzstein, M.M., Ghabrial, A.S., 2018. An Ichor-dependent apical extracellular matrix regulates seamless tube shape and integrity. PLOS Genet. 14, e1007146. https://doi.org/10.1371/journal.pgen.1007146

Roth, M.G., 2004. Phosphoinositides in constitutive membrane traffic. Physiol. Rev. 84, 699–730. https://doi.org/10.1152/physrev.00033.2003

Sánchez-Sánchez, B.J., Urbano, J.M., Comber, K., Dragu, A., Wood, W., Stramer, B., Martín-Bermudo, M.D., 2017. Drosophila Embryonic Hemocytes Produce Laminins to Strengthen Migratory Response. Cell Rep. 21, 1461–1470. https://doi.org/10.1016/j.celrep.2017.10.047

Sandoval, C.O., Simmen, T., 2012. Rab proteins of the endoplasmic reticulum: functions and interactors. Biochem. Soc. Trans. 40, 1426–1432. https://doi.org/10.1042/BST20120158

Sato, T., Mushiake, S., Kato, Y., Sato, K., Sato, M., Takeda, N., Ozono, K., Miki, K., Kubo, Y., Tsuji, A., Harada, R., Harada, A., 2007. The Rab8 GTPase regulates apical protein localization in intestinal cells. Nature 448, 366–369. https://doi.org/10.1038/nature05929

Scheer, N., Campos-Ortega, J.A., 1999. Use of the Gal4-UAS technique for targeted gene expression in the zebrafish. Mech. Dev. 80, 153–158. https://doi.org/10.1016/S0925-4773(98)00209-3

Schindelin, J., Arganda-Carreras, I., Frise, E., Kaynig, V., Longair, M., Pietzsch, T., Preibisch, S., Rueden, C., Saalfeld, S., Schmid, B., Tinevez, J.-Y., White, D.J., Hartenstein, V., Eliceiri, K., Tomancak, P., Cardona, A., 2012. Fiji: an open-source platform for biological-image analysis. Nat. Methods 9, 676–682. https://doi.org/10.1038/nmeth.2019

Schottenfeld-Roames, J., Ghabrial, A.S., 2012. Whacked and Rab35 polarize dynein-motor-complex-dependent seamless tube growth. Nat. Cell Biol. 14, 386–93. https://doi.org/10.1038/ncb2454

Schottenfeld-Roames, J., Rosa, J.B., Ghabrial, A.S., 2014. Seamless tube shape is constrained by endocytosis-dependent regulation of active Moesin. Curr. Biol. 24, 1756–64. https://doi.org/10.1016/j.cub.2014.06.029

Schottenfeld, J., Song, Y., Ghabrial, A.S., 2010. Tube continued: morphogenesis of the Drosophila tracheal system. Curr. Opin. Cell Biol. 22, 633–9. https://doi.org/10.1016/j.ceb.2010.07.016

Seaman, M.N., McCaffery, J.M., Emr, S.D., 1998. A membrane coat complex essential for endosome-to-Golgi retrograde transport in yeast. J. Cell Biol. 142, 665–81.

Sechi, S., Frappaolo, A., Fraschini, R., Capalbo, L., Gottardo, M., Belloni, G., Glover, D.M., Wainman, A., Giansanti, M.G., 2017. Rab1 interacts with GOLPH3 and controls Golgi structure and contractile ring constriction during cytokinesis in *Drosophila melanogaster*. Open Biol. 7, 160257. https://doi.org/10.1098/rsob.160257

Sharma, S., Rao, A., 2009. RNAi screening: tips and techniques. Nat. Immunol. 10, 799–804. https://doi.org/10.1038/ni0809-799

Shaye, D.D., Casanova, J., Llimargas, M., 2008. Modulation of intracellular trafficking regulates cell intercalation in the Drosophila trachea. Nat. Cell Biol. 10, 964–970. https://doi.org/10.1038/ncb1756

Shibata, S., Kawanai, T., Hara, T., Yamamoto, A., Chaya, T., Tokuhara, Y., Tsuji, C., Sakai, M., Tachibana, T., Inagaki, S., 2016. ARHGEF10 directs the localization of Rab8 to Rab6-positive executive vesicles. J. Cell Sci. 129, 3620–3634. https://doi.org/10.1242/jcs.186817

Shibata, S., Teshima, Y., Niimi, K., Inagaki, S., 2017. Involvement of ARHGEF10, GEF for RhoA, in Rab6/Rab8-mediating membrane traffic. Small GTPases 1–9. https://doi.org/10.1080/21541248.2017.1302550

Shiga, Y., Tanaka-Matakatsu, M., Hayashi, S., 1996. A nuclear GFP/beta-galactosidase fusion protein as a marker for morphogenesis in living Drosophila. Dev. Growth Differ. 38, 99–106. https://doi.org/10.1046/j.1440-169X.1996.00012.x

Shirakawa, R., Higashi, T., Tabuchi, A., Yoshioka, A., Nishioka, H., Fukuda, M., Kita, T., Horiuchi, H., 2004. Munc13-4 Is a GTP-Rab27-binding Protein Regulating Dense Core Granule Secretion in Platelets. J. Biol. Chem. 279, 10730–10737. https://doi.org/10.1074/jbc.M309426200

Shishido, E., Higashijima, S., Emori, Y., Saigo, K., 1993. Two FGF-receptor homologues of Drosophila: one is expressed in mesodermal primordium in early embryos. Development 117, 751–61.

Sigoillot, F.D., King, R.W., 2011. Vigilance and Validation: Keys to Success in RNAi Screening. ACS Chem. Biol. 6, 47–60. https://doi.org/10.1021/cb100358f

Sigurbjornsdottir, S., 2015. Complex cell shape: Molecular mechanisms of tracheal terminal cell development in Drosophila melanogaster. University of Iceland.

Sigurbjornsdottir, S., Mathew, R., Leptin, M., 2014. Molecular mechanisms of de novo lumen formation. Nat. Rev. Mol. Cell Biol. 15, 665–676. https://doi.org/10.1038/nrm3871

Sotillos, S., Espinosa-Vazquez, J.M., Foglia, F., Hu, N., Hombria, J.C.-G., 2010. An efficient approach to isolate STAT regulated enhancers uncovers STAT92E fundamental role in Drosophila tracheal development. Dev. Biol. 340, 571–582. https://doi.org/10.1016/j.ydbio.2010.02.015

Steneberg, P., Hemphala, J., Samakovlis, C., 1999. Dpp and Notch specify the fusion cell fate in the dorsal branches of the Drosophila trachea. Mech. Dev. 87, 153–163.

Stenmark, H., 2009. Rab GTPases as coordinators of vesicle traffic. Nat. Rev. Mol. Cell Biol. 10, 513–25. https://doi.org/10.1038/nrm2728

Strickland, L.I., Burgess, D.R., 2004. Pathways for membrane trafficking during cytokinesis. Trends Cell Biol. 14, 115–8.

Sutherland, D., Samakovlis, C., Krasnow, M.A., 1996. branchless encodes a Drosophila FGF homolog that controls tracheal cell migration and the pattern of branching. Cell 87, 1091–101.

Swaminathan, A., Pile, L.A., 2010. Regulation of cell proliferation and wing development by Drosophila SIN3 and String. Mech. Dev. 127, 96–106.

https://doi.org/10.1016/J.MOD.2009.10.003

Toloşi, L., Lengauer, T., 2011. Classification with correlated features: unreliability of feature ranking and solutions. Bioinformatics 27, 1986–1994. https://doi.org/10.1093/bioinformatics/btr300

Tsarouhas, V., Senti, K.-A., Jayaram, S.A., Tiklova, K., Hemphala, J., Adler, J., Samakovlis, C., 2007. Sequential pulses of apical epithelial secretion and endocytosis drive airway maturation in Drosophila. Dev. Cell 13, 214–225. https://doi.org/10.1016/j.devcel.2007.06.008

Ukken, F.P., Aprill, I., JayaNandanan, N., Leptin, M., 2014. Slik and the receptor tyrosine kinase Breathless mediate localized activation of Moesin in terminal tracheal cells. PLoS One 9, e103323. https://doi.org/10.1371/journal.pone.0103323

Vale-Costa, S., Amorim, M., 2016. Recycling Endosomes and Viral Infection. Viruses 8, 64. https://doi.org/10.3390/v8030064

Venables, W.N., Ripley, B.D., 2002. Modern Applied Statistics, 4th ed. ed. Springer, New York.

Vincent, S., Ruberte, E., Grieder, N.C., Chen, C.K., Haerry, T., Schuh, R., Affolter, M., 1997. DPP controls tracheal cell migration along the dorsoventral body axis of the Drosophila embryo. Development 124, 2741–50.

Vincent, S., Wilson, R., Coelho, C., Affolter, M., Leptin, M., 1998. The Drosophila protein Dof is specifically required for FGF signaling. Mol. Cell 2, 515–25.

Vogel, G.F., Janecke, A.R., Krainer, I.M., Gutleben, K., Witting, B., Mitton, S.G., Mansour, S., Ballauff, A., Roland, J.T., Engevik, A.C., Cutz, E., Müller, T., Goldenring, J.R., Huber, L.A., Hess, M.W., 2017. Abnormal Rab11-Rab8-vesicles cluster in enterocytes of patients with microvillus inclusion disease. Traffic 18, 453–464. https://doi.org/10.1111/tra.12486

Wang, C., Yoo, Y., Fan, H., Kim, E., Guan, K.-L., Guan, J.-L., 2010. Regulation of Integrin β1 Recycling to Lipid Rafts by Rab1a to Promote Cell Migration. J. Biol. Chem. 285, 29398–29405. https://doi.org/10.1074/jbc.M110.141440

Wappner, P., Gabay, L., Shilo, B.Z., 1997. Interactions between the EGF receptor and DPP pathways establish distinct cell fates in the tracheal placodes. Development 124, 4707–16.

Wei, T., Simko, V., 2017. R package “corrplot”: Visualization of a Correlation Matrix.

West, R.J.H., Lu, Y., Marie, B., Gao, F.-B., Sweeney, S.T., 2015. Rab8, POSH, and TAK1 regulate synaptic growth in a Drosophila model of frontotemporal dementia. J. Cell Biol. 208, 931–947. https://doi.org/10.1083/jcb.201404066

Wickham, H., 2016. ggplot2: Elegant Graphics for Data Analysis. Springer, New York.

Wilk, R., Weizman, I., Shilo, B.Z., 1996. trachealess encodes a bHLH-PAS protein that is an inducer of tracheal cell fates in Drosophila. Genes Dev. 10, 93–102.

Wixler, V., Wixler, L., Altenfeld, A., Ludwig, S., Goody, R.S., Itzen, A., 2011. Identification and characterisation of novel Mss4-binding Rab GTPases. Biol.

Chem. 392, 239–48. https://doi.org/10.1515/BC.2011.022

Wong, D.M., Shen, Z., Owyang, K.E., Martinez-Agosto, J.A., 2014. Insulin- and warts-dependent regulation of tracheal plasticity modulates systemic larval growth during hypoxia in Drosophila melanogaster. PLoS One 9, e115297. https://doi.org/10.1371/journal.pone.0115297

Wucherpfennig, T., Wilsch-Bräuninger, M., González-Gaitán, M., 2003. Role of Drosophila Rab5 during endosomal trafficking at the synapse and evoked neurotransmitter release. J. Cell Biol. 161, 609–624. https://doi.org/10.1083/jcb.200211087

Yang, X.-Z., Li, X.-X., Zhang, Y.-J., Rodriguez-Rodriguez, L., Xiang, M.-Q., Wang, H.-Y., Zheng, X.F.S., 2016. Rab1 in cell signaling, cancer and other diseases. Oncogene 35, 5699–5704. https://doi.org/10.1038/onc.2016.81

Ye, J., Coulouris, G., Zaretskaya, I., Cutcutache, I., Rozen, S., Madden, T.L., 2012. Primer-BLAST: A tool to design target-specific primers for polymerase chain reaction. BMC Bioinformatics 13, 134. https://doi.org/10.1186/1471-2105-13-134

Yu, J., McMahon, A.P., 2006. Reproducible and inducible knockdown of gene expression in mice. genesis 44, 252–261. https://doi.org/10.1002/dvg.20213

Zerial, M., McBride, H., 2001. Rab proteins as membrane organizers. Nat. Rev. Mol. Cell Biol. 2, 107–17. https://doi.org/10.1038/35052055

Zhang, J., Schulze, K.L., Hiesinger, P.R., Suyama, K., Wang, S., Fish, M., Acar, M., Hoskins, R.A., Bellen, H.J., Scott, M.P., 2007. Thirty-one flavors of Drosophila rab proteins. Genetics 176, 1307–22. https://doi.org/10.1534/genetics.106.066761

8. Appendices

8.1 Cross schemes for YRab-gfpIR lines

YRab on Chr X (10, 18, 21, 27, 35, 39, 40)

gal-1) (f) w-,YRab;+;+   x (m) w-; If/CyO;btl-gal4,UAS-dsRed/TM6,Hu

separate males: $\frac{\mathrm{w-,YRab}}{-};\frac{+}{\mathrm{If/CyO}};\frac{\mathrm{btl}>dsRed}{+}$ (gal-3) and $\frac{\mathrm{w-,YRab}}{-};\frac{+}{\mathrm{If/CyO}};\frac{+}{\mathrm{TM6}}$ (gal-2)

gal-2) (f) w-,YRab;+;+ x (m) $\frac{\mathbf{w-,YRab}}{-};\frac{+}{\mathbf{If/CyO}};\frac{+}{\mathbf{TM6}}$

select virgins: $\mathrm{w-,YRab};+;\frac{+}{\mathrm{TM6}}$

gal-3) (f) $\mathrm{w-,YRab};+;\frac{+}{\mathrm{TM6}}$ x (m) $\frac{\mathbf{w-,YRab}}{-};\frac{+}{\mathbf{If/CyO}};\frac{\mathbf{btl}>dsRed}{+}$

select stock: $\mathrm{w-,YRab};+;\frac{\mathrm{btl-gal4,UAS-dsRed}}{\mathrm{TM6}}$

IR-1a) (f) w-,YRab;+;+ x (m) w-;If/CyO;MKRS/TM6b,Tb,Hu

select males: $\frac{\mathrm{w-,YRab}}{-};\frac{+}{\mathrm{CyO}};\frac{+}{\mathrm{TM6b/MKRS}}$ (IR-2)

IR-1b) (f) w-,YRab;+;+ x (m) yw-;UAS-GFP-IR;+

select males: $\frac{\mathrm{w-,YRab}}{-};\frac{\mathrm{UAS-GFP-IR}}{+};+$ (IR-3)

IR-2) (f) w-,YRab;+;+ x (m) $\frac{\mathbf{w-,YRab}}{-};\frac{+}{\mathbf{CyO}};\frac{+}{\mathbf{TM6b/MKRS}}$

select virgins: $\frac{\mathrm{w-,YRab}}{\mathrm{w-,YRab}};\frac{+}{\mathrm{CyO}};+$ (Cy+ Hu-)

IR-3) (f) $\frac{\mathbf{w-,YRab}}{\mathbf{w-,YRab}};\frac{+}{\mathbf{CyO}};+$ x (m) $\frac{\mathbf{w-,YRab}}{-};\frac{\mathbf{UAS-GFP-IR}}{+};+$

select stock: $\frac{\mathrm{w-,YRab}}{\mathrm{w-,YRab}};\frac{\mathrm{UAS-GFP-IR}}{\mathrm{CyO}};+$

YRab on Chr II (2, 3, 4, 5, 6, 9, 14, 30, 32, X1)

gal-1) (f) YRab;+ x (m) If/CyO; btl-gal4,UAS-dsRed/TM6,Hu

select virgins ($\frac{\mathrm{YRab}}{\mathrm{CyO}};\frac{+}{\mathrm{TM6b}}$) and males ($\frac{\mathrm{YRab}}{\mathrm{CyO}};\frac{\mathrm{btl}>dsRed}{+}$)

gal-2) (f) YRab/CyO;+/TM6   x (m) YRab/CyO;btl-gal4,UAS-dsRed/+

select stock: $\frac{\mathrm{YRab}}{\mathrm{CyO}};\frac{\mathrm{btl-gal4,UAS-dsRed}}{\mathrm{TM6b}}$

IR-1) (f) YRab;+ x (m) UAS-GFP-IR;+

select virgins ($\frac{\mathrm{UAS-GFP-IR}}{\mathrm{YRab}};+$)

IR-2) (f) $\frac{\mathbf{UAS-GFP-IR}}{\mathbf{YRab}};+$ x (m) If/CyO;MKRS/TM6b,Tb,Hu

select larvae: YRab+ if possible, select males

IR-3) Single male crosses

$\frac{\mathbf{UAS-GFP-IR(,YRab)}}{\mathbf{CyO}};\frac{+}{\mathbf{TM6b/MKRS}}$ x (f) If/CyO;MKRS/TM6b,Tb,Hu

genotype lines: $\frac{\text{UAS-GFP-IR,YRab}}{\text{CyO}};+\frac{+}{\text{TM6b/MKRS}}$

IR-4) $\frac{\mathbf{UAS-GFP-IR,YRab}}{\mathbf{CyO}};\frac{+}{\mathbf{TM6b/MKRS}}$ x self: select stock (UAS-GFP-IR,YRab;+)

YRab on Chr III (1, 7, 8, 11, 19, 23, 26, X4, X5, X6)

gal-1) (f) +; YRab x (m) If/CyO; btl-gal4,UAS-dsRed/TM6,Hu

select virgins: $\frac{+}{\text{If/CyO}};\frac{\text{btl}>dsRed}{\text{YRab}}$

gal-2) (f) $\frac{+}{\mathbf{If/CyO}};\frac{\mathbf{btl}>dsRed}{\mathbf{YRab}}$ x (m) If/CyO;MKRS/TM6b,Tb,Hu

select larvae: btl>dsRed+ (YRab+ if possible); select males: $\frac{+}{\text{If/CyO}};\frac{\text{btl}>dsRed(,YRab)}{\text{TM6b/MKRS}}$

gal-3) Single male crosses

$\frac{+}{\mathbf{If/CyO}};\frac{\mathbf{btl}>dsRed(,YRab)}{\mathbf{TM6b/MKRS}}$ x (f) w-;If/CyO;MKRS/TM6b,Tb,Hu

genotype lines: $\frac{+}{\text{If/CyO}};\frac{\text{btl}>dsRed,YRab}{\text{TM6b}}$

gal-4) $\frac{+}{\mathbf{If/CyO}};\frac{\mathbf{btl-ga4,UAS-dsRed,YRab}}{\mathbf{TM6b}}$ x self

select stock (+;YRab,btl>dsRed/TM6b)

IR-Common) (f) If/CyO;MKRS/TM6b,Tb,Hu x (m) UAS-GFP-IR;+

select males: $\frac{\text{UAS-GFP-IR}}{\text{CyO}};\frac{+}{\text{TM6b}}$

IR-1) (f) +;YRab x (m) w-;If/CyO;MKRS/TM6b,Tb,Hu

select virgins: $\frac{+}{\text{CyO}};\frac{\text{YRab}}{\text{TM6b}}$

IR-2) (f) +/CyO; YRab/TM6b x (m) UAS-GFP-IR/CyO;+/TM6b

select larvae: $\frac{\text{UAS-GFP-IR}}{\text{CyO}};\frac{\text{YRab}}{\text{TM6b}}$ and self-cross to eliminate balancers

8.2 Genotyping primers

Rab	Forward (5'->3')	Reverse (5'->3')
Rab1	ACTCTGAACAGCAGCCAGTC	CGTGTGACGACTTACTATTCCG
Rab2	CTGTCGCTAGCCAGTCATCA	CCGTTTCAAAGGAAGTCGCAG
Rab3	TTTCCATTCCCTCCGTGCAG	CACATCTCAACAGCAAGGCAG
Rab4	GGTTTTGATCGTGTCCTGCG	AAATGTGTGCTGACAAACCGT
Rab5	AGGAAGAGCGCATCCACATT	CGATACTTACCGCTCCTGGC
Rab6	ACTCTGGTCACACAGCAACT	GCAGCGGATTGCCAAAATCT
Rab7	GTAAGCCAACGCCACAAACTG	GGAAGTTCATAGTGCTTACCTGC
Rab8	CGGGCCAGATACTGTGATCC	GCGGATGATGACACTCACCT
Rab9	CTCGGGAATCGTGAGTGCAA	TGCAAAAGTTCTACGGCCTTG
Rab10	ATCGAAGTTGCCACACTGGT	GTACGGTCCCGTTACTCACC
Rab11	GGATTTCGTTTAGCACCCGC	CTTCCGCGATCTTCGACCAG
Rab14	CAGCGACTACGGTTGGACAT	GCAGGACGGCAAGTAGAGAT
Rab18	GCAAGGCTGCTGTTACAGTG	TCTCCACGAAGCGACGTATC
Rab19	CAGCAGGCAAAAGAGACCAG	TATTAGTGGCGGGATCTGGG
Rab21	GCTGGTAGACAGCCACACTG	GCTAAACGTACCTTCGCCCA
Rab23	CTCCTCCAACCGATTTGCCT	TGACAGAGATTCACGCAGCC
Rab26	GAACGCCGCAATAGGAGGT	GGGGGATTGTAGGAGCCATC
Rab27	ATCCTTGGAGTGACGAGTGG	CTAGACCGCAGTGCCGTAAT
Rab30	TCGTCTACTTTCGCAGAGCAC	CTGGCCAGGTGGAAATAGACC
Rab32	GGTCGAGTTCAACAAACCGA	AGGTGGAGACAACGCTACTC
Rab35	GTTCGACGCGCCTAACTG	CTGTGGGAAACGGGAATGC
Rab39	GAGCAGCATAAGCAAATCAACG	GCATCTCACGAAGATCGCAC
Rab40	GTTCTACTGGTGGGCGACAG	GGCTTGCATATCCGGTGGTC
RabX1	GAAAGCGATGCGATTGAGCC	GAATGGAGTCCGCCGAATGG
RabX4	CCGAAAACCTCCGCAGTTGA	CTGCACATAACAGCCGAGGTA
RabX5	AAGCCGACCAAGTTTGTGGT	GCCATGCTCACCGATTGACG
RabX6	GCTGTTGTCGCACTGTTGTT	CAGCCATCACGCCCTTTTAG

8.3 Software versions

Software	Version
(FIJI Is Just) ImageJ	2.0.0-rc68/1.52h
Java	1.8..0_66
Quantum-Capt	15.15
RStudio	1.1.456
R	3.5.1
R package corrplot	0.84
R package factoextra	1.0.5
R package GPArotation	2014.11-1
R package MASS	7.3-50
R package psych	1.8.4
ZEN Black	2.3